Università degli Studi di Torino

PhD Programme in Chemical and Materials Sciences XXXII Cycle

MW-assisted synthesis of zirconia-based materials: possible active catalysts in glucose conversion

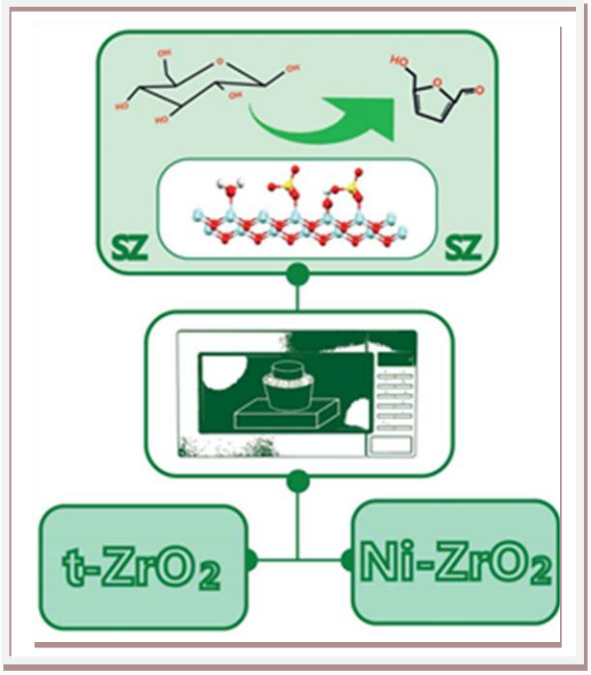

Alessia Giordana

Supervisor:
Prof. Giuseppina Cerrato

Università degli Studi di Torino

PhD Programme in Chemical and Materials Sciences XXXII cycle

MW-assisted synthesis of zirconia-based materials: possible active catalysts in glucose conversion

Candidate: **Alessia Giordana**

Supervisor: Prof. **Giuseppina Cerrato**

Jury Members: Prof. **Marco Daturi**
Université de Caen Normandie – France
Laboratoire Catalise&Spectrochimie

Prof. **Michela Signoretto**
Università "Ca' Foscari" Venezia – Italy
Dipartimento di Scienze Molecolari e Nanosistemi

Prof. **Enzo Laurenti**
Università degli Studi di Torino – Italy
Dipartimento di Chimica

Head of the Doctoral School: Prof. Alberto Rizzuti
PhD Programme Coordinator: Prof. Mario Chiesa

Torino, 2019

Nonostante gli inconvenienti sopra detti, credo che ogni chimico conservi del laboratorio universitario un ricordo dolce e pieno di nostalgia. Non soltanto perché vi si nutriva una camaraderie intensa, legata al lavoro comune, ma anche perché se ne usciva, ogni sera e più acutamente a fine corso, con la sensazione di aver "imparato a fare una cosa"; il che, la vita lo insegna, è diverso dall'aver "imparato una cosa".

Il segno del chimico, Primo Levi

TABLE OF CONTENTS

1. INTRODUCTION

Global concerning about climate changes implication is growing. Not surprisingly, Greta Thumberg was chosen as Time's person of the 2019 year. In recent decades, due to the depleting of fossil fuels reserves and the environmental pollution caused by the impact of CO_2 emission, different international agreements have been rectified. In 2015 the United Nations defined the 17 Sustainable Development Goals, which are still considered the world's best plan to build up a better world for human beings and our planet by 2030.[1] This urgent call for action led to rectification of the Paris Agreement, that highlights the need of a global strategy to reach a sustainable industrial and societal development.[2] So a balance needs to be found among economic development, environmental impact and societal equity. Conventional linear economy encourages short product lifespans, resulting in wastefulness, overconsumption, and product inefficiency. A more environmentaly friendly and stable economic model is proposed to be based on circular grounds. A circular economy approach tries to eliminate waste through deliberate design of products and processes by bearing in mind both resource efficiency and recycling.[3]

Concerning the environmental impact of products design with a cradle-to-cradle perspective, the first consideration is the choice of feedstock. Alternative feedstocks are necessary to reduce dependence on non-renewable sources, and among them biomass represents the only renewable source of organic molecules for the manufacturing of chemicals and fuels, nowadays mainly derived from petrol.[4,5] Most of the process developed in petrochemical industry to functionalize hydrocarbon are not suitable for biomass conversion, which requires controlled de-functionalization of the highly oxygenated raw materials. The development of a bio-based industry passes through the development of efficient

catalysts. Homogeneous catalysts generally show high activity and selectivity, but have some disadvantages in separation and disposal. Heterogeneous catalysts offer in turn advantages in terms of easy separation, reusability and de-corrosion issue, in addition to stability in severe reaction environments.[5] Heterogeneous catalysts thus represent the bes*t option in term of environmental impact and are the preferred option for industrial applications, representing 80-85% among those employed nowadays in industrial processes[6].

1.1 Lignocellulosic biomass valorisation

Biomass is the results of plant photosynthesis, in which simple molecules as CO_2, H_2O, O_2 are transformed into organic (bio)molecules, mainly carbohydrates, using sun light as energy source. Biomass represents an abundant renewable resource of organic molecules, for the subsequent manufacture of chemicals. At first edible biomass was used as feedstock, as maize and oil seeds, for the production of bioethanol and biofuels. The employment of this "first generation" biomass is not considered as a sustainable option in longer term, due to the obvious competition with food production. "Second generation" bio-based fuels and platform chemicals, in contrast, utilise lignocellulosic biomass as feedstock. The ideal scenario, from the viewpoint of a truly circular economy, involves the valorisation of waste biomass generated in the production of edible crops (as sugar cane, corn stover, rice husks).

Lignocellulosic biomass is mainly composed of three polymers, i.e., cellulose, hemicellulose and lignin, as shown in Figure 1.1. Both structure and amount of these plant components vary according to the species, but generally, lignocellulosic biomass consists of 35–50% cellulose, 20–35% hemicellulose, and 10–25% lignin.[7] Lignocellulose has evolved to resist

degradation and its polymers are organized in complex three-dimensional structures. The major component is cellulose, a crystalline glucose polymer organized in planar sheets packed through hydrogen bonding. Hemicellulose, the second most abundant polymer, is a bracket polymer composed of different pentoses (xylose, arabinose) and hexoses (mannose, glucose, galactose) units. Lignin has a more complex structure, being composed of different phenyl-propanoid units that polymerize by random coupling reactions.

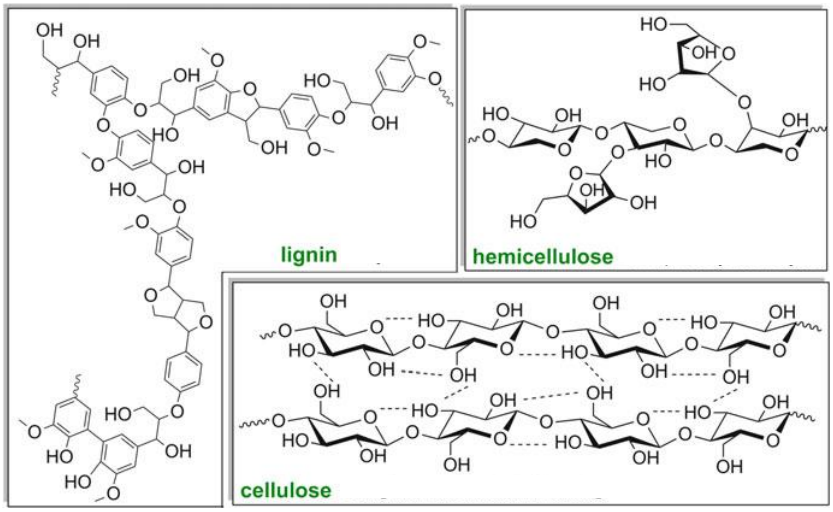

Figure 1.1. Chemical structures of the main components of lignocellulosic biomass.[8]

Different approaches have been proposed in the conversion of lignocellulosic biomass. Biocatalytic processes, that generate bioethanol or biobutanol using fermentation processes, have already reached the commercial stage.[4] Thermochemical processes, as gasification and pyrolysis, have also been applied, similar to those already used in the petrochemicals industry.[9] Gasification yields syn gas, and fast pyrolysis leads to a complex mixture of bio-oils, whose separation is difficult and expensive. Chemical methods allow to better control reactivity and to improve selectivity. First lignocellulosic biomass is fractionated into its main components

(hemicellulose, cellulose, and lignin) and then each fraction is processed in different conditions. Cellulose and hemicellulose can be further hydrolysed in their relevant monomers. Glucose is the sugar degradation product of cellulose. The depolymerization of hemicellulose results in the formation of a mixture of C-5 and C-6 sugars, mainly xylose. Chemical-catalytic methods of biomass valorisation have the potential to utilize almost all of the available carbon present in the feedstock, but they have attracted less commercial attention than fermentative and thermocatalytic methods, possibly due to the fact that they require new technologies. But the potentiality of chemical methods is that higher value chemicals could be produced, besides the production of low-margin/high-volume biofuels. In fact, a variety of organic molecules can be produced in short times and under mild conditions. For example, cellulose might be hydrolysed to glucose, which might be dehydrated to 5-hydroxymethylfurfural (5-HMF), rehydrated to levulinic acid (LA), and then hydrogenated to γ-valerolactone.

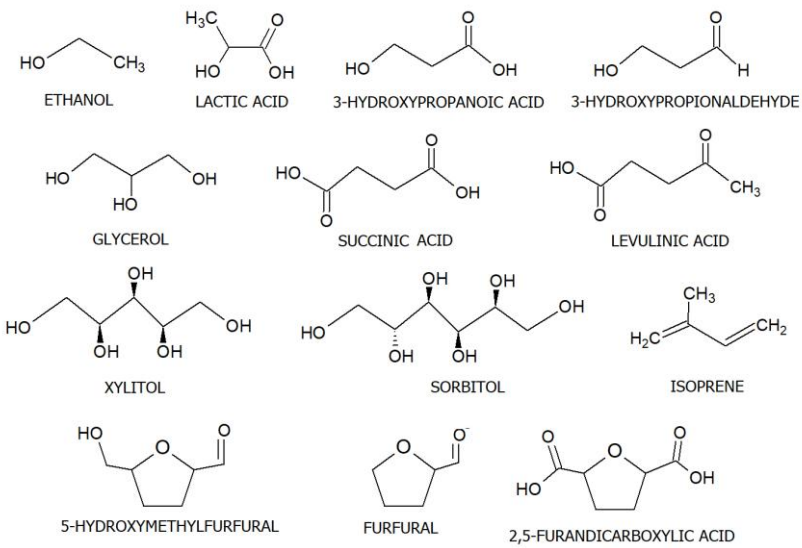

Figure 1.2. Top 13 platform chemicals.

Among 300 potential products derived from carbohydrate biomass to produce chemicals, in 2004 the US Department of Energy[10] sorts a final list of top 12 platform chemicals, mainly based on their market potential. In 2010 Bozell and Petersen re-analyzed this list, using different criteria, as multiple product applicability or technology development, and revisited this list: 13 chemical opportunities were selected, as shown in Figure 1.2.[11] The selected molecules bear at least one functional group in their molecular structure that can serve as entry points for further chemical transformations.

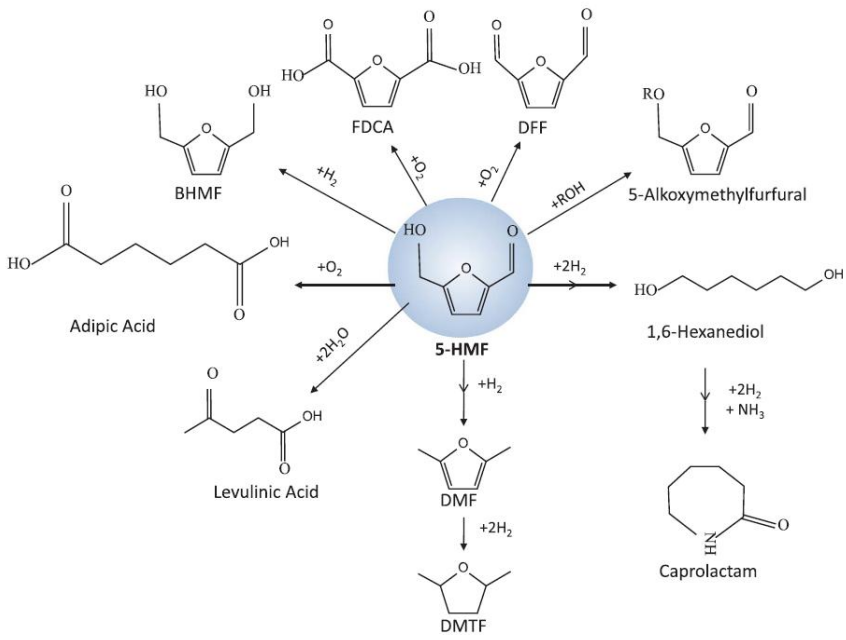

Figure 1.3. Possible value-added chemicals obtainable from 5-HMF.[12]

Among them, 5-hydroxymethylfurfural (5-HMF) is considered a key platform chemical because it can be further converted in a variety of commercially important chemicals, as proposed in Figure 1.3.[12] For example, hydrogenation reactions result in the synthesis of 2,5-dimethylfuran, a commonly used transportation fuel. Also, 5-HMF can be

oxidized to 2,5-furandicarboxylic acid, an important monomer for bioplastic production. Condensation reactions of 5-HMF result in formation of long chain alkanes, that could be used as direct transportation fuel. Hydrolysis of 5-HMF leads to the synthesis of LA and formic acid as well. LA is itself a valuable building block for the production of liquid fuels, gasoline additive, solvents, polymers and other important industrial products. Also formic acid can be used as both a hydrogen donor and a reagent for the synthesis of formaldehyde, plasticizers and pharmaceutical products.[13]

In HMF preparation many studies have used fructose as the starting substrate, that can be easily converted showing high selectivity.[12,14,15] But industrial application are limited by the high costs and restricted availability of fructose. On the other hand, glucose represents an economic and accessible alternative, being the product of cellulose depolymerisation. Synthesis of 5-HMF from glucose is widely recognize to be a two-step process: (i) isomerisation of glucose to fructose catalysed by either a base or Lewis acids, and (ii) hydrolysis promoted by a Brønsted acid catalysts. Starting from glucose as substrate, the low yields have been mainly attributed to self-polymerization reactions between reaction intermediates and/or the 5-HMF itself, forming insoluble humins. Moreover 5-HMF is not stable in water under acid conditions, forming LA and FA for rehydration reaction. Two main strategies have been proposed to improve yield and selectivity: (i) continuous removal of the produced 5-HMF or (ii) design of solid acid catalyst(s) properly tuned for selective formation of 5-HMF.[13] High HMF selectivity seems to result from the Brønsted acid density of the catalyst, whereas the activity in fructose conversion seems to be correlated with the strength of the Lewis acidity, which leads to simultaneous HMF oligomerization.[12] Practical and efficient glucose to 5-HMF conversion thus requires bi-functional solid acid and base catalysts which can operate in aqueous phase, as protonated zeolite, metal oxides and their modified

variations, functionalized silica materials, carbon-based catalysts and phosphate-based catalyst.[5]

Nowadays acid-catalysed reactions represent and important class in hydrocarbon conversions in the petrochemical industry. Reactions catalysed by zeolites and oxides represent ca. 40 and 30%, respectively, of all acid–base catalysed processes.[16] Despite the importance of zeolites as acid catalysts for the current chemical processes, the catalytic processing of biomass involves the transformation of much larger and bulkier substrates that cannot access the zeolite micropores and cavities, and occurs in different conditions, in which zeolite suffer of weak stability. Metal oxides offer the advantages of high thermal stability and to be easily tailored by surface modifications.

We decided to focus our attention over zirconium oxide due to its intrinsic chemical and physical characteristics that can be adjusted by choosing different precursors and synthetic conditions. Moreover, by the addition of dopants/promoters, in particular sulfate species, can modify surface acidity, surface area and crystallization temperature. The acid-basic properties of zirconia make it a catalytic material that can be used in the isomerisation of glucose. Sulfated zirconia (SZ), possessing both Lewis and Brønsted acid sites, can act as catalyst in further dehydration reactions. The reaction pathway and the role of surface sites is not still completely understood. Qi et al[17] studied the production of 5-HMF from fructose and glucose catalysed by ZrO_2 and their results suggest that zirconia acts as base and promotes the isomerisation of glucose to fructose, producing small yield of 5-HMF (ca 10%) and very small amount of LA (<1%). They supposed that the isomerisation reaction involves an acyclic mechanism, and that the rate-determinant step is the enolisation of the starting substrate. Another study[18] employed SZ as catalyst in fructose dehydration

to 5-HMF and reported that it has low catalytic activity in water, while high conversion and 5-HMF yield (ca 80%) are observed in non-aqueous solutions. Both studies employed microwave (MW) heating to promote the reaction. Osatiashtiani et al[19] reported that unsulfated monoclinic zirconia, possessing only Lewis sites, is effective for glucose isomerisation to fructose but poorly active towards fructose dehydration to 5-HMF, while using sulfated tetragonal zirconia, possessing a significant Brønsted acidity, the 5-HMF production is enhanced. Their results suggest that for SZ an appropriate mix of Lewis and Brønsted sites is required for the tandem isomerization of glucose to fructose and the latter subsequent dehydration to 5-HMF, and isomerisation seems to be the rate-determinant step.

1.2 Zirconia and its modification

Zirconia is a well-known material, and it has found application in different fields thanks to its interesting physical and chemicals properties. ZrO_2 has low thermal conductivity, good corrosion resistance, and it is a good refractory material used in thermal barrier coating applications[20]. Zirconium oxide possesses a very high refractive index and it is used as opacifier in ceramic grazes and to manufacture synthetic jewels. As a result of its high oxygen ion conductivity, it is useful as solid electrolytes in oxygen sensors and fuel cells.[21,22] Thanks to its high strength, toughness and hardness it is employed as liner in combustion engines. Zirconia has been used in orthopaedic and dental implants thanks to its high Young's modulus.[23] However, its most important application is in catalysis. ZrO_2 exhibits acid-basic properties and it is also stable at high T, even under reducing atmosphere and photoirradiation. These properties make zirconia a more suitable candidate in catalytic applications if compared to other

ceramic materials as titania, alumina and silica: in fact, it has been employed both as such or as a support.[24,25]

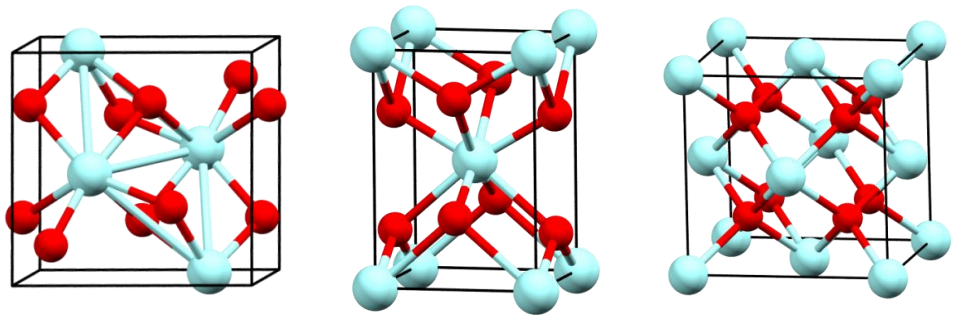

Figure 1.4. Unit cells of crystalline phases of zirconia: from the left monoclinic[26], tetragonal[27] and cubic[28].

ZrO_2 exhibits three crystallographic phases at atmospheric pressure: monoclinic (m-) until 1175°C, tetragonal (t-) from 1175°C to 2370°C, and cubic (c-) above 2370°C, as represented in Figure 1.4. Applications as a ceramic at high temperatures are limited due to the unavoidable martensitic monoclinic-to-tetragonal transformation. However, high temperatures-stable phases (tetragonal and cubic) if properly (chemically and/or physically) stabilised, can be used for low temperature applications. The existence of high T polymorphs at room temperature has been reported in doped bulk and in undoped nanocrystalline materials and various stabilization mechanisms have been proposed by different research groups.[29] In bulk ZrO_2, tetragonal and cubic phases stabilization mechanism is supposed to rely on the generation and association of oxygen ion vacancies with the Zr^{4+} cations hosts. Tetragonal phase can be stabilized at lower T under reduced oxygen partial pressure or at higher temperature at ambient pressure. The most common way to stabilize bulk high temperature polymorphs is by doping with tri-, tetra-, or pentavalent cations, which generate oxygen ions vacancies in the zirconia lattice. First Garvie[30], in 1965, hypothesized that the occurrence of t-ZrO_2 was related to a crystalline size effect, and small

size particles exist as tetragonal phase due to the its lower surface energy compared to the monoclinic phase. The critical size for metastable tetragonal phase stabilization was supposed to be 30 nm. Garvie claimed that stabilization is due to both enhanced specific surface area and excess surface energy below this critical size. He also proposed a thermodynamic model for tetragonal stabilization.[30] Further studies demonstrated the stabilization of tetragonal nanocrystals of smaller size (from 2 to 26 nm) than those proposed by Garvie.[29] HR-TEM analysis suggests that the critical size may be 18 nm.[31] Surface energy theory suggests a critical size of 10 nm, below which isolated, strain free, ZrO_2 nanocrystals are stable, but they must possess a spherical (or near-spherical) surface morphology. Aggregation of zirconia nanocrystallite increases the critical size to 33 nm, similar to value proposed by Garvie. Various other factors seem to affect tetragonal phase stability at room temperature, such as hydrostatic strain energy, structural similarities, foreign surface oxides, water vapour and anionic impurities.

Zirconia can be obtained by the calcination of its hydroxide. The crystal form of the final product depends on how the hydroxide is prepared/obtained and treated. For example, Murase and Kato[24] reported that for hydroxides prepared by direct hydrolysis of a zirconium salt, aging for a long period results in monoclinic formation, while the tetragonal phase is predominant when aging is omitted. The influence of precipitation conditions and aging time on the final crystal form has been interpreted in term of the change of the unit structure of the hydroxide. The synthesis of both tetragonal and cubic ZrO_2 in a nanocrystalline form has been extensively studied in the last decades employing different approaches such as the sol–gel method[32,33], precipitation route[34] and hydrothermal synthesis[35]. In each approach, the crystal form of the final product depends on both synthetic parameters and calcination temperature, still rendering

the synthesis of nanoparticles in pure tetragonal or cubic phase a difficult task.

ZrO_2 is an acid-base bifunctional oxide, capable to absorb both CO_2 and ammonia.[36] Infrared study on adsorbed pyridine revealed the presence of Lewis sites, but not of Brønsted ones.[37] Zirconia has been extensively used as catalyst in the form of either pure oxide or dispersed on other oxides to obtain larger surface area, or even promoted by the addition of properly chosen ions, or finally as a support. In the form of pure oxide, it has found industrial application in different reactions, as alkylation, condensation, isomerization, dehydration.[24] The addition of ions can modify ZrO_2 acid properties: the presence of sulfate groups is known to modify intrinsic Lewis acidic properties of zirconia.[38] Part of the surface is then occupied by thermally stable sulfate groups and there is a lower amount of coordinatively unsaturated surface available cations, but the residual Lewis acidity has been observed to increase in strength; besides, surface sulfates induce Brønsted (protonic) acidity.

Sulfated zirconia was first proposed in 1980 by Hino and Arata[39], and it has found a large employ as solid acid catalyst. SZ has reported to be able to promote short chain hydrocarbons isomerization reaction at relatively low temperature: many studies have been carried out on this catalyst, because of its possible industrial application in alkanes isomerization.[24,38,40] SZ has been tested in many other reactions as such alkylation, acylation, esterification, polymerization and nitration. SZ has demonstrated to be an active catalyst in a heterogeneous liquid–solid system, for reactions as Friedel–Crafts acylations, esterifications of acids with alcohols and reactions between amines and ketones.[41] SZ has shown to be recoverable and reusable, and so offers new opportunities in organic syntheses for developing environmentally friendly processes. The tetragonal phase is

reported to possess higher activity, due to its superior Brønsted surface acidity with respect to the monoclinic one.[42] It is well recognized that activity of SZ catalysts depends on a large number of factors, related in particular to (i) preparation condition, (ii) nature of both zirconium and sulfates precursors, (iii) sulfate loading and (iv) calcination parameters.[43,44,45]

SZ can be produced by means of several syntheses procedures.[46] The catalyst can be prepared by (i) impregnation with H_2SO_4 or $(NH_4)_2SO_4$ on either dried $Zr(OH)_4$ or crystalline zirconia, (ii) direct co-precipitation of sulfate and Zr hydroxide or (iii) by reaction in the gas phase of ZrO_2 with SO_2 or H_2S and O_2. The nature of the starting substrate has a pronounced effect on the final SZ catalyst. Sulfate groups can be bonded onto different surface sites. An high surface area SZ possessing tetragonal phase is obtained by impregnation of amorphous zirconium hydroxide, containing a mixture of defective and non-defective sites.[46,47] The presence of sulfates stabilizes the tetragonal phase avoiding it transform into the thermodynamically more stable m-ZrO_2, and different interpretations have been proposed to explain this behaviour.[47] Impregnation of sulfate precursors onto crystalline zirconia tend to give non-defective surface sulfate structures and only a minimal amount of defective sites.

SZ has shown high activity toward isomerisation of hydrocarbons under mild condition, but unfortunately it suffers of fast deactivation. The addition of small amount of noble metals to the catalyst was proposed to overcome this drawback. In particular, the addition of platinum has been shown to improve both catalytic activity and stability in pentane isomerisation.[24,47] In oxidation catalysis, ZrO_2 is a promising support as well as an active phase.[48] For example it is suggested to be the best support for gold-based catalysts in the oxidative esterification of furfural, promoting activity, selectivity and

also stability.[49] The effect of numerous transition metals was investigated, and all resulted in a modification of the surface acidity.[47,50] Non-noble metals are less expensive and can be active catalysts as well as metal oxides, showing different properties as single, mixed or supported systems.

We decided to investigate the effect of nickel addition into either plain ZrO_2 or SZ. Nickel is the fourth most abundant transitional metals on earth and has a long history in modern catalysis. Its first application as a hydrogenation catalyst dates back to the 19th century and its discovery led Paula Sabatier and Victor Grignard to the Nobel Prize in Chemistry in 1912. Another advantage on the use of Ni is its currently cost (1/5000 of the price of gold).[51] Ni-based catalysts have shown high catalytic activity, or high selectivity in many industrial processes such as steam reforming of hydrocarbons, hydrotreatment, hydrocarbon hydrogenolysis, and CO/CO_2 methanation.[52] But it can also act as cooperative site on other catalysts. In ethylene dimerization it has been reported that Ni is required for a SZ catalyst to be active, and both Ni^+ and Ni^{2+} species have been proposed as potential catalytic sites.[53,54]

The possible methods for the synthesis of metal oxides require long reaction times and/or long thermal treatment at high temperatures to obtain crystalline materials. Coupling these methods with microwave irradiation has the advantages of rapid synthesis and very rapid heating to the required temperature. For example, the formation of SnO_2 by hydrothermal process requires only 3 min instead of hours with conventional heating.[55] It is well known that the catalytic activity and selectivity is dependent on surface structure. Therefore, the different reaction mechanisms between conventional methods and MW-assisted processes may lead to a different structure of the metal oxide obtained and this, may influence their functional properties. In particular, the crystal

structure (phase, crystallinity degree), morphology (size, shape, anisotropy) and composition interplay important role in determining the presence of active catalytic sites in the nanomaterials.

1.3 Microwave heating

Microwaves (MW) are electromagnetic waves in the 0.3–300 GHz frequency range (λ = 1 mm-1 m) occupying in the electromagnetic spectrum the region between infrared and radio frequencies. MW are extensively used in telecommunication systems, and to avoid interferences international agreement requires that industrial reactors and domestic ovens operate at 2.45 GHz.[56] MW heating effect was accidentally discovered in 1945 during studies on radar applications, observing the melting of chocolate bars.[57]. The first paper on MW-assisted synthesis was published in the middle of the 1980s: Komarneni and Roy[58] reported the synthesis of titania gel sphere in liquid phase, while Gedye et al.[59] and Giguere et al.[60] reported the use of MW employed for the organic synthesis. Starting from these reports, MW heating technology has been receiving increasing attention and it has become an important tool, especially in organic syntheses. The major advantages of MW heating reside in the enhanced rate of reactions, which allows to synthesise materials in a few minutes, instead of hours or even days as usually required by the conventional heating methods. It is considered more environmentally friendly than conventional heating being more efficient in selective heating.[61] Several attributes of MW heating contribute to greener syntheses: shorter reaction time, lower energy consumption and higher product yield. MW-assisted methods can help to overcome disadvantages of common techniques in the synthesis of nanoparticles and nanostructures, whose growth is highly sensitive to the reaction conditions and could benefit from the efficient and

controlled heating as provided by MW irradiation.[62] It has been reported that the synthesis of compounds in a metastable phase, with small particles size, small distribution on average particle size, high purity and enhanced physicochemical properties.[59,63]

Many inorganic nanostructured (metals, metal oxides, chalcogenides, nanocomposites) materials have been prepared by MW heating in liquid phase employing various solvents as water, polyols, ionic liquids, and mixed solvents.[57] It has been reported that in liquid phase MW irradiation accelerated not only nucleation, but also crystal growth.[64]

MW energy in not enough to break chemical bonds, so MW chemistry is based on efficient heating of materials, that in turn depends on the ability of materials to absorb and transform electromagnetic energy into heat. MW can penetrate the material and supply energy: heat can be generated throughout the volume of the material resulting in volumetric heating. As a consequence of the direct heating of samples, the temperature profile of a microwave-heated material is the inverse of conventional heating, resulting in the surface being cooler than the inner one. Materials, with respect to their interaction with MW, can be divided into different categories: (i) Reflectors, not effectively heated by MW (metals); (ii) Transmitters, transparent to MW (Teflon and fused quartz); (iii) Absorbers, that take up the energy from the MW field and get heated up very rapidly.[65]

MW dielectric heating is a bulk effect, consequence of a dielectric loss. The heating mechanism is supposed to involve two main processes: dipolar polarization and ionic conduction. MW irradiation of a sample results in the alignment of the dipoles or ions in the electric field. As the applied field oscillates, the dipoles or ions continuously attempt to realign themselves in the electric field and, during the process, energy is lost in the form of heat through rotation, friction and collision of molecules. The ability of a specific substance to convert electromagnetic energy into heat, at a given frequency

and temperature, is determined by the so-called loss tangent (tanδ), expressed as:

$$\tan \delta = \frac{\varepsilon''}{\varepsilon'} \qquad (1)$$

The dielectric constant (ε') describes the ability of the molecules to be polarized by the electric field, and the dielectric loss (ε'') indicates the efficiency with which electromagnetic radiation is converted into heat.[61] A reaction medium with a high loss factor (so high tanδ value) is required for efficient absorption and rapid heating. In Table 1.1 the values of loss tangent of common solvents are reported.

Table 1.1. Loss tangent (tanδ) values at 2.45 GHz and 20°C.[57]

Solvent	**tanδ**	**T_B (°C)**
Ehtylen glycol	1.350	~198
Ethanol	0.941	78
2-propanol	0.799	82
Methanol	0,659	65
1,2-diclhorobenzene	0.280	180.5
Acetic acid	0.174	118-119
Water	0.123	100
Acetone	0.054	56-57
Tetrahydrofuran	0.047	66
Hexane	0.020	68-69

Another important parameter is the penetration depth (d_p), which is defined as the point where 37% of the initially irradiated MW power is still present. The penetration depth is inversely proportional to the loss tangent as shown in eq. 2, where λ_0 represents the wavelength of the microwaves. So, solvents and materials with high loss tangents have short penetration depths.

$$d_p = \frac{3\lambda_0}{8.686\pi \tan \delta (\varepsilon')^{0.5}} \qquad (2)$$

The penetration depth is an important parameter to consider during the design of the synthesis. Vessels of appropriate materials, with specific shape and dimension, have to be chosen to allow MW penetration in the reaction environment.

Table 1.2. Temperature dependence of dielectric properties and penetration depth (d_p) of selected materials.[66] Underlining indicates MW transparency.

Material	**T (°C)**	**ε′**	**ε″**	**d_p (m)**	
		590	10.37	0.027	4.65
Alumina		980	11.06	0.15	0.84
		1340	11.64	0.74	0.18
		25	4.2	<0.05	>1.3
Borosilicate-Glass		500	4.9	0.24	0.29
		880	7.5	3.2	0.028
		25	245	95	0.007
α–SiC		800	433	175	0.0047
		1350	456	360	0.0025
		200	34	0.04	5.68
3%Y_2O_3 – ZrO_2		600	40	6.25	0.039
		1200	50	93	0.004

The loss tangent is not a constant for a giving material, being ε′ and ε″ T dependent. Many solids that do not absorb MW energy at room temperature will begin to absorb when the temperature is increased, as shown in Table 1.2. For example, alumina remains MW transparent until 900°C, but efficiently couples with the MW at higher temperature. Or the low-lossy zirconia becomes an excellent MW absorber above 600°C. It may be noted that dielectric properties also depend on the physicochemical properties of the material, as density, morphology and chemical purity, so the exact T may vary, but the trend remains the same.

The MW heating rate is primarily determined by dielectric and magnetic losses of the materials (ε″ and μ″), but it is affected by several other factor as sample size, geometry/position of the sample, type of MW oven, input power. So the heating rate may vary with the experiment condition.

Walkiewicz et al.[67] performed a series of systematic experiments on different materials with fixed design parameters. Table 1.3 shows the results in term of maximum attainable temperature for each material and the time required to achieve it. Their results are in accordance with the dielectric loss of the material: low-lossy materials are very difficult to heat, while lossy materials reach 1000°C in few minutes. It is also shown that powdered metals can be heated, although bulk metals are reflector. Also in this case the exact temperature and time requested may vary changing experimental design, but the trend remain to be the same.

Table 1.3. The heating rate of various materials (25 g). Data from Ref. 67

Material	T (°C)	Time (min)	Material	T (°C)	Time (min)
Al_2O_3	78	4.5	Graphite Carbon[a]	1073	1.75
ZrO_2	63	4	NiO	1305	6.25
Fe_2O_3	182	7	CuO	1012	6.25
PbO	91	2.25	Al[c]	577	6
MgO	203	5.5	Fe[c]	768	7
Amorphous Carbon[a]	1283	1	Ni[c]	384	1
Graphite Carbon[b]	780	6	Zr[c]	462	6

a=size < 1μm, b~200 mesh, c=powdered samples

When reaction involved MW transparent materials it is possible to use a secondary MW adsorbing material or susceptor, used as dopant or as external susceptor. The former technique is invasive and can alter the chemical composition of the material, so the latter is the most used one. Susceptors are a class of highly lossy materials (as SiC, carbon and CuO), that are rapidly heated by MW, even at room temperature. The heat is transferred to the sample via the conventional model of heat transfer. When the coupling T of the sample is reached, it becomes able to interact with MW. Susceptor assisted MW heating is often referred as 'hybrid heating' because it occurs via a mixed mode: conventional heating in the initial phase and MW heating during the later stage. The efficiency of this

technique is primary dependent on the design of the susceptor, that must provide heating but not shield the material. The most common configuration requires to pack the susceptor around the sample via a two crucibles set-up: the smaller crucible containing the sample is placed is a larger crucible filled with the susceptor powder (see Image 2.1). MW hybrid heating has been applied in material processing (polymers, metals, ores, glass), syntheses and waste treatments.[66]

In literature some studies reporting MW assisted synthesis of zirconia materials can be already found. Zirconia nanoparticles, generally possessing tetragonal phase, can be obtained by MW-hydrothermal treatment using different precursors.[68,69,70] Tetragonal zirconia has been obtained also by sol-gel synthesis in presence of MW irradiation. For example, Fetter et al reported the synthesis of ZrO_2 and Cu/ZrO_2 starting from zirconium butoxide at different pH.[71] Gel formation was induced by MW irradiation, and then the obtained powder calcined at 600°C. They reported that powder always crystallized in the tetragonal phase. Dwivedi et al.[72] applied microware assisted citrate sol–gel method to zirconia synthesis. The gel was dried under MW irradiation and then calcined at 450°C. Also in this case the formation of t-ZrO_2 was observed. More recently, Silva et al[73] reported the preparation of zirconia by a two-step synthetic route, both assisted by MW irradiation. The first step involved gel formation, while in the second step the obtained xerogel was calcined by the MW hybrid method. Their results suggest that MW heating enhanced the formation of tetragonal phase.

1.4 Aim of the work

In this work we investigated the effect of MW heating in the synthesis of zirconia and its modification, to understand if this synthetic procedure

can produce an active catalyst to be further employed in glucose hydrolysis, an important reaction in biomass valorisation.

In the first part the development and optimization of a MW-assisted procedure for zirconia synthesis will be reported and discussed. The proposed method involves two MW-assisted steps: in the first the gel is dried under MW irradiation, while in the second the obtained xerogel is calcinated by a MW hybrid method. MW-assisted methods allow to considerably reduces both time and energy consuming in the synthesis and can affect material properties. Then the optimized method has been applied to the synthesis of Ni-promoted zirconia, sulfated zirconia (SZ) and a preliminary study has been conducted to investigate the effect of addition of both nickel and sulfates species on zirconia. Raman and FTIR spectroscopies, powder X-Ray diffraction (PXRD) and HR-TEM were used to characterized samples.

In the second part the results of the employment of SZ as catalyst in glucose hydrolysis for 5-HMF and LA production will be discussed. The surface properties (as sulfates nature, presence of acid sites) of the employed catalyst have been investigated by means of FT-IR spectroscopy, using CO and 2,6-dymethylpyridine (2,6-DMP) as probe molecules. Mechanism of glucose hydrolysis can follow different routes. Activity and selectivity of employed materials is supposed to be related to the presence, strength and amount of Lewis and Brønsted acid sites. To understand if any correlation between catalytic activity and the presence of surface acid sites exists, it is necessary to quantify the amount of Lewis and Brønsted sites: thus, integrated molar absorption coefficients (ε) of the relevant 2,6-DMP modes related to Lewis and Brønsted are required and have been experimentally determined.

[1] UN General Assembly, *Transforming our world: the 2030 Agenda for Sustainable Development*, 21 October 2015, A/RES/70/1.

[2] United Nations/Framework Convention on Climate Change (2015), *Adoption of the Paris Agreement*, 21st Conference of the Parties, Paris: United Nations.

[3] J.H. Clark, T.J. Farmer, L. Herrero-Davila, J. Sherwood, Circular economy design considerations for research and process development in the chemical sciences, *Green Chem.* **2016** (18), 3914–3934.

[4] R.A. Sheldon, Green and sustainable manufacture of chemicals from biomass: state of the art, *Green Chem.* **2014** (16), 950–963.

[5] S. De, S. Dutta, B. Saha, Critical design of heterogeneous catalysts for biomass valorization: current thrust and emerging prospects, *Catal. Sci. Technol*. **2016** (6), 7364–7385.

[6] G. Ertl, H. Knözinger, F. Schüth, J. Weitkamp, Handbook of Heterogeneous Catalysis, ed. G. Ertl, H. Knözinger, F. Schüth, J. Weitkamp, Wiley-VCH, Weinheim, **2008**, vol. 1.

[7] F.H. Isikgora, C.R. Becer, Lignocellulosic Biomass: A Sustainable Platform for Production of Bio-Based Chemicals and Polymers, *Polym. Chem.* **2015** (6), 4497–4559.

[8] M. Dusselier, M. Mascal, B.F. Sels Top Chemical Opportunities from Carbohydrate Biomass: A Chemist's View of the Biorefinery, in Top Curr Chem, Springer-Verlag, Berlin Heidelberg, **2014**.

[9] Y.C. Lin, G.W. Huber, The critical role of heterogeneous catalysis in lignocellulosic biomass conversion, *Energy Environ. Sci.* **2009** (2), 68–80.

[10] T. Werpy, G. Petersen (2004) Top value added chemicals from biomass. DOE/GO-102004-1992 1.

[11] J.J. Bozell, G.R. Petersen, Technology development for the production of biobased products from biorefinery carbohydrates – the US Department of Energy's "Top 10"revisited, *Green Chem.* **2010** (12), 539–554.

[12] B. Agarwala, K. Kailasamb, R.S. Sangwana, S. Elumalai, Traversing the history of solid catalysts for heterogeneous synthesis of 5-hydroxymethylfurfural from carbohydrate sugars: A review, *Renew. Sust. Energ. Rev.* **2018** (82), 2408–2425.

[13] S. Kanga, J. Fub, G. Zhang, From lignocellulosic biomass to levulinic acid: A review on acid-catalyzed hydrolysis, *Renew. Sust. Energ. Rev.* **2018** (94), 340–362.

[14] B.R. Caes, R.E. Teixeira, K.G. Knapp, R.T. Raines, Biomass to furanics: renewable routes to chemicals and fuels, *ACS Sustain. Chem. Eng.* **2015** (3), 2591–2605.

[15] F. Yang, Q. Liu, X. Bai, Y. Du, Conversion of biomass into 5-hydroxymethylfurfural using solid acid catalyst, *Bioresour. Technol.* **2011** (102), 3424–3429.

[16] K. Tanabe, W.F. Hölderich, Industrial application of solid acid–base catalysts, *Appl. Catal., A* **1999** (181), 399–434.

[17] X. Qi, M. Watanabe, T.M. Aida, R.L. Smith, Catalytical conversion of fructose and glucose into 5-hydroxymethylfurfural in hot compressed water by microwave heating, *Catal. Comm.* **2008** (9), 2244–2249.

[18] X. Qi, M. Watanabe, T.M. Aida, R.L. Smith, Sulfated zirconia as a solid acid catalyst for the dehydration of fructose to 5-hydroxymethylfurfural, *Catal. Commun.* **2009** (10), 1771–1775.

[19] A. Osatiashtiani, A.F. Lee, D.R. Brown, J.A. Melero, G. Moralese, K. Wilson, Bifunctional SO_4/ZrO_2 catalysts for 5-hydroxymethylfufural (5-HMF) production from glucose, *Catal. Sci. Technol.* **2014** (4), 333–342.

[20] D.R. Clarke, C.G. Levi, Materials Design for the Next Generation Thermal Barrier Coatings, *Annu. Rev. Mater. Res.* **2003** (33), 383–417.

[21] V.G. Deshmane, Y.G. Adewuyi, Synthesis of thermally stable, high surface area, nanocrystalline mesoporous tetragonal zirconium dioxide (ZrO_2): Effects of different process parameters, *Micropor. Mesopor. Mat.* **2012** (148), 88–100.

[22] P. Charpentier, P. Fragnaud, D.M. Schleich, E. Gehain, Preparation of thin film SOFCs workin at reduced temperature, *Solid State Ionics* **2000** (135), 373–380.

[23] B. Al-Amleh, K. Lyons, M. Swain, Clinical trials in zirconia: a systematic review, *J. Oral Rehabil.* **2010** (37), 641–652.

[24] T. Yamaguchi, Application of ZrO2 as a catalyst and a catalyst support, *Catal. Today* **1994** (20), 199–218.

[25] K. Tanabe, T. Yamaguchi, Acid-base bifunctional catalysis by ZrO_2 and its mixed oxides, *Catal. Today*, **1994** (20), 185–198.

[26] Monoclinic-ZrO_2: ICSD 37-1484.

[27] Tetragonal-ZrO_2: ICSD 42-1164.

[28] Cubic-ZrO_2: ICSD 27-0997.

[29] S. Shukla, S. Seal, Mechanisms of room temperature metastable tetragonal phase stabilisation in zirconia, *Int. Mater. Rev.* **2005** (50, 1), 45–64.

[30] R.C. Garvie, The Occurrence of Metastable Tetragonal Zirconia as a Crystallite Size Effect, *J. Phys. Chem.* **1965** (69), 1238–1243.

[31] T. Chraska, A.H. King, C.C. Berndt, On the size-dependent phase transformation in nanoparticulate zirconia, *Mater. Sci. Eng.* **2000** (A286), 169–178.

[32] D.Kundu, D. Ganguli, Monolithic zirconia gels from metal-organic solutions, *J. Mater. Sci. Lett.* **1986** (5), 293–295.

[33] D.A. Ward, E.I. Ko, Synthesis and structural transformation of zirconia aerogels, *Chem. Mater*. **1993** (5, 7), 956–969.

[34] A. Benedetti, G. Fagherazzi, F. Pinna, S. Polizzi, Structural properties of ultra-fine zirconia powders obtained by precipitation methods, *J. Mater. Sci.* **1990** (25, 2B), 1473–1478.

[35] S. Somiya, T. Akiba, Hydrothermal Zirconia Powders: A Bibliography, *J. Eur. Ceram. Soc.* **1999** (19), 81–87.

[36] B.Q. Xu, T. Yamaguchi, K. Tanabe, Acid-Base Bifunctional Behavior of ZrO_2 in Dual Adsorption of CO_2 and NH_3, *Chem. Lett.* **1988**, 1663–1666.

[37] Y. Nakano, T. Iizuka, H. Hattori, K. Tanabe, Surface properties of zirconium oxide and its catalytic activity for isomerization of 1-butene, *J. Catal.* **1978** (57), 1–10.

[38] K. Tanabe, Surface and catalytic properties of ZrO_2, *Mater. Chem. Phys.* **1985** (13), 347–364.

[39] M. Hino, K. Arata, Synthesis of Solid Superacid Catalyst with Acid Strength of $H_0 \leq 16.04$, *J.C.S. Chem. Comm.* **1980**, 851–852.

[40] G.D. Yadav, J.J. Nair, Sulfated zirconia and its modified version as promising catalysts for industrial processes, *Micropor. Mesopor. Mat.* **1999** (33), 1–48.

[41] K. Arata, Organic syntheses catalyzed by superacidic metal oxides: sulfated zirconia and related compounds, *Green Chem* **2009** (11), 1719–1728.

[42] C. Morterra, G. Meligrana, G. Cerrato, V. Solinas, E. Rombi, M F. Sini, 2,6-Dimethylpyridine Adsorption on Zirconia and Sulfated Zirconia Systems. An FTIR and Microcalorimetric Study, *Langmuir* **2003** (19), 5344–5356.

[43] D. Fărcaşiu, J.Q. Li, Preparation of sulfated zirconia catalysts with improved control of sulfur content, III. Effect of conditions of catalyst synthesis on physical properties and catalytic activity, *Appl. Catal., A* **1998** (175), 1–9.

[44] D. Fărcaşiu, J.Q. Li, Preparation of sulfated zirconia catalysts with improved control of sulfur content, *Appl. Catal., A* **1995** (128), 97–105.

[45] M. Signoretto, L. Oliva, F. Pinna, G. Strukul, Synthesis of sulfated-zirconia aereogel: effect of the chemical modification of precursor on catalyst porosity, *J. Non-Cryst. Solids* **2001** (290), 145–152.

[46] G.X. Yan, A. Wang, I.E. Wachs, J. Baltrusaitis, Critical review on the active site structure of sulfated zirconia catalysts and prospects in fuel production, *Appl. Catal. A* **2019** (572), 210–225.

[47] X. Song, A. Sayari, Sulfated Zirconia-Based Strong Solid-Acid Catalysts: Recent Progress, Catal. *Rev.- Sci. Eng.* **1996** (38, 3), 329–412.

[48] M.S.L. Aparicio, M.A. Ocsachoque, D. Gazzoli, I.L. Botto, I.D. Lick, Total Oxidation of Naphthalene with Zirconia-Supported Cobalt, Copper and Nickel Catalysts, *Catalysts* **2017** (7), 293–309.

[49] F. Menegazzo, M. Signoretto, F. Pinna, M. Manzoli, V. Aina, G. Cerrato, F. Boccuzzi, Oxidative esterification of renewable furfural on gold-based catalysts: Which is the best support?, *J. Catal.* **2014** (309), 241–247.

[50] N. Liu, X. Wang, L. Shi, X. Meng, Metallic oxide-modified sulfated zirconia: an environment-friendly solid acid catalyst, *New J. Chem.* **2019** (43), 3625–3632.

[51] S. De, J. Zhang, R. Luque, N. Yan, Ni-based bimetallic heterogeneous catalysts for energy and environmental applications, *Energy Environ. Sci.* **2016** (9), 3314–3347.

[52] J. Yang, J. Ren, H. Guo, X. Qin, B. Han, J. Lin, Z. Li, The growth of Nin clusters and their interaction with cubic, monoclinic, and tetragonal ZrO_2 surfaces–a theoretical and experimental study, *RSC Adv*. **2015** (5), 59935–59945.

[53] J.R. Sohn, H.W. Kim, M.Y. Park, E.H. Park, J.T. Kim, S.E. Park, Highly active catalyst of NiO-ZrO_2 modified with H_2SO_4 for ethylene dimerization, *Appl. Catal., A* **1995** (128), 127–141.

[54] A. Finiels, F. Fajula, V. Hulea, Nickel-based solid catalysts for ethylene oligomerization – a review, *Catal. Sci. Technol.* **2014** (4), 2412–2426.

[55] Y. Wang, J. Tian, C. Fei, L. Lv, X. Liu, Z. Zhao, G. Cao, Microwave-assisted synthesis of SnO_2 nanosheets photoanodes for dye-sensitized solar cells, *J. Phys. Chem. C* **2014** (118), 25931–25938.

[56] C.O. Kappe, D. Dallinger, S.S. Murphree, Practical Microwave Synthesis for Organic Chemists: Strategies, Instruments, and Protocols, Wiley-VCH Verlag GmbH, Germany, 2009.

[57] Y.-J. Zhu, F. Chen, Microwave-Assisted Preparation of Inorganic Nanostructures in Liquid Phase, *Chem. Rev.* **2014** (114), 6462−6555.

[58] S. Komarneni, R. Roy, Titania gel spheres by a new sol-gel process, *Mater. Lett.* **1985** (3), 165−167.

[59] R. Gedye, F. Smith, K. Westaway, H. Ali, L. Baldisera, L. Laberge, J. Rousell, The use of microwave ovens for rapid organic synthesis, *Tetrahedron Lett.* **1986** (27), 279−282.

[60] R.J. Giguere, T.L. Bray, S.M. Duncan, G. Majetich, Application of commercial microwave ovens to organic synthesis, *Tetrahedron Lett.* **1986** (27), 4945−4948.

[61] G.A. Tompsett, W.C. Conner, K.S. Yngvesson, Microwave Synthesis of Nanoporous Materials, *ChemPhysChem* **2006** (7), 296–319.

[62] I. Bilecka, M. Niederberger, Microwave chemistry for inorganic nanomaterials synthesis, *Nanoscale* **2010** (2), 1358–1374.

[63] H.J. Kitchen, S.R. Vallance, J.L. Kennedy, N. Tapia-Ruiz, L. Carassiti, A. Harrison, A.G. Whittaker, T.D. Drysdale, S.W. Kingman, D.H. Gregory, Modern Microwave Methods in Solid-State Inorganic Materials Chemistry: From Fundamentals to Manufacturing, *Chem. Rev.* **2014** (114), 1170–1206.

[64] S.H. Jhung, T.H. Jin, Y.K. Hwang, J.S. Chang, Microwave effect in the fast synthesis of microporous materials: which stage between nucleation and crystal growth is accelerated by microwave irradiation?, *Chem.-Eur. J.* **2007** (13), 4410–4417.

[65] K.J. Rao, B. Vaidhyanathan, M. Ganguli, P.A. Ramakrishnan, Synthesis of Inorganic Solids Using Microwaves, *Chem. Mater.* **1999** (11), 882–895.

[66] M. Bhattacharya, T. Basak, A review on the susceptor assisted microwave processing of materials, *Energy* **2016** (97), 306–338.

[67] J.W. Walkiewicz, G. Kazonich, S.L. McGill, Microwave heating characteristics of selected minerals and compounds, *Min. Metall. Process.* **1988** (5), 39–42.

[68] F. Bondioli, A.M. Ferrari, C. Leonelli, C. Siligardi, G.C. Pellacani, Microwave-Hydrothermal Synthesis of Nanocrystalline Zirconia Powders, *J. Am. Ceram. Soc.* **2001** (84, 11), 2728–2730.

[69] F. Bondioli, C. Leonelli, T. Manfredini, A.M. Ferrari, M.C. Caracoche, P.C. Rivas, A.M. Rodrìguez, Microwave-Hydrothermal Synthesis and Hyperfine Characterization of Praseodymium-Doped Nanometric Zirconia Powders, *J. Am. Ceram. Soc.* **2005** (88, 3), 633–638.

[70] J. Liang, Z. Deng, X. Jiang, F. Li, Y. Li, Photoluminescence of Tetragonal ZrO_2 Nanoparticles Synthesized by Microwave Irradiation, *Inorg. Chem.* **2002** (41), 3602–3604.

[71] G. Fetter, P. Bosch, T. Lòpez, ZrO_2 and Cu/ZrO_2 Sol-Gel Synthesis in Presence of Microwave Irradiation, *J. Sol-Gel Sci. Techn.* **2002** (23), 199–203.

[72] R. Dwivedi, A. Maurya, A. Verma, R. Prasad, K.S. Bartwal Microwave assisted sol–gel synthesis of tetragonal zirconia nanoparticles, *J. Alloy. Compd.* **2011** (509), 6848–6851.

[73] E. Silva Jr, S.G. Antonio, E. Longo, Synthesis and structural evolution of partially and fully stabilized ZrO_2 from a versatile method aided by microwave power, *Ceram. In.* **2018** (44), 3517–3522.

2. MATERIALS AND METHODS

2.1 Synthetic procedures

All solvents and reagents employed for the syntheses were commercial products; and as MW heating system an adapted household multimodal MW oven (SAMSUNG C109STF; working at 2,45 GHz) was used.

The general procedure for the preparation of zirconia nanoparticles involved three steps, as represented below:

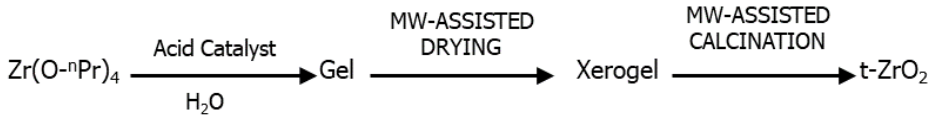

At first, the gel was formed adding water dropwise in a solution containing 5 ml of Zr propoxide (70 wt%, in 1-propanol), 7 ml of solvent and the appropriate amount of the acid hydrolysis catalyst to obtain a final pH~2. The gel obtained was dried into MW oven to rapidly remove the solvent by evaporation. This step is named MW-ASSISTED DRYING and requires 2 cycles of 90 s at 600 W. The obtained xerogel was washed with ethanol and dried. In order to obtain a crystalline product, a further thermal treatment at high temperature was carried out in MW oven using graphite as external susceptor (~10 g per 1.6 g of xerogel, synthetic powder, <20 μm). To promote an homogeneous heating of the sample, graphite completely surrounded the sample crucible (two crucibles set-up), represented in Image 2.1. The thermal treatment is named MW-ASSISTED CALCINATION and requires 2 cycles of 90 s at 600 W. Starting from 5 ml of zirconium precursor about 1.2 g of ZrO_2. was obtained.

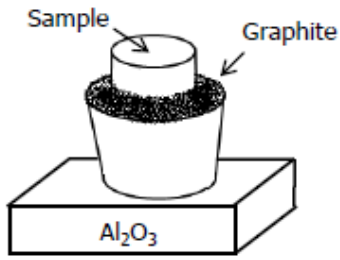

Image 2.1. Schematic representation of susceptor-sample crucibles set-up during MW-assisted calcination.

In Table 2.1 attempted syntheses are summarized. A first set of samples was prepared according to a general procedure using ethanol as solvent and either acetic (Za) or sulfuric (Zb) or nitric (ZE) acids as catalyst to promote hydrolysis. A second set of samples was prepared according to a general procedure using ethanol (ZE) or 2-propanol (ZP) as solvent and different gel aging time (from 0 to 24 hours, indicated as subscript in the relevant sample names). A third set of samples (ZM) was prepared according to a general procedure, but the xerogel was calcinated in a muffle at 400°C or 450°C for 1 hour (dT/dt = 5°C/min). Calcination T is indicated as subscript in the relevant sample names. A fourth set (Z_prec) was prepared by a controlled co-precipitation from aqueous solutions of $ZrOCl_2 \cdot 8H_2O$, and carried out at room temperature and at constant pH (pH = 8.5, using NH_4OH 5.0 M). The precipitate was aged in the mother liquor for 20 h at 90°C, filtrated and washed from chloride ions. MW-assisted calcination was carried out on dry powdery materials.

Sulfates and nickel species were added using, respectively, $(NH_4)_2SO_4$ and $Ni(NO_3)_2 \cdot 6H_2O$ by either wetness impregnation (WI) or by incipient wetness impregnation (IWI) on xerogels prior to calcination or on already formed t-ZrO_2. MW-assisted calcination was carried out on dried impregnated samples (2 cycles of 90 s at 600 W for impregnated xerogel and 2 cycles of 90 s at 450 W for impregnated ZrO_2). Ni addition was also attempted during gel formation using either Ni nitrate, acetylacetonate or

etylendiammine complexes. $Ni(acac)_2$ and $[Ni(en)_3](NO_3)_2$ were prepared according to literature procedures.[1,2] Samples with Ni or sulfate were designated as NixZ_y or SxZ_y where x stands for addition step (0=added during gel formation, 1=impregnated on xerogel, 2=impregnated on t-ZrO_2) and y stands for Ni/S nominal content (as wt%).

Table 2.1. Details of the MW-assisted syntheses.

Sample		Aspect	Acid catalyst	Solvent	Ni/SO_4^{2-} Impregnation
Za		Brown powder	CH_3COOH	EtOH	---
Zb		Brown powder	H_2SO_4	EtOH	---
ZE	ZE_0 ZE_3 ZE_{24}	White powders	HNO_3	EtOH	---
ZP	ZP_0 ZP_3 ZP_{24}	Yellow powder White powder White powder	HNO_3	i-PrOH	---
ZM	ZM_{400} ZM_{450}	White powders	HNO_3	EtOH	---
Z_prec		White powder	---	---	---
S1Z_WI		White powder	HNO_3	EtOH	WI with $(NH_4)_2SO_4$ sol. (0,5 M)
S2Z_WI		White powder	HNO_3	EtOH	WI with $(NH_4)_2SO_4$ sol. (0,5 M)
S1Z	S1Z_5 S1Z_10 S1Z_15	White powders	HNO_3	EtOH	IWI with $(NH_4)_2SO_4$
S2Z	S2Z_5 S2Z_8 S2Z_10 S2Z_15	White powders	HNO_3	EtOH	IWI with $(NH_4)_2SO_4$
Ni1Z	Ni1_2 Ni1Z_10	Dark grey powders	HNO_3	EtOH	IWI with $Ni(NO_3)_2$
Ni2Z	Ni2Z_2 Ni2Z_10	Black powders	HNO_3	EtOH	IWI with $Ni(NO_3)_2$
Ni0Z	Ni0Z_0.5 Ni0Z_2 Ni0Z_5	Pinkish powder Pink powder Brownish powder	HNO_3	EtOH	$Ni(NO_3)_2$ in EtOH
Ni0Z_en		Pinkish powder	HNO_3	EtOH	$[Ni(en)_3](NO_3)_2$ in H_2O (2 wt%)

Table 2.1. Details of the MW-assisted syntheses.

Sample	Aspect	Acid catalyst	Solvent	Ni/SO_4^{2-} Impregnation
Ni0Z_acac	Grey powder	HNO_3	EtOH	$Ni(acac)_2$ in EtOH (2 wt%)
NiS1Z	White powder	HNO_3	EtOH	WI with $(NH_4)_2SO_4$ sol. (0,5 M) containing $Ni(NO_3)_2$ (2 wt%)
NiS2Z	White powder	HNO_3	EtOH	WI with $(NH_4)_2SO_4$ sol. (0,5 M) containing $Ni(NO_3)_2$ (2 wt%)
Ni3S2Z	Grey powder	HNO_3	EtOH	WI with $(NH_4)_2SO_4$ sol. (0,5 M) IWI with $Ni(NO_3)_2$ (2 wt%)
S2Ni0Z	Pink powder	HNO_3	EtOH	$Ni(NO_3)_2$ in EtOH (2 wt%) IWI with $(NH_4)_2SO_4$ (8 wt%)

Our materials were compared to two 'model' systems: sulfated zirconia prepared by a standard precipitation route (SZ_prec) and SBA-SO_3H. SZ_prec was synthesized starting from $ZrOCl_2 \cdot 8H_2O$ according to the precipitation method described above, but the dry powder obtain after washing was impregnated with 8 wt% of sulfates (using $(NH_4)_2SO_4$) and then calcinated in a furnace at 555°C (dT/dt = 10°C/min) for 180 min under air flow (30 ml/min). SBA-SO_3H was kindly supplied by C. Pizzolitto (CATMAT lab. Università Ca' Foscari Venezia, Italy). Details on both preparation method and material characterization can be found in literature.[3]

2.2 Characterization methods

Materials were characterized by means of X-Ray diffraction powder (PXRD) using a X'Pert powder diffractometer operating in a Bragg–Brentano geometry, equipped with a graphite crystal monochromator and using Cu($K_{\alpha 1}$) radiation (λ=1.5406 Å). Crystallite size was calculated using the Scherrer equation ($d = (k \cdot \lambda) \ (\beta \cos\theta)$). Monoclinic volume was calculated using Toraya equation (eq. 1).[4] Fitting procedure of the experimental

spectra was made in the 27°–33° range using Lorentzian curves in order to determine integrated intensity of individual signals.

$$V_m = \frac{1{,}131\ X_m}{1+ 0{,}311\ X_m} \quad ; \quad X_m = \frac{I_m^{28}+ I_m^{31}}{I_t^{30}+ I_m^{28}+ I_m^{31}} \qquad (1)$$

Raman spectra were recorded on pure samples using a Bruker Vertex 70 spectrometer, equipped with the RAMII accessory and Ge detector, by exciting samples with Nd:YAG laser source (1064 nm), with resolution of 4 cm^{-1}. Monoclinic volume was calculated using equation proposed by Tabares et al (eq. 2).[5] Integrated intensity of individual peak were obtained by fitting procedure, using a Lorentzian curve on a linear background in the 125–205 cm^{-1} spectral range.

$$V_m = \frac{I_m^{180}+ I_m^{190}}{(2{,}07\cdot I_t^{147}) + I_m^{180}+ I_m^{190}} \qquad (2)$$

ATR and FIR spectra were obtained on pure samples with a Bruker Vertex 70 spectrophotometer equipped with Harrick MVP2 ATR cell and DTGS detectors (64 scan, 2 cm^{-1} resolution).

FTIR spectra were recorded using a Bruker IFS28 spectrometer, equipped with both MCT and DTGS detectors at 4 cm^{-1} resolution. The solid samples, in form of self-supported pellets (≈10 mg/cm^2), were inserted in a conventional quartz vacuum cell equipped with KBr windows connected to a glass vacuum line (residual pressure<10^{-5} Torr) that allows to perform in situ adsorption/desorption runs. Samples were activated at 300 °C and treated under oxidizing environment. Adsorption/desorption tests of CO and 2,6-dimethylpyridine (2,6-DMP) were carried out at ambient temperature. First, 100 torr of CO was allowed on the sample and then totally evacuated, recording spectra at decreasing pressure. Then a relatively large amount of 2,6-DMP (~ 4 Torr) was allowed on the samples and left in contact for 2 min in order to reach a complete monolayer formation, and then the 2,6-

DMP excess was evacuated for increasing times in the 1-15 min range in order to put into evidence only the more strongly held fraction. Differential spectra were obtained by subtracting the spectra of activated catalysts from the spectra obtained after adsorption/desorption runs.

High resolution transmission electron microscopy (HR-TEM) images of the samples were acquired with a JEOL JEM 3010 UHR operating at 300 kV, equipped with a LaB_6 filament and an Oxford Inca spectrometer for energy-dispersive X-ray spectroscopy (EDS) determinations. All powders were 'dry' dispersed on Cu grids coated with lacey carbon film.

Specific surface areas and pore size distributions were evaluated from N_2 adsorption/desorption isotherms in subcritical conditions (–196 °C), obtained by means of a ASAP 2020 instrument. Surface area was calculated using the B.E.T. model[6] whereas pore size distribution was determined by DFT method[7] (with slit pores and low regularization).

Thermogravimetric analysis (TGA) were performed on a SDT Q600 instrument in air flux (20 mL/min) using a temperature rate set at 10 °C/min in the 25–650 °C temperature range.

ATR spectra were recorded at Laboratoire Catalise&Spectrochimie (ENSI Cean), by with Nicolet Magna spectrometer equipped with MCT detector and Smart iTR sampling accessory (resolution 4 cm^{-1}, 32 scans), properly equipped to allow controlled heating. Consecutive spectra were collected under thermal ramp (5°C/min) from ambient T to 180°C, on glucose and on slurry of glucose solution (1,5 M) and catalyst powder (SBA-SO_3H or S2Z_8).

Integrated molar absorption coefficients determination

Infrared spectra were recorded at Laboratoire Catalise&Spectrochimie (ENSI Cean), with Nicolet Magna 550 FTIR spectrometer equipped with both DTGS and MCT detectors (resolution 4 cm^{-1}, 128 scans). Samples

(SBA-SO_3H and S2Z_8) were pressed into discs (ca. 20 mg; 2 cm^2), activated successively in vacuum and in O_2 at 300 °C (573 K), and cooled down to ambient temperature. The experiments were performed by adding known amounts of 2,6-DMP: increasing pressures were introduced in a known small volume and then expanded in the cell. The probe molecule was allowed to diffuse for 1 min prior to collect the spectrum. Differential spectra were used to calculate the absorbance integrated intensity (noted A) for the considered band (ν_{8a} and ν_{8b} modes of 2,6-DMP). Differential spectra were obtained by subtracting the spectra of activated catalysts from the spectra obtained after 2,6-DMP adsorption.

The integrated molar coefficients (ε) were determined using an equation similar to the Beer-Lambert law:

$$A = \int_{\nu_1}^{\nu_2} A_\nu \cdot d\nu = \varepsilon \cdot b \cdot \frac{n}{S} \cdot b \qquad (1)$$

$$\varepsilon = \frac{A \cdot S}{n} \qquad (\varepsilon \text{ in cm } \mu\text{mol}^{-1}) \qquad (2)$$

where n, S and b denote respectively the amount of 2,6-DMP adsorbed, the surface of the disc and the optical path, assumed as a first approximation to be equivalent to the thickness of the disc. For systems containing several types of bonding between 2,6-DMP and the surface (i.e. 2,6-DMP adsorbed on Lewis or Brønsted acid sites), it must be considered that n is the sum of molecules on different sites:

$$n_{TOT} = n_{Lewis} + n_{Brønsted}; \qquad A_{TOT} = A_L + A_B \qquad (3)$$

$$n_L = \frac{A_L \cdot S}{\varepsilon_L}; \qquad n_B = \frac{A_B \cdot S}{\varepsilon_B} \qquad (4)$$

So, the following equation is obtained:

$$\frac{S}{n}\left(\frac{A_L}{\varepsilon_L}+\frac{A_B}{\varepsilon_B}\right)=1 \qquad (5)$$

For calculating the Lewis and Brønsted integrated molar absorption coefficients eq. 5 was applied and the resulting set of equations was solved by a least-squares procedure. Curve-fitting was used, and best fits were obtained with Voigt curves. The added 2,6-DMP was assumed to be fully adsorbed on the solid. It was assumed that integrated molar absorption coefficient is independent to the degree of coverage and that absorbing molecules do not interact between them. These assumptions are based on previous studies.[8,9,10]

2.3 Catalytic tests

Different sulfated zirconia samples were employed as catalysts in glucose hydrolysis (SZ_WI, SZ_prec, S1Z_5, S2Z_8), in collaboration with CATMAT lab (Università Ca' Foscari Venezia). Reaction was carried out in a batch stainless still autoclave with mechanical stirring and electric heater. Before the reaction, 500 mg substrate, 100 mL of water and appropriate amount of catalyst (from 200 to 500 mg) were added to the reactor and then heated to 180 °C under a 10 bar pressure of N_2. The initial time of the reaction was taken once the reaction temperature was reached. The reaction was carried out for 1-5 hours at 1000 rpm. After this time, the mixture was cooled down to room temperature and separated by filtration. Reaction mixture was analyzed by HPLC (Agilent Technology 1260 Infinity II) equipped by an Aminex HPX-87H column kept at 50°C. The mobile phase was 5 mM H_2SO_4 with a flow rate of 0,6 mL/min. UV-Vis detector (λ=195 nm) was used for the identification of the analytes and their quantitative determination. Reactivity parameters were calculated based on moles of carbon as follow, where i represents a general product of reaction:

$$Glucose\ conversion\ \%\ = \frac{mol\ glu\ in\ -\ mol\ glu\ out}{mol\ glu\ in} \cdot 100\ ;$$

$$C\ balance\ \ \%\ = \frac{C_{out}}{C_{in}} = \frac{(mol\ of\ C\ in\ product)}{mol\ of\ C\ in\ glu\ converted} \cdot 100\ ;$$

$$Yield_{(i)}\ \%\ = \frac{mol_i\ out}{mol\ glu\ in} \cdot 100;$$

$$Selectivity_i\ \%\ = \frac{Yield_i}{Glucose\ conversion} \cdot 100\ .$$

---

[1] R.H. Holm, F.A. Cotton, X-Ray Powder Data And Structures Of Some Bis-(Acetylacetonate)-Metal(II) Compounds And Their Dihydrates, *J. Phys. Chem.* **1961** (65,2), 321–323.

[2] H.M. State, I.K. Reid, F.P. Dwyer, Tris(ethylenediamine)nickel(II) Chloride 2- Hydrate, Tris(Propylenediamine) Nickel(II) Chloride 2- Hydrate, *Inorg. Synth.* **1950** (6), 200–202.

[3] C. Pizzolitto, E. Ghedini, F. Menegazzo, M. Signoretto, A. Giordana, G. Cerrato, G. Cruciani, Effect of grafting solvent in the optimisation of SBA-15 acidity for levulinic acid production, *Catal. Today* **2020** (345) 183–189.

[4] H. Toraya, M. Yoshimura, S. Somiya, Calibration Curve for Quantitative Analysis of the Monoclinic-Tetragonal ZrO_2 System by X-Ray Diffraction, *J. Am. Ceram. Soc.* **1984** (67, 6), C119–C121.

[5] J.A.M. Tabares, M.J. Anglada, Quantitative Analysis of Monoclinic Phase in 3Y-TZP by Raman Spectroscopy, *J. Am. Ceram. Soc*. **2010** (93, 6), 1790–1795.

[6] S. Brunauer, P.H. Emmett, E. Teller, Adsorption of Gases in Multimolecular Layers, *J. Am. Chem. Soc.* **1938** (60), 309−319.

[7] J.P. Oliver, W.B. Conklin, Determination of Pore Size Distribution from Density Function Theoretical Models of Adsorption and Condensation within Porous Solids, presented at First Internatonal Symposium on Effects of Surface Heterogeneity in Adsorption and Calatysis on Solids, Kazimierz Dolny, Poland, **1992**.

[8] C.A. Emeis, Detrmination of integrated Molar extinction coefficients for infrared absorption bands of pyridine adsorbed on solid acid catalysts, *J. Catal*. **1993** (141), 347−354.

[9] S. Khabtou, T. Chevreau, J.C. Lavalley, Quantitative infrared study of the distinct acidic hydroxyl groups contained in modified Y zeolites, *Micropor. Mater*. **1994** (3), 133−148.

[10] T. Onfroy, G. Clet, M. Houalla, Quantitative IR characterization of the acidity of various oxide catalysts, *Micropor. Mesopor. Mat.* **2005** (82), 99–104.

3. MICROWAVE-ASSISTED SOL-GEL SYNTHESIS

3.1 MW-assisted synthesis of zirconia

The proposed synthetic procedure for the synthesis of zirconia can be divided in three steps, as shown in Scheme 3.1. First, the gel was formed starting from an alcoholic solution of zirconium propoxide, using an acid catalyst to promote hydrolysis. Then the polar solvent was eliminated from the gel by evaporation promoted by few minutes of MW irradiation (MW-assisted drying). Finally, the obtained xerogel was calcinated in the same MW oven using graphite as external susceptor (MW-assisted calcination). A white crystalline powder, that is demonstrated to be tetragonal zirconia (t-ZrO_2), (vide infra) was obtained in three steps of few minutes.

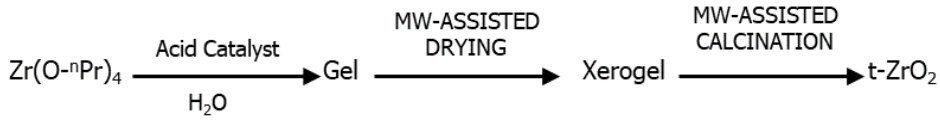

Scheme 3.1. Synthetic procedure.

Many parameters are known to influence sol-gel synthesis, as gel-time, starting precursor, employed catalyst, drying condition, aging time, etc.[1,2,3,4] We always used the same starting precursor and drying condition, and we investigated effects of different solvents (2-propanol or ethanol) at different aging time and we tested different acid catalysts (acetic, nitric and sulfuric acid). Many parameters could influence MW treatment: volume of the sample, dimension and shape of the vessel, power used during procedure.[5,6,7,8] Many trials were attempted to test and optimized the procedure in drying and calcination steps. To ensure reproducibility the same vessels (positioned in the focusing position of oven) and the same volume of samples were used for each specific treatment in MW oven. The employed

multimodal MW oven can operate at different power levels: 180 W, 300 W, 450 W, 600 W and 900 W. It works in continuous mode at the higher power level and in pulsed mode at lower levels, with on-off cycle of irradiation (20 s on-10 s off). In MW-assisted drying, we started from lower power levels, but it was noted that is it necessary to work at least at 450 W to observe quantitative solvent evaporation from the gel. On the contrary, work at 900 W seems to cause superheating and hot spot formation[7], so it was avoided. Analogously, in MW-assisted calcination it was noted that the minimum power level to rapidly heat graphite was 450 W, and the continuous mode was not used to avoid superheating and ensure reproducibility of the process. In addition, studies suggest that pulsed mode leads to smaller particles.[9]

In the first step, to remove solvent, few minutes are requested at 600 W. After this treatment the majority of the solvent was evaporated from the samples and the obtained xerogel interacts no more with MW: even using maximum power and long exposure time no changes are observed in the material. Raman spectrum of the liquid collected from evaporation, reported in Figure 3.1, exhibits signals attributable to 1-propanol, from zirconium precursor, and ethanol, used as solvent. It is possible to observe the ν_{10} modes at 861 cm^{-1} (of 1-propanol) and at 885 cm^{-1} (of solvent)[10]. Powder products obtained after MW-assisted drying is still amorphous as evidenced by the diffractogram shown in the inset of Figure 3.1: it is supposed to be formed by zirconium oxy-hydroxide, as suggest by the broad peak at 450 cm^{-1} and signals below 1000 cm^{-1} present in Raman spectra and ascribable to Zr–O modes[11,19]. The intense band at 1050 cm^{-1} can be attributable either to the symmetric vibration of the nitrate ions, or to a vibration of the Zr–OH group.[4]

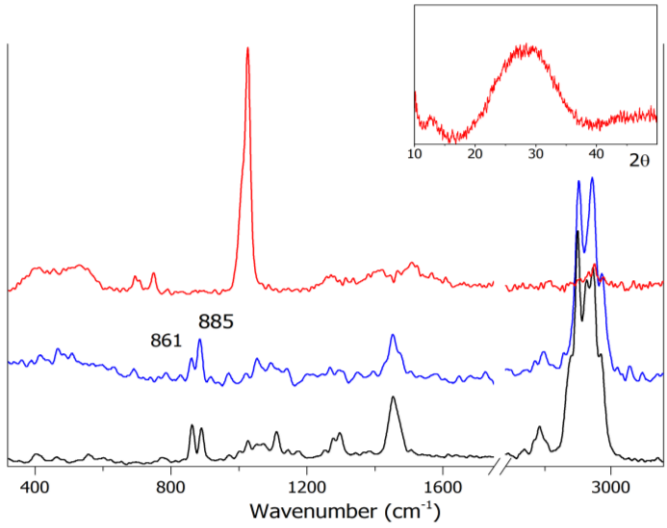

Figure 3.1. Raman spectrum of zirconium precursor (in black), of washed xerogel (in red) and of the liquid removed from the gel (in blue). In the inset diffractogram of the xerogel.

Since xerogels show no heating when exposed to MW, in the subsequent step we decide to use a susceptor[12], which is defined as a substance that has the ability to absorb electromagnetic energy and convert it into heat, allowing to quickly reach high temperature. A crystalline powder was obtained after few minutes of treatment at 600 W. It is not simple to define a specific calcination temperature. It is in general not easy to define the correct temperature of MW treatment, being the recorded T depended upon both the measurement method and the position of the measuring device within the system. Measurement can be carried out with shielded thermocouple, fiber optic or infrared temperature sensors.[13] It was shown that there is often a difference in the T recognition by possible sensors.[14] In the case of the thermocouple the measure is punctual and can be done inside the reaction mixture, whereas IR sensor usually reads temperature in the outside of the vessel and fiber optic sensor can be inserted directly in the reaction solution. The thermal effect induced by MW irradiation is caused by inverse heat transfer and so T profile is opposite to

conventional heating, being the inside hotter than the surface. Trying to define an appropriate profile temperature in our synthetic procedure, T was measured during the MW-assisted calcination using an optic pyrometer and after the treatment using a thermocouple, into graphite and into sample crucible. To avoid graphite contamination, the sample is placed in a separated crucible (see Image 2.1) and heat is transferred by direct contact between hot graphite and vessel walls. Alumina was chosen as material for crucible being MW transparent, a good thermal conductor, resistant at high temperature and chemically inert.[12,15] During the MW treatment in pulsed mode it is possible to observe graphite powder becoming incandescent (red colour) after few seconds in cycle on, and return black when irradiation stops (cycle off). Temperature variation is fast and the maximum and minimum detected T, during cycle on, were 750°C and 380°C. These values are comparable to literature.[12] The temperature seems to be slightly higher in the centre of the system, where the sample is located. It has been reported that zirconia is a MW absorber at high T[12], so we can suppose that the sample, heated by graphite, starts to absorb MW radiation. The temperature of the susceptor after MW-assisted calcination resulted of 450°C, becoming 250°C after 5 minutes and 40°C after half an hour. Inside the sample crucible, after MW-assisted calcination, the recorded temperatures were the same. This suggests that during cycle off (of 10 s) the temperature does not get down below 400°C. We can conclude that the temperature of calcination is cyclic (as represented in Figure 3.2), reaching a maximum of 750°C at the end of cycle on and a minimum 400°C during cycle off.

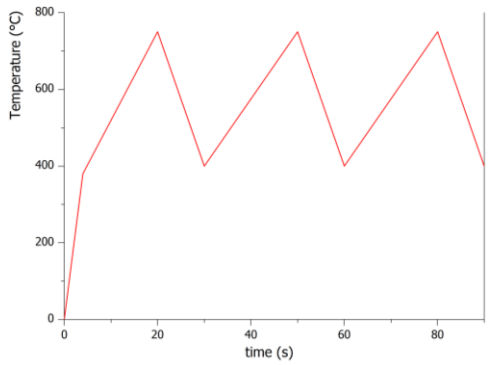

Figure 3.2. Temperature profile during MW-assisted calcination, by optic pyrometer.

We decided to explore the effect of different acid catalyst to promote hydrolysis of zirconium alkoxide: nitric, acetic and sulfuric acid. Using acetic and sulfuric acid the hydrolysis is slow, taking at least 15 minutes, and gels are dense, like a cream. Changing stoichiometry and aging time has no effect on the final density of gels. Gels were dried in MW oven until evaporation is no longer observed. In Figure 3.3 ATR spectra of xerogels are reported. It is possible to recognize signals ascribable to acetate species: CH_3 stretching, scissoring and rocking modes are evident at 2932, 1455, 1344, 1050 and 1020 cm^{-1}, and the COO symmetric and asymmetric stretching modes are present at 1407 and 1544 cm^{-1}.[16] Spectrum of xerogel from sulfuric acid presents a broad band in the 1250-900 cm^{-1} region, ascribable to the combination of ν_3 and ν_1 modes of sulfate species.[16] Powders obtained after calcination of these xerogels are amorphous, as evident from the diffractograms shown in Figure 3.4b: moreover, Raman spectra of the obtained brown powders are dominated by a broad fluorescence band (not show). Many attempts of MW-assisted calcinations were done increasing time and power levels, but almost the same results were obtained. ATR spectra of final products (reported in Figure 3.3)

compared to those of xerogels are very similar, confirming that calcination was ineffective.

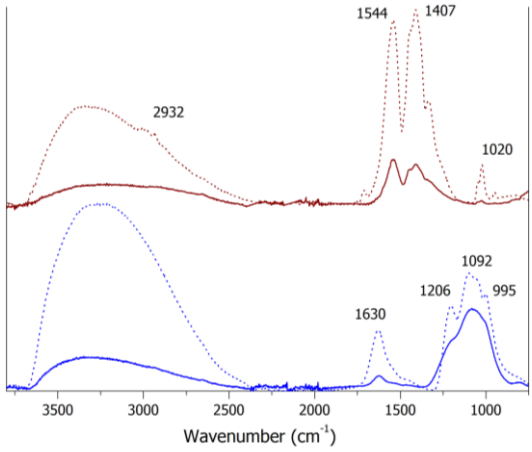

Figure 3.3. ATR spectra of xerogel (dot line) and calcinated powder (solid line) obtained using acetic acid (in red) and sulfuric acid (in blue).

At the contrary, using nitric acid the hydrolysis reaction is fast (less than 2 minutes), and the obtained gel is compact, like jelly. After the MW-assisted drying the powder was calcinated in MW oven and a white powder of tetragonal zirconia[17] was obtained, as confirmed by PXRD pattern shown in Figure 3.4a. It can be noticed that, during MW-assisted calcination, sample produces a red dense smoke, probably related to the formation of NO_2 in the degradation of nitrate ions, reported to occur around 300°C[18]. Raman spectra, reported in Figure 3.4c, allow to investigate the transformation that is taking place during the synthesis. In the gel it is possible to recognize signals of the Zr precursor, of ethanol solvent (at 885 cm^{-1})[10], of nitrate ions (around 1050 cm^{-1}) and of the Zr–O bonds present in gel network (below 650 cm^{-1})[19]. Signals attributable to nitrate and Zr–O bonds are still present in the xerogel spectrum, and the absence of organic residues is confirmed by the vanishing of CH vibration mode at ~2900 cm^{-1}. Calcinated product exhibits the pattern of tetragonal ZrO_2 with characteristic signals at 149, 271, 317, 461, 602 and 646 cm^{-1}.[11,20] Among the tested

catalysts, nitric acid is resulted to be the only appropriate one, forming quickly a gel and giving a crystalline tetragonal product. From here on, HNO_3 has been employed as acid catalyst in the reported syntheses.

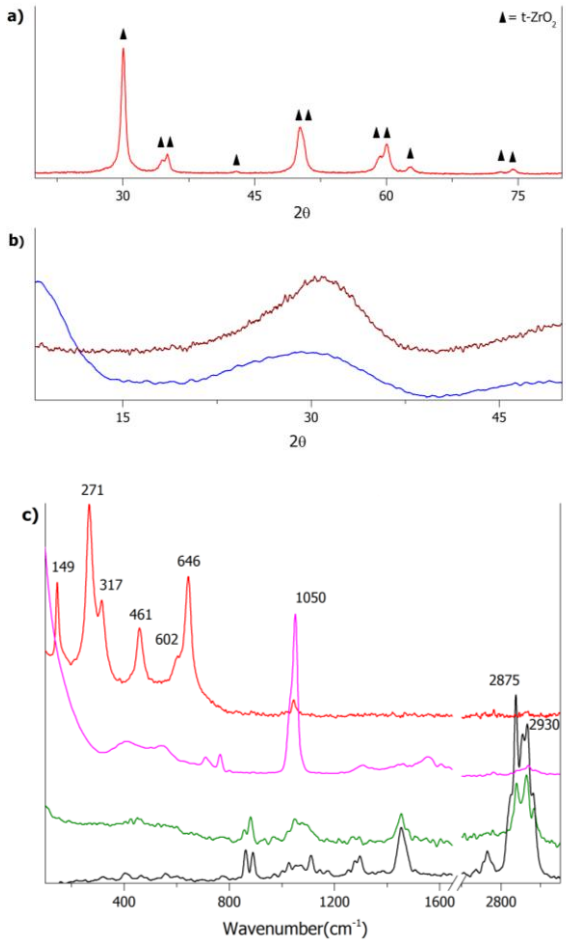

Figure 3.4. Diffractograms of calcined products using: (a) HNO_3 (in red); (b) CH_3COOH (in brown) and H_2SO_4 (in blue), (triangles indicate tetragonal signals)[17]; (c) Raman spectra of zirconium precursor in black, gel in green, xerogel in pink and final product in red (all from HNO_3).

Moreover, we decided to study the variation of two synthetic parameters: solvent (ethanol and 2-propanol) and gel aging time. As already stated, using nitric acid gelification is fast, and the formed gel is kept at ambient temperature untill to 24 hours. Pure t-ZrO_2 has been

obtained from both solvents, but with different aging time. Using ethanol as solvent, Raman spectra in Figure 3.5a, evidence the formation of tetragonal zirconia[11,20]. Extending aging time till 24 hours, a growth of monoclinic fraction was observed, with characteristic peaks at 176, 186, 380 and 475 cm^{-1}.[11,20] PXRD characterization confirms the formation of tetragonal zirconia[17] and also the presence of monoclinic[21] fraction in samples with longer aging time, as evidenced in Figure 3.5b. In samples prepared using 2-propanol as solvent we observe an opposite trend. Raman and PXRD characterizations (presented in Figure 3.5) evidence that without aging time the product obtained after calcination is largely amorphous and it becomes more and more crystalline when gel aging time is extended, showing typical patterns of tetragonal phase[11,17,20] after aging of 24 hours.

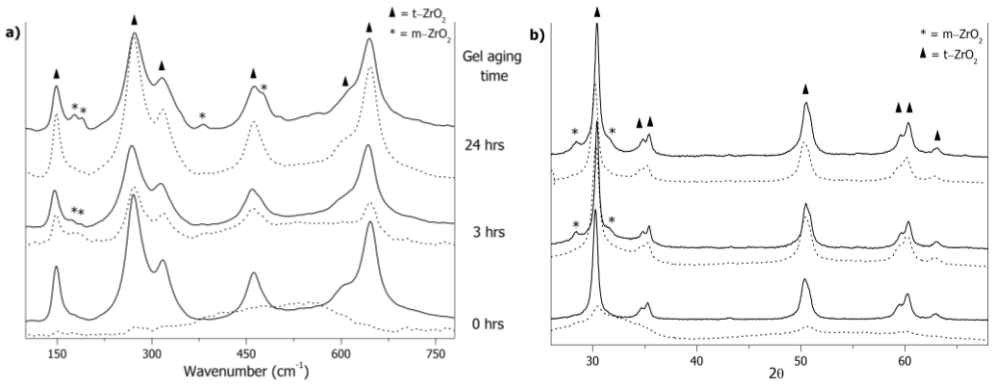

Figure 3.5. Raman spectra (a) and diffractograms (b) of calcinated products obtained using ethanol (solid line) or 2-propanol (dot line) as solvent at increasing aging time.

Further characterizations have been carried out on pure tetragonal samples: ethanol with no aging time (ZE_0) and propanol aged 24 hours (ZP_{24}). Both samples exhibit IV type adsorption isotherm curves, as shown in Figure 3.6, with the characteristic hysteresis loop of a mesoporous material, presenting a H4 loop shape. Samples exhibit very similar SSA values (respectively 60 and 70 m^2/g) and pore size distribution. The curve,

in the inset to Figure 3.6,evidences a bimodal distribution of pores size: both micro and mesopores are present.

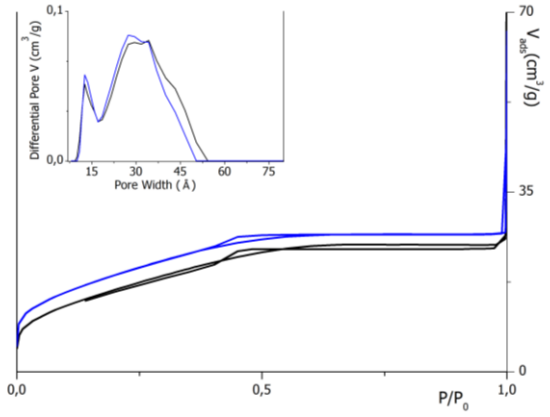

Figure 3.6. Adsorption/desorption isotherms of ZE_0 (black) and ZP_{24} (blue), in the inset curves of pores distributions.

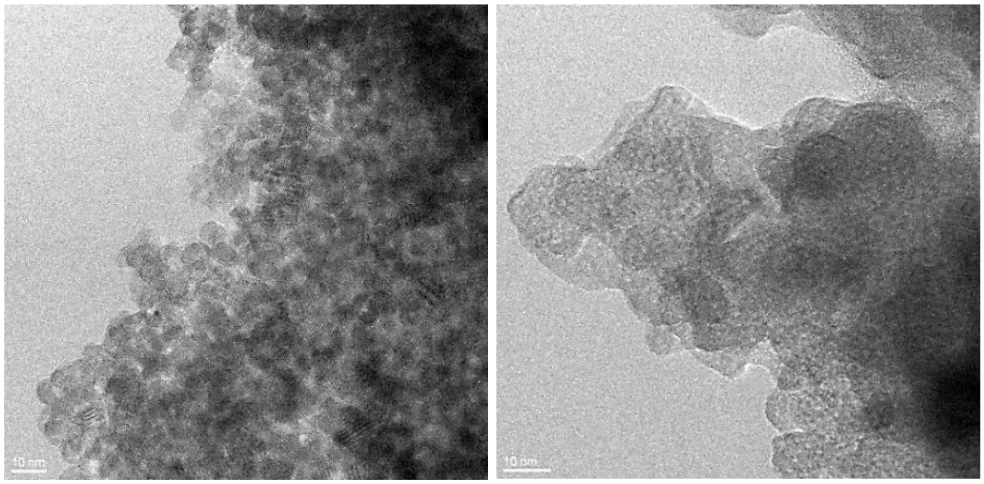

Figure 3.7. HR-TEM images of ZE_0 (on the left) and ZP_{24} (on the right) at the same magnification.

HR-TEM images of both samples show small crystallites, with dimension around 10 nm. We can observe that for ZE_0 all the particles look smaller and have roundish contours with closed packed features, while for ZP_{24} particles seems to be more closed packed and look less individual compared to the former one, as evident in Figure 3.7. ZE_0 particles exhibit a

highly ordered habit, as it is quite simple to single out fringe patterns confirming the high crystallinity of the materials. The detailed inspections of the distances of the fringe patterns, and the parallel analysis of the diffraction patterns, indicate that the most frequently observed fringe patterns belong to (101) family planes of t-ZrO_2[22] with d_{hkl}= 0.299 nm and (112) family planes of t-ZrO_2[22] with d_{hkl}= 0.183 nm (in Figure 3.8). EDS analyses (in Figure S1) were carried out for both samples in many different portions of the grids and confirmed the purity of nanoparticles.

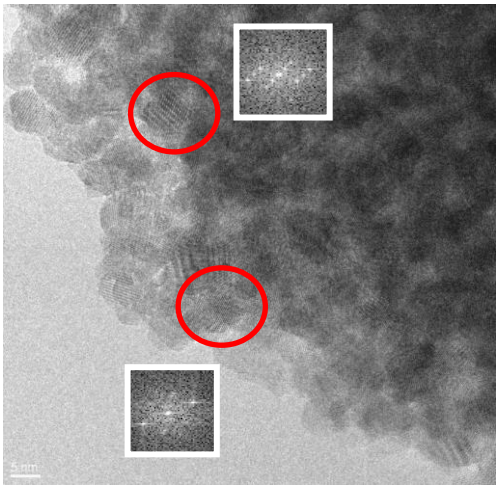

Figure 3.8. HR-TEM image and electronic diffraction patterns of ZE_0 particles.

These results allow us to discriminate between the role played by the two solvents involved in the preparation. Samples are in both cases belonging to crystalline tetragonal zirconia, with nanoparticles exhibit similar surface area, pore sizes and distribution. HR-TEM images show that particles are very small, but ZE_0 nanoparticles are more crystalline and appears to be more homogeneous. This effect could be related to MW irradiation. The drying process of gel is faster and more effective for ZE_0: in fact, differently to ethanol,2-propanol signals are still present and intense in Raman spectra of xerogels (see Figure S2). Ethanol has higher dielectric

loss tangent than 2-propanol[7]: the interaction with MW seems to promote a more rapid and homogenous evaporation of this solvent from gel, that may influence dimension and aggregation of the final particles.

To understand which step is more influenced by MW irradiation, we decided to prepare samples subjected to only one MW treatment:

- Set A: xerogel (obtained from MW-assisted drying) calcinated in muffle;
- Set B: MW-assisted calcination of Zr intermediate (by precipitation from $ZrOCl_2$).

For set A, xerogel obtained by MW-assisted drying is calcined in a muffle at 400°C or 450°C for 1 hour. These temperatures were chosen because they lay in the range of recorded T. As discussed before, during the cycle of irradiation off we supposed that temperature does not go down beyond 400°C, reaching cyclical 750°C. Calcination in muffle has been conducted in static atmosphere, similar to MW-assisted treatment, to better compare the two methods. In both samples we observe the presence of both tetragonal and monoclinic phases. At 400°C the minor intensity of signals in vibrational and structural characterizations indicates that the sample has poor crystallinity, but still both phases are detectable, as shown in Figure 3.9. At higher T it is possible to notice an increase of the tetragonal fraction. For set B, zirconium oxy-hydroxide intermediate was chosen being similar in composition to xerogel, and MW-assisted calcination leads to formation of a pure tetragonal product (see Figure 3.9). These results suggest that the last step is the most influenced by MW irradiation: the rapid heating provided by susceptor during MW-assisted calcination seems to favour nucleation, grown and stabilization of the tetragonal phase.

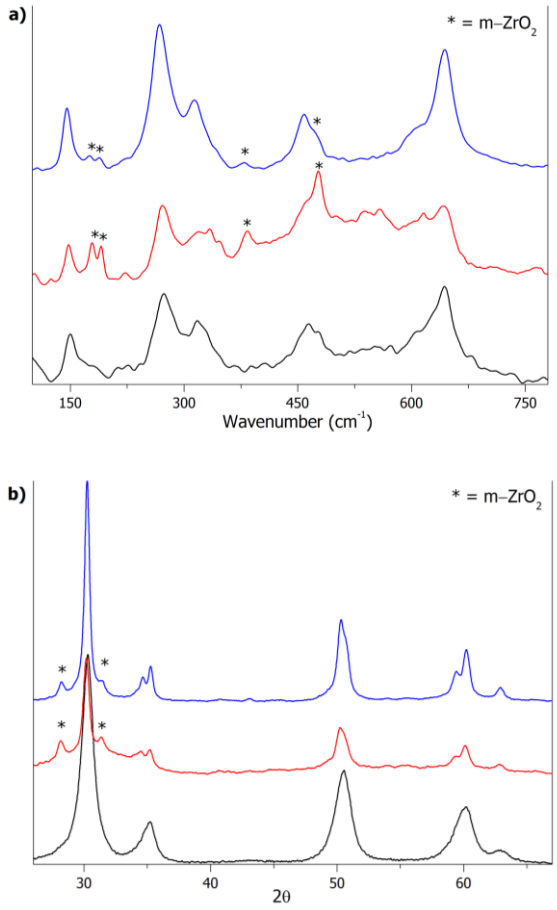

Figure 3.9. Raman spectra (a) and diffractograms (b) of sample obtained from precipitation method (in black), and samples calcinated in muffle at 400°C (in red) and 450°C (in blue).

The quantitative analysis of polymorphic zirconia systems has been object of interest due to the study on the martensitic monoclinic-tetragonal transformation and the effect on the material toughening, for example in its application as implants. Quantification can be done using both XRD and Raman data. In fact, diffractograms of the monoclinic phase possesses characteristic signals at 28.2° and 31.51°, whereas the tetragonal phase most intense signal lies at 30.2°. Also in Raman spectra there are characteristic peaks: the monoclinic doublet at 180-190 cm^{-1} and the

tetragonal peak at 147 cm^{-1}. In 1984, Toraya et al proposed equation (1) to determine monoclinic volume from X-ray data.[23]

$$V_m = \frac{1{,}131\ X_m}{1+ 0{,}311\ X_m} \quad ; \quad X_m = \frac{I_m^{28} + I_m^{31}}{I_t^{30} + I_m^{28} + I_m^{31}} \qquad (1)$$

Several equations are given in the literature for determining the composition of monoclinic and tetragonal mixtures from Raman spectra. Tabares et al[24] analysed t- and m-ZrO_2 mixtures with known composition from PXRD and Raman spectroscopy, and used literature equations for determining the relevant composition. Comparison of results indicated that Toraya's equation provided the actual composition of the mixtures with an excellent accuracy. Using Raman data, researchers estimated k for the linear equation (2), which value (2,07) is similar to that reported in other two papers[25,26], while logarithmic and power law equations seems to be inaccurate for predicting the composition.

$$V_m = \frac{I_m^{180} + I_m^{190}}{(k \cdot I_t^{147}) + I_m^{180} + I_m^{190}} \qquad (2)$$

In Table 3.1 the volume of monoclinic fraction (V_m) calculated with Toraya's[23] and Tabares's[24] equations has been reported. There is a good accordance between volumes calculated using PXRD and Raman data, but values resulted in general higher in the latter case. This could be related to the fact that monoclinic fraction is very low and in this case Raman spectroscopy is more sensitive, being Raman scattering of m-ZrO_2 more intense than the tetragonal one. The calculated crystallite dimension (D) resulted a little overestimated as compared to the mean value of 10 nm suggested by HR-TEM images for ZE_0 and ZP_{24}. Sherrer's equation determines crystallites dimension and is not the most appropriate way to determine nanoparticles size but allow us to quickly compare samples. We

can notice a general dimension increase when the samples are not pure tetragonal. The smallest particles have been obtained in Z_prec, suggesting again that MW-assisted calcination promotes the formation of small tetragonal nanoparticles.

Table 3.1. Comparison of crystalline data of ZrO_2.

Sample	Cryst. Phase	V_m [a]	V_m [b]	D(Å)
ZE_0	t-	--	--	10.6
ZE_3	t- + m-	0.17	0.18	18.6
ZE_{24}	t-+ m-	0.34	0.37	14.7
ZP_0	am.+ t-	--	--	45.2
ZP_3	t- + am.	--	--	36.5
ZP_{24}	t-	--	--	11.1
ZM_{400}	t-+ m- + am.	0.35	0.38	12.1
ZM_{450}	t-+ m-	0.11	0.14	17.2
Z_prec	t-	--	--	7.43

[a]=from PXRD data, [b]=from Raman data

The rapid heating seems to favour the crystallization into metastable tetragonal phase. Thermal analysis, in Figure 3.10, indicates that after dehydration, completed at around 400°C, the material is stable untill 580°C. At this temperature the signal derivative heat flow curve could suggest a modification of crystalline phase in the material.

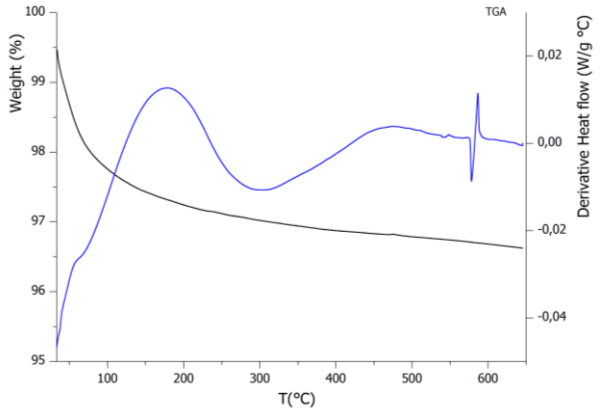

Figure 3.10. TGA of ZE_0: black line indicates loss weight and blue line indicates derivative heat flow.

The proposed MW-assisted synthesis leads to the formation of tetragonal zirconia. Various parameters have been investigated and the procedure was optimized. Homogenous roundish crystalline nanoparticles of t-ZrO_2 were obtained using ethanol as solvent; MW-assisted sol-gel synthesis involves three steps, each one less than 5 minutes long. Compared to a classic sol-gel route the main advantages are (i) the time and (ii) energy saving in calcination step that is completed is 3 minutes instead of hours needed for the traditional method. To the best of our knowledge no similar method been reported for calcination on metal oxides. Furthermore, the rapid heating seems to promote a rapid crystallization in tetragonal phase, the most valuable for catalytic applications.

3.2 MW-assisted synthesis of Ni-promoted ZrO_2

Dopants addition can enhance tetragonal stability and also affect surface properties. We investigated the effect of Nickel addition during the different synthetic step. During zirconia synthesis, nitrate species have been shown to easily degrade during MW-assisted calcination, so we chose $Ni(NO_3)_2$ as nickel precursor. It was added in different synthetic steps: (i) dissolved in ethanol (named Ni0Z), (ii) impregnated on xerogel (Ni1Z) or (iii) on already formed zirconia (Ni2Z). A first set of samples was prepared adding 2 wt% in Ni. Macroscopically speaking, calcined samples are very different, passing from a pink powder for Ni0Z_2, to darker powder for Ni1Z_2 (grey) and Ni2Z_2 (black). On the contrary samples diffractograms exhibit very similar features, as evident in Figure 3.11a. Both cubic[27] and tetragonal phase[17] are present and singled out, even though their patterns are very similar, exhibiting signals with analogous relative intensities in similar position. Results suggest that Ni0Z_2 and Ni2Z_2 are made up of tetragonal zirconia, showing double peaks around 35° and 60° and a weak

signal at 43.1°. The position and the shape of analogous peaks in the diffractogram of Ni1Z_2 indicate the formation of the cubic phase. Adding Ni on xerogel, i.e. in the still amorphous intermediate, leads to the stabilization of the cubic phase, the same of Ni oxide.

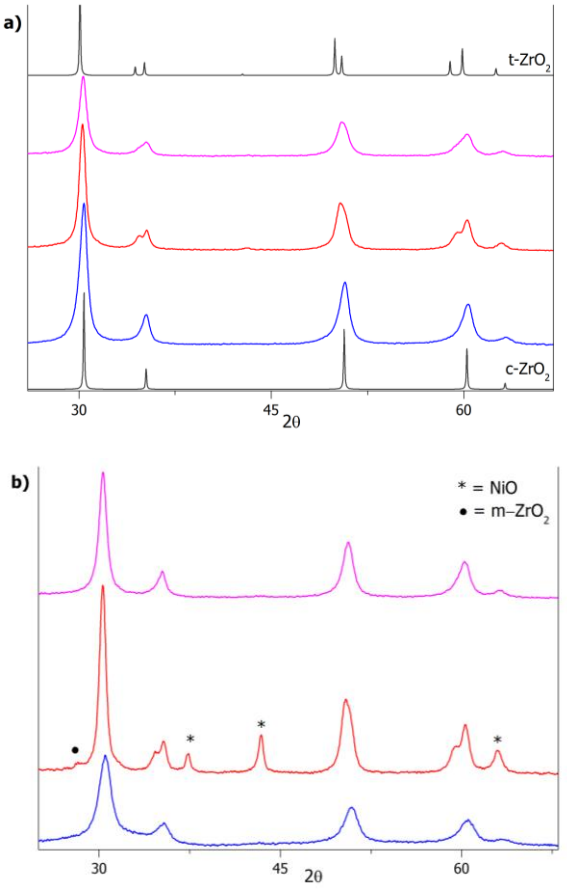

Figure 3.11. (a) Diffractograms of Ni1Z_2 (in blue), Ni2Z_2 (in red) and Ni0Z_2 (in pink) and calculated patterns of cubic[27] and tetragonal[17] ZrO_2; (b)Diffractograms of Ni-rich samples: Ni1Z_10 (in blue), Ni2Z_10 (in red) and Ni0Z_5 (in pink).

To confirm this assumption, samples with an higher concentration of Ni were then prepared: Ni0Z_5, Ni1Z_10 and Ni2Z_10. The lower concentration in the sample Ni0Z, is due to the limits of solubility of nitrate salt in the alcoholic solution. As shown in Figure 3.11b, Ni-rich samples confirms the trend: impregnation on xerogel leads to the cubic phase[27],

whereas in the diffractogram of Ni2Z_10 and Ni0Z_5 it is possible to recognize the presence of crystalline t-ZrO_2[17]. Inspection of Ni2Z_10 pattern indicates also the formation of crystalline NiO (2θ=37.3°, 43.4°, 63.0°)[28] and of a small fraction of m-ZrO_2[21].

Raman spectroscopy is a useful tool to discriminate between the crystalline phase of zirconia, each phase exhibiting a characteristic pattern. As shown in Figure 3.12a, spectra of Ni0Z_2 and Ni2Z_2 present the typical pattern ascribable to the tetragonal phase[11,20], whereas Ni1Z_2 exhibits only a weak broad band at around 620 cm^{-1}, characteristic of cubic phase[20,29]. We can observe a general broadening of Ni0Z_2 signals, suggesting the formation of a solid solution[30]. Raman spectra of Ni-rich samples are dominated a broad fluorescence band (employing a near-IR laser, at 1064 nm), so Far-InfraRed (FIR) spectra were also recorded. According to literature[29] t-ZrO_2 is expected to give rise to 3 active IR bands in this spatial region: one near 160 cm^{-1}, dominated by the movement of Zr ions (E_u mode), and two in the 400-650 cm^{-1} range, associated with the movement of oxide ions. Cubic phase is expected to have only one IR active mode which generates a broad band with a maximum near 500 cm^{-1}. Spectra of ZE and Ni0Z_5 (in Figure 3.12b) present a band at 160 cm^{-1} and a broad signal with a maximum around 460 cm^{-1}, which could be ascribed to t-ZrO_2. The poor resolution of the spectra is related to the small dimension of the particles, which influence peaks width, and to the fact that two bands at higher wavenumbers underwent to TO-LO splitting, in fact similar spectra are reported for zirconia nanoparticles[29]. FIR spectrum of Ni1Z_10 shows a broad band in the 100-650 cm^{-1} range, that confirms cubic phase, as suggested by diffraction data. In this case the broadening of the band could be related to the presence of Ni dopant. FIR spectrum of Ni2Z_10 presents a broad band with a maximum at 405 cm^{-1}, probably due to the sum of NiO (reported a strong band at 465 cm^{-1})[31] and t-ZrO_2 signals.

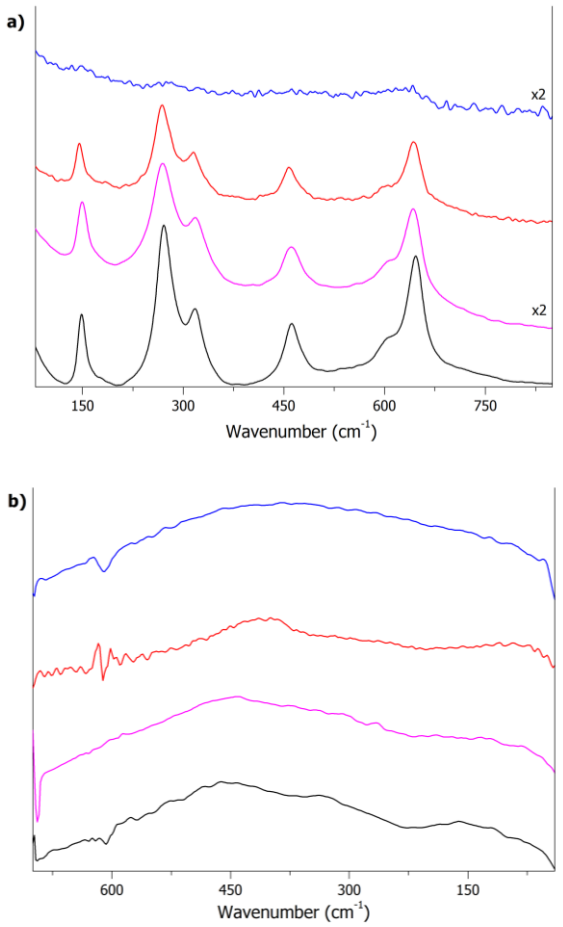

Figure 3.12. (a) Raman spectra of ZE (in black), Ni0Z_2 (in pink), Ni1Z_2 (in blue) and Ni2Z_2 (in red); (b) FIR spectra of ZE (in black), Ni0Z_5 (in pink), Ni1Z_10 (in blue) and Ni2Z_10 (in red).

In the literature it is possible to find other examples of Ni-promoted zirconia. In 1995 Valigi at al[32] investigated the incorporation of Ni^{2+} into the zirconia structure. Samples were prepared by impregnation of hydrous zirconium oxide with an Ni nitrate solution. Authors suggest the formation of a solid solution where nickel ions are incorporated into the zirconia structure in a substitutional site, favouring the tetragonal modification at the expense of the monoclinic one (found in Ni free sample). In 1996 Alvarez at al[33] prepared a series of Ni-promoted sulfated zirconia catalysts,

depositing sulfate and Ni nitrate over a zirconium hydroxide precursor prior to calcination. Authors reported to have obtained pink powders of tetragonal zirconia, as confirmed by diffraction data. More recently a series of metallic oxide-modified sulfated zirconia were prepared by a solvent-free route heating the mixture of metal oxide, $ZrOCl_2 \cdot 8H_2O$ and $(NH_4)_2SO_4$. Also in this case it is suggested that the incorporation of metallic oxides enhanced/favoured the formation of tetragonal ZrO_2. In our samples, differently to those reported previously, the formation of the cubic phase is favoured when the Ni precursor was impregnated on xerogels, but in the same studies, the undoped samples are reported to be monoclinic, and not tetragonal as in our case. We can observe that NiO crystallizes in a fluorite-type structure[34] and that Ni^{2+} ion has a dimension very similar to Zr^{4+} (respectively 69 and 72 pm)[35]. Impregnation on the still amorphous intermediate seems to lead to incorporation of nickel ions in the zirconia lattice, forming a solid solution that stabilizes the cubic phase, as indicated by both vibrational and diffraction data. After impregnation of Ni on already formed t-ZrO_2 nanoparticles, NiO is formed on top of the particles surface as expected from the thermal degradation of nickel nitrate[36]. When Ni was dispersed in solvent prior to gel formation, we obtained tetragonal zirconia, but since the same phase was obtained for undoped system, in our case tetragonal stabilization cannot be due to Ni alone. To understand the influence of Ni content in tetragonal phase stabilization, samples with different amount of Ni (from 0.5 to 5 wt%) were also prepared. As shown in Figure 3., Raman spectra and diffractograms present the typical pattern of tetragonal phase[11,20, 17], but also Raman signal broadening with the increase of Ni content. These could be related to an increase of disorder in the zirconia lattice and support the hypothesis of the formation of a solid solution[30].

The effect of Ni source was also investigated, using as alternative either acetylacetonate or etylendiammine complex during gel formation. In the case of $Ni(acac)_2$, the complex was dissolved in the alcoholic solution, obtaining an homogenous green solution that forms a not uniform gel. Xerogel obtained after MW-assisted drying are green but presents ATR spectrum analogous to ZE samples. Thermal decomposition of $Ni(acac)_2$ is reported to start around 200°C, producing CO_2, methane, acetone and other gases (that include mesityl oxide, methyl acetate, butane, propylene, propane), which amounts increase with increasing T.[37] A similar behaviour is observed during MW-assisted calcination: a white smoke starts to be evolved from the sample and its production increases during heating. A grey powder is obtained, and its diffraction pattern, shown in Figure 3.13b, indicates to be tetragonal zirconia[17]. Its Raman spectrum is covered by fluorescence and it is not reported. We can suppose that the grey colour of Ni_acac can be ascribed to the deposition of carbonaceous species, generated by the ligand degradation and responsible of Raman fluorescence, at the surface. In the case of $[Ni(en)_3](NO_3)_2$, because of the insolubility of the complex in ethanol, it was necessary to dissolve it in water, and the solution was then added to promote gelification. Also in this case the obtained gel is not homogenous and during MW-assisted calcination it is possible to observe the formation of white smoke. Thermal degradation studies[18] indicate that $[Ni(en)_3](NO_3)_2$ decomposes at 220°C in a single step to give nickel oxide as a residue. The gaseous products include N_2, NO and N_2O species from nitrate degradation and ammonia, hydrogen and nitrogen from the fragmentation of ethylenediamine. Vibrational and structural data, reported in Figure 3.13, indicate that the pink powder is made up of tetragonal zirconia.[11,17,20]

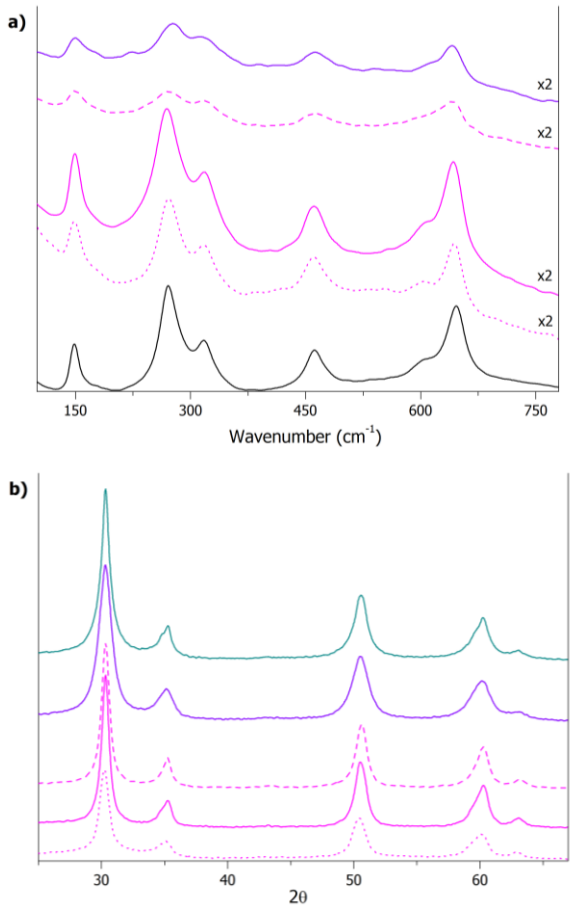

Figure 3.13. Raman spectra (a) and diffractograms(b) of ZE (black line), Ni0Z_0.5 (pink dot line), Ni0Z_2 (pink solid line), Ni0Z_5 (pink dash line), Ni0Z_en (violet line) and Ni0Z_acac (blue line).

To understand the nature of Ni on samples surface, CO was used as probe molecule.[38,39,40] Prior to adsorption all samples were activated in the same conditions. Samples were heated at 300 °C for 1 hour, first in vacuum, then in oxidizing atmosphere for 20 minutes and eventually in vacuum. Spectra of activated sample in OH stretching region, presented in Figure 3.14, show the presence of terminal and bridged groups on ZrO_2, with signals respectively at 3765 cm^{-1} and 3675 cm^{-1}.[41] For Ni0Z_en, signals around 2900 cm^{-1} suggests that a organic fraction is still present in the sample.

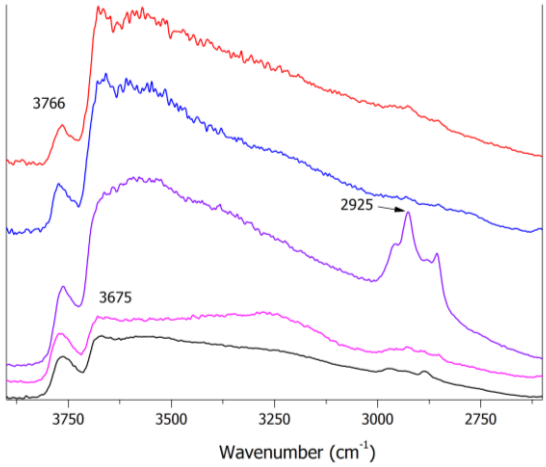

Figure 3.14. FTIR spectra of activated samples in OH spectral region: ZrO_2 (in black), Ni0Z_2 (in pink), Ni0Z_en (in purple), Ni1Z_10 (in blue) and Ni2Z_10 (in red).

CO adsorption on ZE at room temperature gives a characteristic band related to formation of Zr^{4+}–CO complex at 2181 cm^{-1}, which is shifted to higher frequencies with decreasing pressure and vanished after evacuation (in Figure 3.15a), similar to literature reports.[42,43,44] For Ni0Z_2, as shown in Figure 3.15c, in addition to the strong signal at 2181 cm^{-1}, a series of peaks is evident at lower wavenumbers. The higher intensity of the signal at 2181 cm^{-1} with respect to pure ZrO_2 could be ascribable to the contribution of the stretching mode of CO coordinated to Ni^{2+}, which is reported to be located in this range.[38,39,40] Below 2100 cm^{-1} signals can be ascribed to carbonyl species of metallic Ni.[38] In the spectral region between 2160 and 2100 cm^{-1} signals were supposed to be ascribable to Ni^{+} species, an oxidation state that has been observed on others Ni catalysts.[38,39,40] These results suggest that Ni0Z_2 contains Ni species of different nature on the surface. If we inspect differential spectra relative to Ni0Z_en, reported in Figure 3.15b, it is possible to observe a strong signal at 2179 cm^{-1} and a weak peak around 2038 cm^{-1}. The intensity of peak at 2180 cm^{-1} is lower it compared to pure ZrO_2,

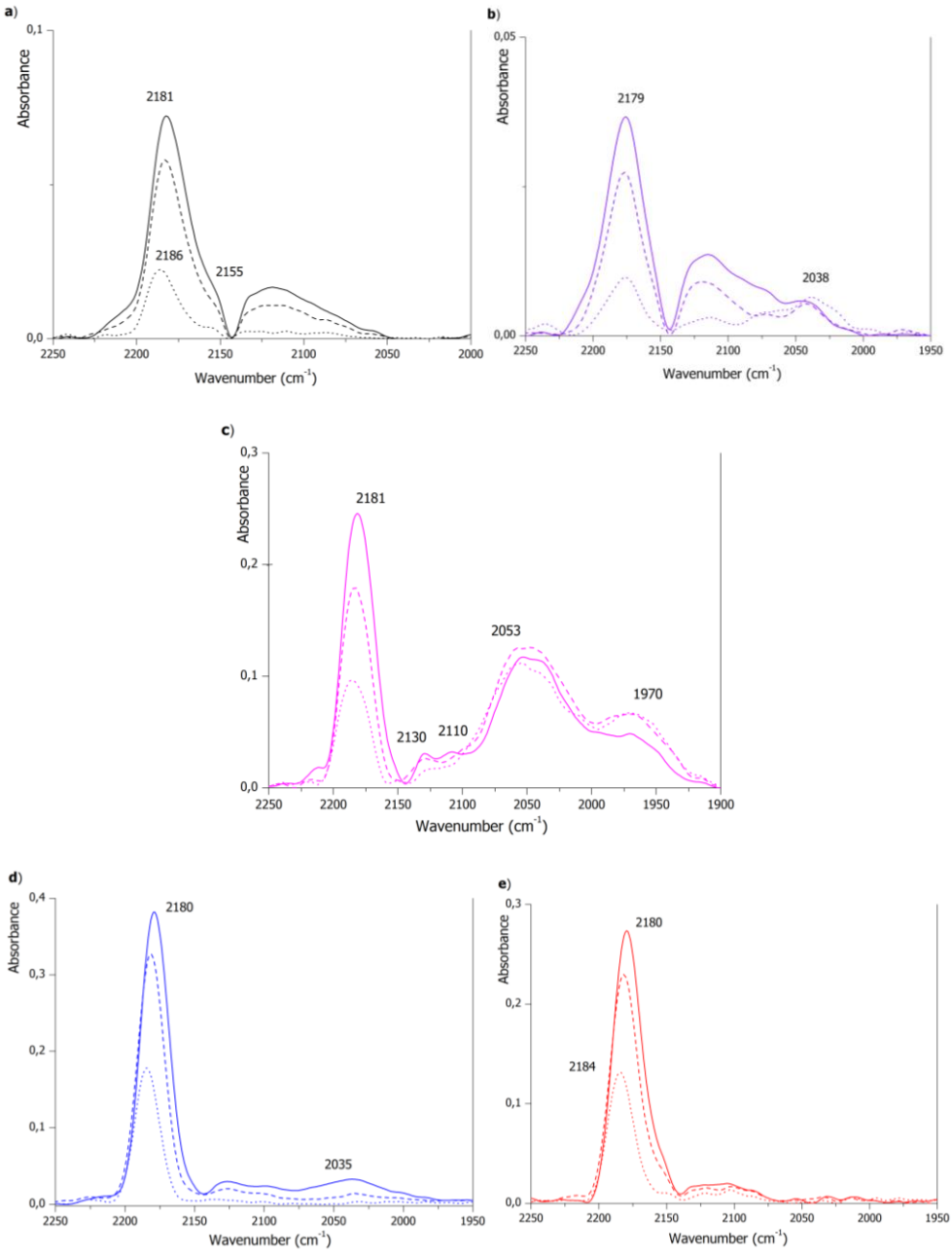

Figure 3.15. Differential FTIR spectra of CO adsorbed on (a) ZrO_2, (b) Ni0Z_en, (c) Ni0Z_2, (d) Ni1Z_10 and (e) Ni2Z_10. Solid line for 100 torr, dash line for 50 torr, dot line for 5 torr.

suggesting a negligible contribution of Ni^{2+} and a reduced presence of coordinative unsaturated surface cations. The weak signal at lower

wavenumbers could be ascribable to metallic Ni.[38] For Ni1Z_10 and Ni2Z_10 spectra, in Figure 3.15d and Figure 3.15e, it is possible to observe the strong signal at 2180 cm^{-1}, whose intensity suggests that is related both to Zr^{4+} and Ni^{2+} sites coordinated with CO[38,43]. In Ni1Z_10 spectra the weak peak at 2035 cm^{-1} could be related to metallic Ni.[38] It can be observed that signals related to metallic Ni are absent only in Ni2Z_10, where the impregnated Ni nitrate degraded into NiO during thermal treatment. On the contrary, when Ni in added in an intermediate step a metallic fraction is always detected when CO interacts with the surface, even if samples were treated in mild oxidative atmosphere prior to analysis. It can be noted that CO interaction with metallic nickel strongly depends on metal particle size.[38] Generally, linear and bridged forms are generated by CO adsorption on flat Ni surfaces, but when the surfaces are rough (and the metal particles are small) $Ni(CO)_4$ is formed. It can re-adsorb on the surface and generate many different species, complicating spectra interpretation. These results suggest that in those cases Ni is incorporated in the zirconia structure and also exposed on the surface and seems to be partially reduced. Results also suggest that for Ni0Z_en, Ni-doping does not enhance acid properties.

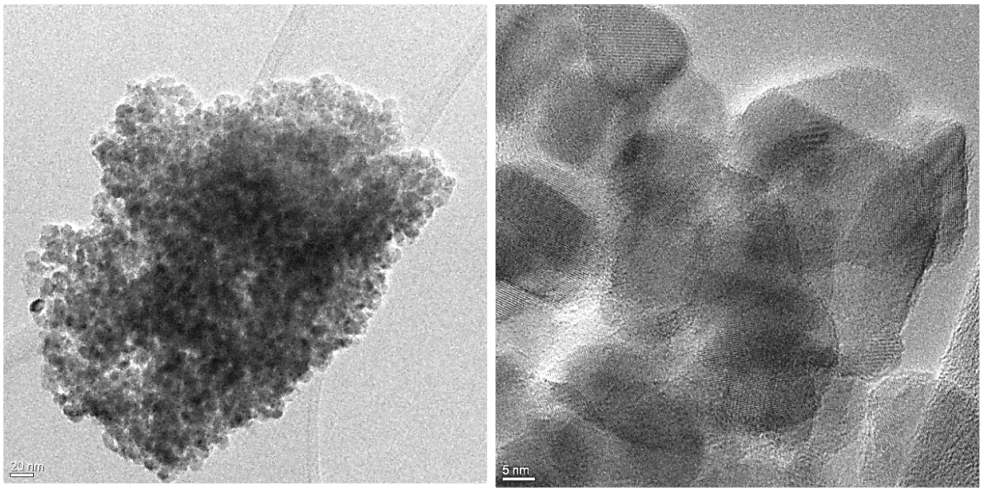

Figure 3.16. HR-TEM images of Ni0Z_2 at different magnification.

In order to find out both external habits of the crystallites and the possible location/shape of the Ni species, HR-TEM investigations were carried out: Figure 3.16 reports some images of Ni0Z_2 sample in which the presence of roundish crystallites, around 10 nm, with uniform size and distribution is evident. Particles exhibit a highly ordered habit, as it is quite simple to single out fringe patterns confirming the high crystallinity of the materials. The detailed inspections of the distances of the fringe patterns, and the parallel analysis of the diffraction patterns, indicate that the fringe patterns belong to (111) family planes of t-ZrO_2[22] and to different family planes of m-ZrO_2[45]. The presence of monoclinic planes could be related to the formation of this phase on particle surface. In fact, reported studies[46,47] demonstrate that nanocrystalline ZrO_2 particles within size range of 7-32 nm can exhibit a core-shell morphology with monoclinic phase in the 'shell' and tetragonal phase in the 'core'. In our particles the tetragonal phase is identified in the most ordering region, and the monoclinic phase in the more heterogeneous portions. This could suggest that when particles aggregate, a monoclinic phase may format the surface, whereas isolated particles maintain a pure tetragonal phase. EDS analysis does not give evidence of Ni presence in the surface (see Figure S3), confirming its incorporation into zirconia structure and formation of a solid solution.

Ni1Z_10 samples is made up of nanoparticles, which are heterogeneous both in shape and dimension, as evident is Figure 3.17 (a and b). It is possible to recognize the presence of very small Ni metallic particles on the zirconia surface. The poor crystallinity of the sample, already suggested by the low intensity of signals in PXRD, make impossible to recognize fringes pattern. EDS analysis (see Figure S4) indicates that Ni is present and heterogeneously dispersed in the material. Inspection of images of Ni2Z_10, presented in Figure 3.17 (c and d), reveals that also in this case the sample is heterogeneous, being composed of either very small

roundish nanoparticles (around 5 nm) and/or of aggregates of bigger size. Inspections of the distances of the fringe patterns indicate the presence of (101) family planes of t-ZrO_2[22], of different planes of m-ZrO2 and of NiO. EDS analysis (see Figure S5) indicate an high rate of Ni, if compared to Ni1Z_10, supporting the hypothesis that NiO is formed on t-ZrO_2 nanoparticles, while in Ni1Z_10 part of Ni is incorporated into zirconia lattice, promoting the formation of cubic phase.

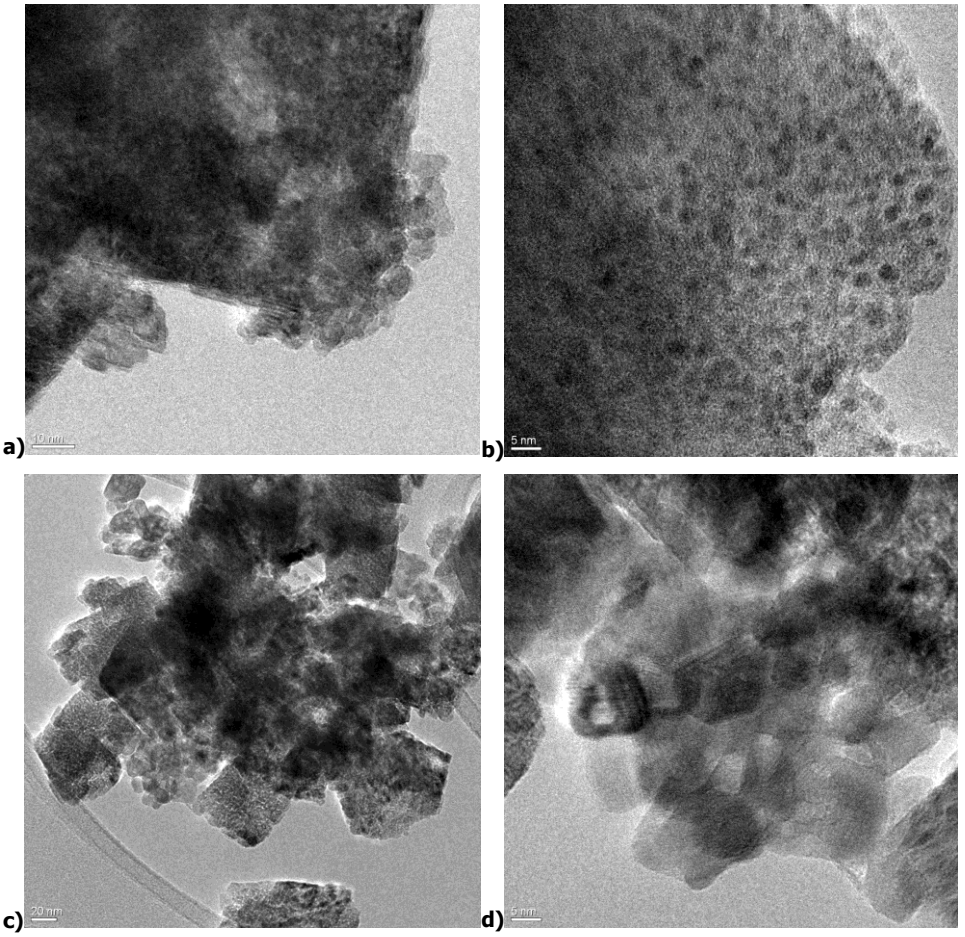

Figure 3.17. HR-TEM images of Ni1Z_10 (a and b) and Ni2Z_10 (c and d) at different magnification.

Ni0Z_2, Ni1Z_2 and Ni2Z_2 exhibit IV type adsorption isotherm curves with the characteristic hysteresis loop of a mesoporous material and loop

has a H4 shape (see Figure 3.18). Specific surface areas are reported in Table 3.2 and evidenced that while Ni0Z_2 has a SSA similar to undoped t-ZrO_2, impregnation of Ni leads to a decrease of the specific surface area of around 30%.

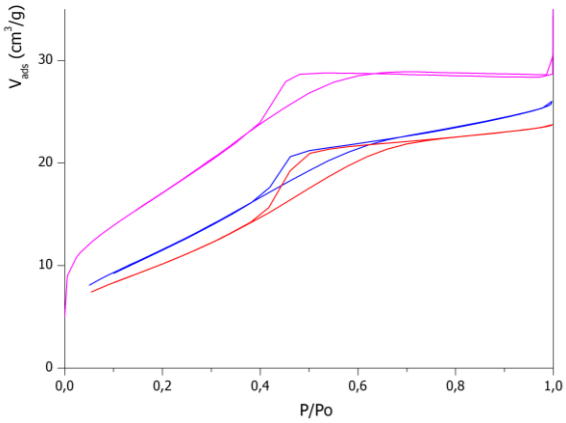

Figure 3.18. Adsorption/desorption isotherms of Ni0Z_2 (in pink), Ni1Z_2 (in blue) and Ni2Z_2 (in red).

Table 3.2. SSA of samples.

Sample	SSA (m^2/g)
t-ZrO_2	61
Ni0Z_2	64
Ni1Z_2	45
Ni2Z_2	39

We can conclude that three different behaviours are observed depending on the step of Ni addition. In particular: (i) When Ni is impregnated in t-ZrO_2 nanoparticles, crystalline NiO is formed on the particles' surface. Crystallinity of zirconia seems not to be affected, but specific surface area is drastically reduced. (ii) Impregnation on the still amorphous intermediate promotes the formation of cubic phase. The physic-chemical characterization suggest that Ni is incorporated in zirconia lattice as Ni^{2+}, and very small particles of metallic nickel are present on the surface. Ni incorporation causes a decrease of crystallinity and surface area, if compared to pure zirconia. (iii) The best way to obtained Ni-promoted zirconia appears to be adding metal during gel formation, and the best precursor is resulted to be nickel nitrate. Vibrational and structural data of Ni0Z suggested that the obtained material is a solid solution of Ni in tetragonal zirconia. Ni addition affects neither crystallinity nor surface area

compared to pure t-ZrO_2 obtained with the same synthetic procedure. Ni site of different nature are also present on material surface, as supported by CO absorption results. The presence of these sites could influence catalytic properties.

3.3 MW-assisted synthesis of sulfated zirconia

As reported before, the MW-assisted synthesis allows to obtain tetragonal zirconia, the crystalline phase that has been reported to have superior catalytic activity. We apply the proposed procedure to the synthesis of sulfated zirconia, a well-known solid acid catalyst.[48] Sulfated (from $(NH_4)_2SO_4$) were added by means of WI or IWI on xerogel or the already formed t-ZrO_2 (respectively indicate as S1Z and S2Z). In both cases, after impregnation dried powders are calcined by MW-assisted calcination. During the thermal treatment it is possible to observe the formation of a white smoke due to salt degradation. Ammonium sulfate is reported to thermally degrade around 200°C producing a gas mixture rich of NH_3.[49]

In the case of S1Z_WI, as shown in Figure 3.19, Raman spectra exhibit the typical pattern of t-ZrO_2[20,29], even if signals possess very low intensity. The broad band above 1000 cm^{-1} is supposed to be associate to sulfates with a more ionic character formed in the material. In S2Z_WI spectra it is possible to recognize signals of monoclinic phase (at 175, 186, 376 cm^{-1}) [29], absent before sulfation, as evident in Figure 3.19. PXRD data confirmed that sulfation on S2Z_WI induces modification on its crystal phase (Vm=0,04), while the lower intensity in S1Z_WI peaks suggests that sulfation on intermediate inhibits crystallization. In literature[50] it is known that sulfation on zirconia precursor lead to a stabilization of tetragonal phase, but in our case seems to promote a little growth of monoclinic fraction.

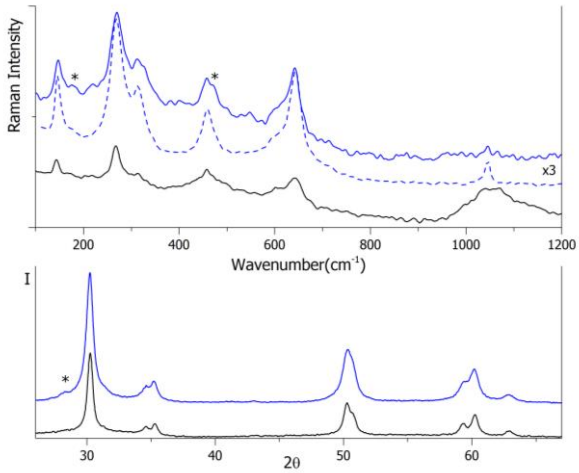

Figure 3.19. Raman spectra (on the top) and diffractograms of S1Z_WI (in black) and S2Z_WI (in blue), dot line for intermediate ZrO_2 prior impregnation. Stars indicate -monoclinic signals.

Figure 3.20 reports FTIR spectra relative to S1Z_WI and S2Z_WI, recorded after activation at 573 K in vacuum. In the vibrational region of surface sulfates (1400-1000 cm^{-1}) it is possible to recognize signal attributable to surface sulfates with a covalent configuration for S2Z, while for S1Z sulfate species seem to possess a more ionic character.[51] In fact, it has been demonstrated that the covalent character increases the separation of signals related to stretching mode of S=O and S–O, respectively around 1400 and 1050 cm^{-1}.[41] Other signals in the 1650-1200 cm^{-1} region are ascribable to residual water, carbonate and bicarbonate species adsorbed on the surface. At higher wavenumbers it is possible to observe signals related to water and -OH groups.[51] For S2Z both terminal OH component at 3755 cm^{-1} and a strong bridged OH component at 3670 cm^{-1} are detectable after activation, whereas for S1Z dehydration was not totally complete (as also suggested by the strong signal related to OH scissoring mode at 1630 cm^{-1}) and only a weak signal related to terminal OH can be singled out. Results suggest that: (i) sulfation is more effective on zirconia rather than on xerogel and (ii) a more crystalline product is obtained in the former case.

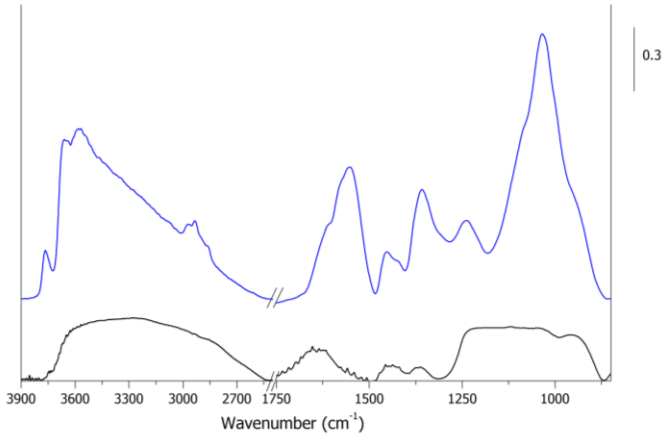

Figure 3.20. FT-IR spectra of S2Z_WI (in blue) and S1Z_WI (in black) in vacuum (activated at 573 K).

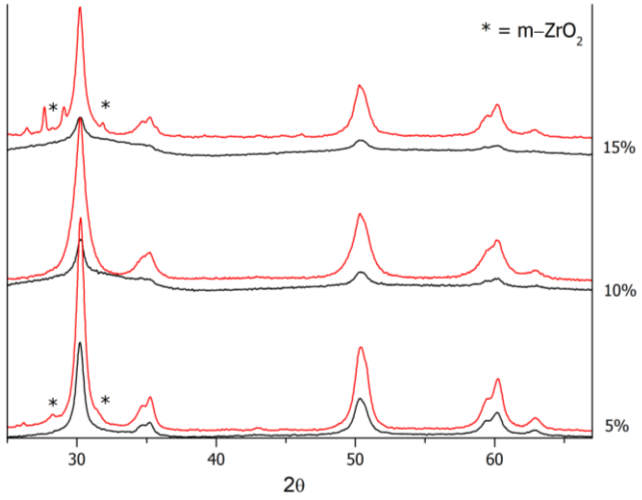

Figure 3.21. Diffractograms of S1Z (in black) and S2Z (in red), impregnated by IWI with sulfates at increasing wt%.

Sulfates were added in different synthetic steps at growing wt%. When IWI was made on xerogel (S1Z), structural and vibrational characterizations indicate that, as far as the amount of nominal sulfates increases, the material exhibits a partially amorphous structure. As evident in Figure 3.21, XRD peaks present in the S1Z_5 indicate the formation of the tetragonal phase[17]; whereas for S1Z_10 and S1Z_15 the presence of a still amorphous

fraction is suggested by the minor intensity of the peaks and by the broadening around 30°. Raman data (see Figure 3.22a) confirm these assumptions. S1Z_5 curve exhibits the pattern of t-ZrO_2[20], with signals at 149, 271, 317, 461, 602 and 646 cm^{-1}, and for S1Z_10 and S1Z_15 spectra are very similar to those reported for amorphous zirconia. The broad signal at 1050 cm^{-1} could be related to ionic sulfate groups. On the contrary, when sulfation by IWI was carried out on already formed t-ZrO_2 (S2Z), the obtained materials are crystalline, exhibiting the typical pattern of tetragonal phase both in the diffractograms[17]and the Raman spectra[20], as evidenced respectively in Figure 3.21 and Figure 3.22b. It is possible to note that S2Z_5 and S2Z_15 exhibit a small fraction of monoclinic phase (more evident in the PXRD data), and S2Z_15 also exhibit a series of peak at lower angles that is was not possible to assign.

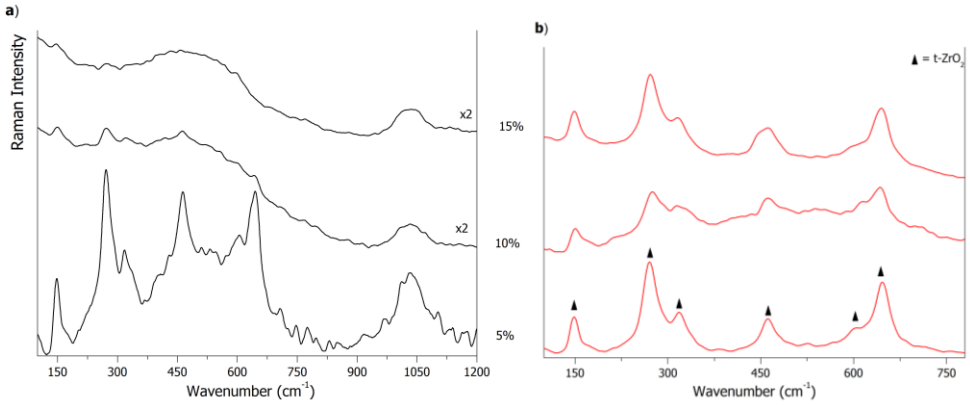

Figure 3.22. Raman spectra of S1Z (in black) and S2Z (in red), impregnated by IWI with sulfates at increasing wt%.

The nature of surface sulfates is better investigated by means of IR spectroscopy. ATR spectra (see Figure 3.23) of S1Z samples exhibit a signal around 1650 cm^{-1}, ascribable to the bending mode of water molecules and a broad band in the 1250-900 cm^{-1} range. These spectra are similar to that of $Zr(SO_4)_2$ [52] and indicate an ionic nature of sulfates on samples

impregnated on the intermediate. Band broadening in samples with higher sulfates loading is similar to that observed for S1Z_WI, supporting the hypothesis of the ionic character. For S1Z_5 the band is more structured, suggesting that at lower concentration, sulfates reached, almost in part, a covalent character.

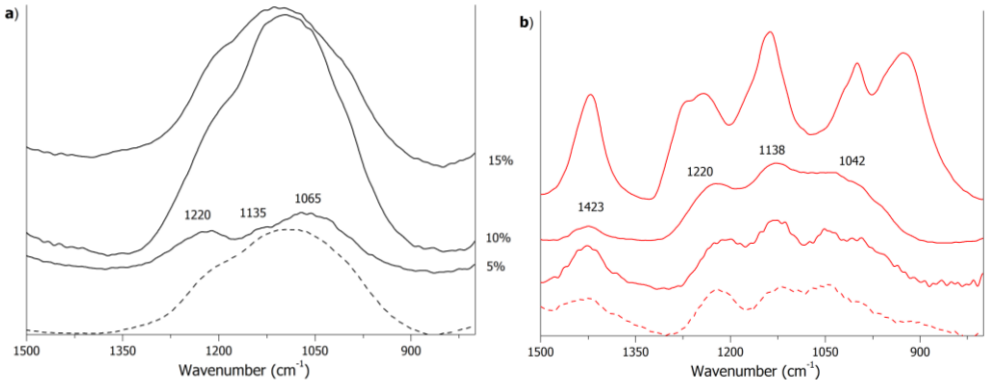

Figure 3.23. ATR spectra of S1Z (in black) and S2Z (in red), impregnated by WI (dash line) and by IWI (solid line) with sulfates at increasing wt%.

In the S2Z spectra, peak located at 1423 cm^{-1} is ascribable to the asymmetric stretching mode of the S=O bond of polynuclear sulfates as indicate in the literature[53], and the broad band at lower wavenumbers is ascribable to the stretching mode of S–O.[54,55] S2Z_5 and S2Z_10 have signals similar to that observed for S2Z_WI, suggesting a covalent character of sulfate groups. We can conclude that when sulfation is carried out on tetragonal ZrO_2, sulfate species with covalent character are present at the surface. FTIR spectra of S2Z_10 and S1Z_5, recorded in vacuum and after activation at 573 K, are presented in Figure 3.24. Samples exhibit similar signals at 1375 and 1030 cm^{-1}, attributable to sulfate groups covalently bonded to the surface.

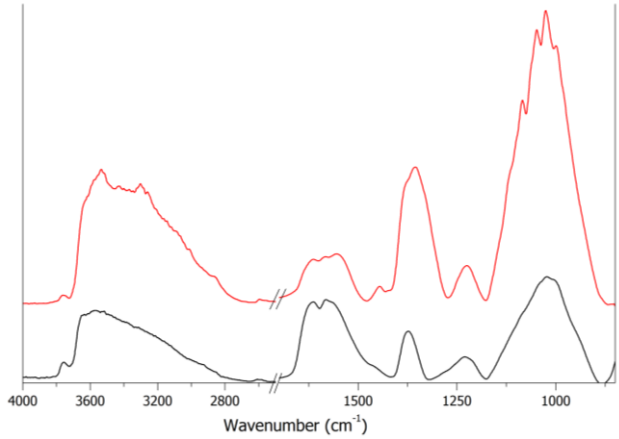

Figure 3.24. FT-IR spectra of S2Z_10 (in red) and S1Z_5 (in black) in vacuum, activated at 573 K.

We can conclude that sulfation is generally more effective if carried out on tetragonal zirconia with respect to the intermediate. In fact, in the former case covalent sulfate species are observed by vibrational spectroscopy characterization. Sulfation and the second thermal treatment seem have no effect on zirconia phase, that retains its tetragonal structure, even if some increase of the monoclinic fraction has been observed.

3.4 MW-assisted synthesis of sulfated Ni-zirconia

With the aim to investigate if the proposed procedure can lead to the synthesis of a bifunctional material, containing Ni and sulfate groups, we carried out a preliminary study comparing different preparation routes: (i) Ni and SO_4^{2-} on xerogel by WI (NiS1Z), (ii) Ni and SO_4^{2-} on t-$ZrO_2$by WI (NiS2Z), (iii) Ni on sulfated zirconia (S2Z_WI) by IWI (Ni3S2Z), (iv) SO_4^{2-} on Ni-promoted zirconia (S2Ni0Z_2) by IWI (S2Ni0Z).

Diffractograms and Raman spectra indicate that all samples are made up of tetragonal zirconia[17,29], as shown in Figure 3.25. Impregnation on the intermediate leads to a white powder (NiS1Z), that PXRD data suggests

being poorly crystalline and still partly amorphous, as confirmed by the Raman pattern ascribable to amorphous ZrO_2. The broad signal at 1050 cm^{-1} could be related to sulfates with ionic character. A similar behaviour has been observed in previous MW-assisted syntheses for xerogel impregnated by sulfates. Differently from Ni1Z samples, no cubic phase is ever present. This could be related to the different impregnation method (from solution or IWI), but also to the simultaneous presence of sulfate ions. Impregnation on zirconia particle (NiS2Z) seems to promote the formation of a small fraction of the monoclinic phase, observed in PXRD but not detectable in the vibrational data. A white powder was obtained, and no signals related to the formation of NiO was ever observable. On the contrary, when Ni nitrate is added by IWI on S2Z_WI (Ni3S2Z), a black powder is obtain and diffraction data indicate the formation of small fractions of crystalline NiO[28]. The intensity of the Raman signals ascribable to tetragonal zirconia is very low, but we can observe very intense diffraction peaks that suggest that crystallinity is not affect by impregnation and by subsequent thermal treatment. In fact, the peak ascribable to the monoclinic fraction was already present for the sulfated precursor, as evident in Figure 3.25. Nickel oxide seems to affect more Raman scattering and a similar behaviour has been observed for Ni2Z, suggesting that NiO crystallizes on the particle surface and affects surface scattering. When sulfation is carried out on Ni0Z_2 by IWI (S2Ni0Z), no substantial modifications are observed on the material, that retains the tetragonal phase. If compared to Ni0Z_2 precursor, both Raman signals and diffraction peaks suggest only a slight loss of crystallinity. These results suggest that WI seems not to be the appropriate method to add (or deposit) Ni on zirconia. Instead when Ni is added by IWI on SZ, NiO crystallizes on the particles surface.

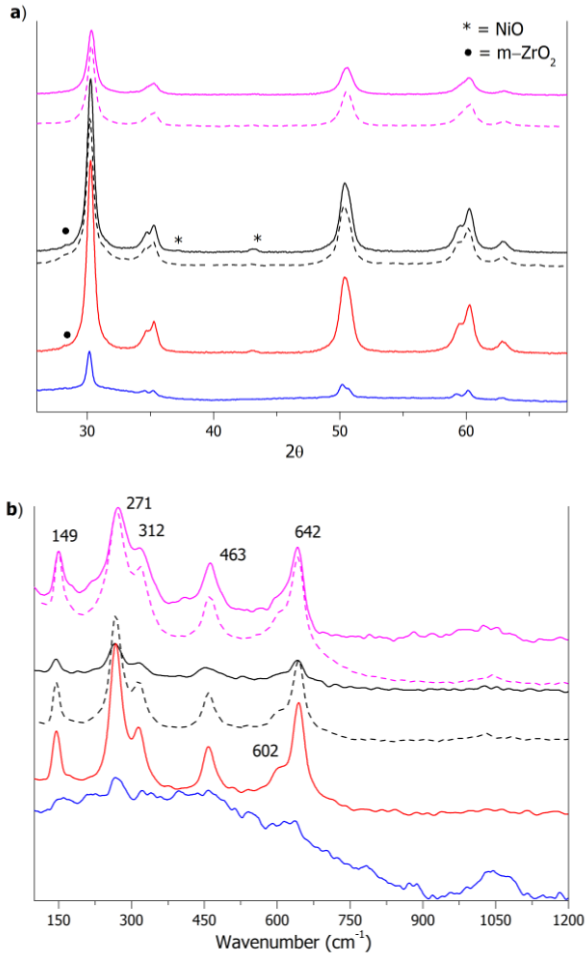

Figure 3.25. Diffractograms (a) and Raman spectra (b) of NiS1Z (in blue), NiS2Z (in red), Ni3S2Z (in black, dash line for S2Z_WI precursor) and S2Ni0Z (in pink, dash line for Ni0Z_2 precursor).

ATR spectra were recorded to investigate the nature of the sulfate species (in Figure 3.26). The broad band of NiS1Z suggest a ionic nature of the sulfate groups. The idea that impregnation on xerogel does not lead to the formation of catalytic active sites on zirconia surface is supported by similar results previously described for S1Z sample. The same signal is more structured in S2Ni0Z spectra, and the absence of similar signals in the spectrum of the precursor indicates that sulfate species with covalent character are formed on the powder surface. A similar band is less

structured in the Ni3S2Z spectrum, if compared to the precursor one, suggesting the Ni addition negatively affects also the nature of surface sulfate groups. No signal attributable to sulfate species is ever present for NiS2Z, confirming the hypothesis that this impregnation route is the least promising.

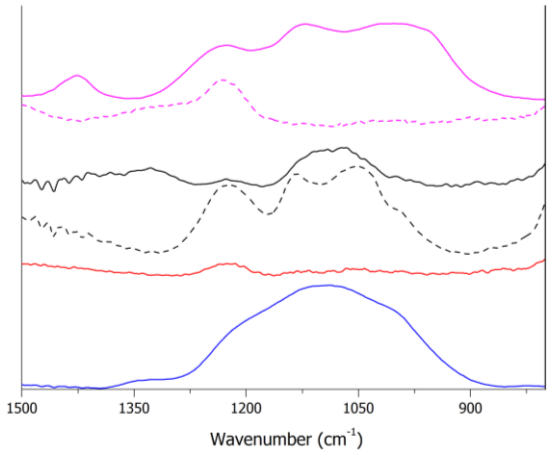

Figure 3.26. ATR spectra of NiS1Z (in blue), NiS2Z (in red), Ni3S2Z (in black, dash line for S2Z_WI precursor) and S2Ni0Z (in pink, dash line for Ni0Z_2 precursor).

In order to find out both habits of the crystallites and the location/shape of the Ni species, HR-TEM investigations were carried out on the most interesting samples: Ni3S2Z and S2Ni0Z. For the former (see the image in Figure 3.27a) it is evident that the obtained powder is heterogeneous: small nanoparticles are observed, whose average size is less than 10 nm, besides bigger aggregates. These aggregates, as evident in Figure 3.27b at higher magnification, seems to be slightly crystalline and holes are observed. Ni3S2Z underwent to three MW-assisted calcination, and probably these subsequent heating treatments affected particles crystallinity and influenced the formation of aggregates. EDS analysis (in Figure S6) evidences the presence of Ni and S on the surface, but their concentration is small and appears to be not uniform.

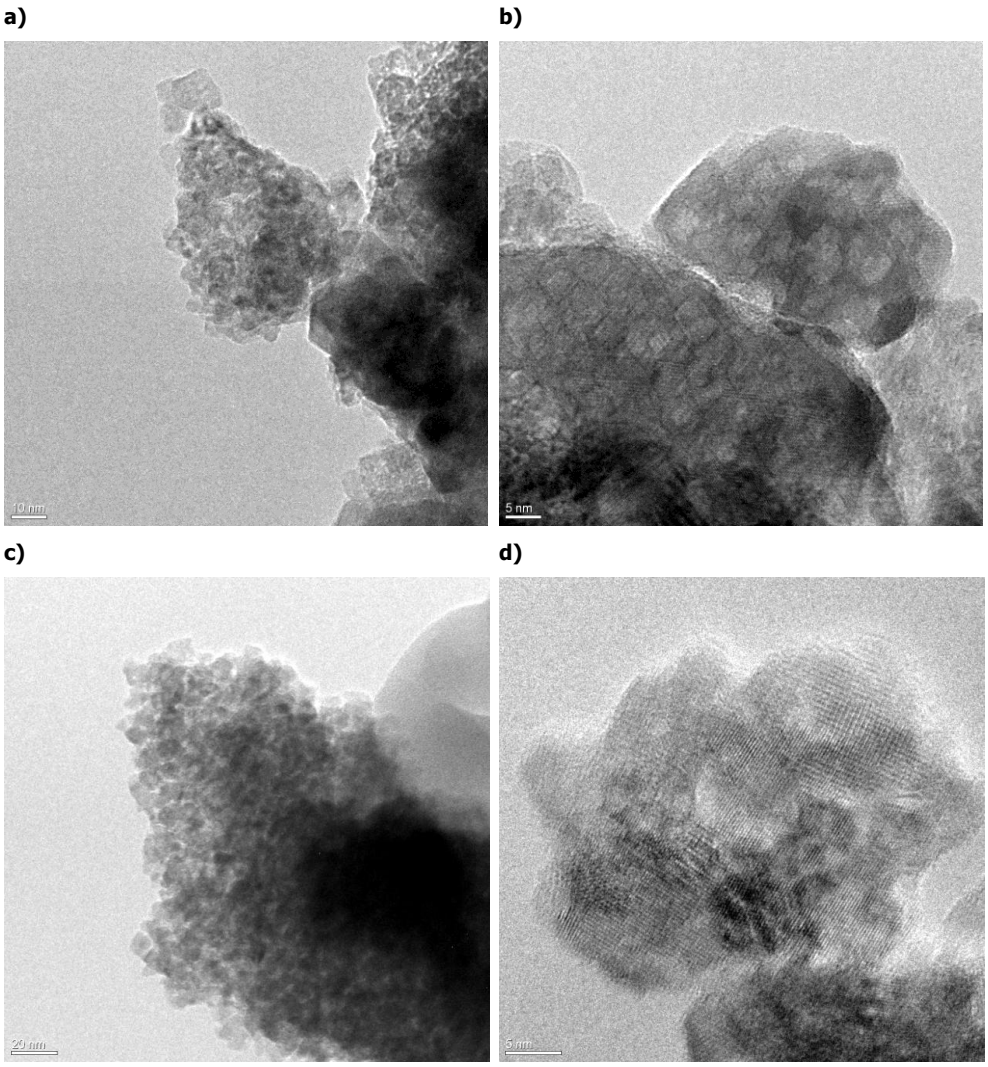

Figure 3.27. HR-TEM images at different magnification of Ni3S2Z (a and b) and S2Ni0Z (c and d).

In the case of S2Ni0Z, images suggest that this pink powder is composed by very small nanoparticles (less than 10 nm), as evident in Figure 3.27c. Particles exhibit a highly ordered habit, as it is quite simple to single out fringe patterns confirming the high crystallinity of the materials, as shown in Figure 3.27d. The detailed inspections of the distances of the fringe patterns, and the parallel analysis of the diffraction patterns, indicate

the many fringe patterns belong to the monoclinic family planes 100, 110, 111[45], analogously to Ni0Z. This supports the hypothesis that for Ni-promoted zirconia small core-shell nanoparticles are formed, and that the tetragonal stabilization seems to be promoted by the formation of a shell of monoclinic phase. EDS analysis evidences a not uniform presence of Ni and S species on the particles.

The nature of the surface (i.e., its acid/basic/redox character) was further investigated on the best product S2Ni0Z by FTIR spectroscopy, using CO and 2,6-dimethylpyridine (2,6-DMP) as probe molecules. Carbon monoxide allows to investigate the nature of metal sites and so to recognize the presence of Ni, but also indicate the presence of Lewis acid sites.[42] 2,6-DMP allows the identification of both Lewis and Brønsted acidic centers present at the surface of an oxide, even distinguish sites of different strength.[56,57] Differential spectra are presented in Figure 3.28. Upon CO adsorption, a strong signal is present at 2194 cm^{-1}, whose intensity decreases after desorption. A similar behavior has been reported for sulfated zirconia as were.[43] The comparison of intensity, with ZrO_2 and Ni0Z_2 (in Figure 3.15), suggests that for S2Ni0Z the signal is partially due CO coordinated on Ni^{2+} sites. Differently to the starting Ni0Z_2 samples, no signal is detectable at lower wavenumbers. Previous characterizations suggest that Ni0Z_2 is a solid solution of zirconia and Ni^{2+}, and Ni sites of different nature are exposed on the surface. In S2Ni0Z, part of the surface is occupied by thermally stable sulfate groups and a lower amount of coordinatively unsaturated surface cations can become exposed. Absorption of 2,6-DMP evidences the presence of Brønsted and Lewis acidic sites, presenting spectra similar to those reported for tetragonal sulfated zirconia.[57] In particular the formation of lutidinium for absorption on Brønsted sites yields to two strong bands centered at 1647 and 1628 cm^{-1},

whereas multiple band at lower frequencies are ascribable to Lewis-bonded (1601 cm^{-1}) and H-bonded species (1594 and 1580 cm^{-1}) 2,6-DMP species.

Characterization results suggest that the most appropriate way to synthesize a bifunctional material is to impregnate sulfate of Ni-promoted zirconia. On the surface of the high crystalline material Lewis and Brønsted acidic sites were detected by basic probe.

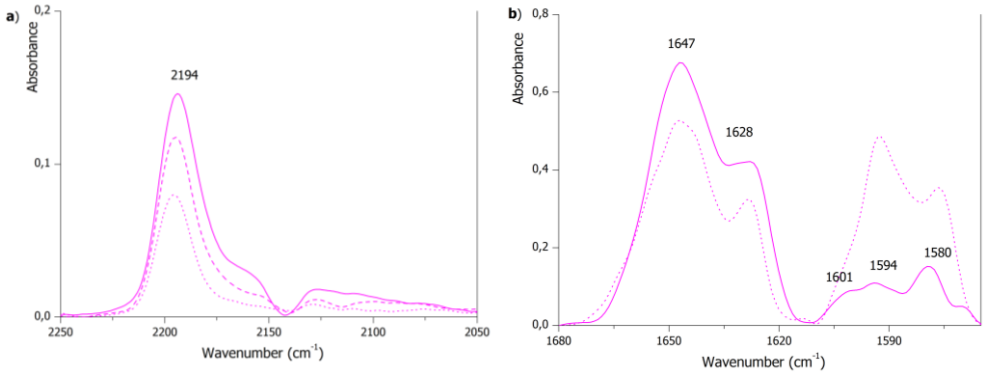

Figure 3.28. Differential FTIR spectra of (a) CO adsorbed on S2Ni0Z (solid line for 100 torr, dash line for 50 torr, dot line for 5 torr); (b) adsorption/desorption of 2,6-DMP on S2Ni0Z (dash line under maximum pressure of 2,6-DMP, solid line after evacuation for 15 min).

In summary, the proposed MW-assisted sol-gel synthesis has proved to be a very efficient method to obtain high crystalline tetragonal zirconia nanoparticles. The proposed procedure was the applied for the synthesis of other zirconia-base materials: (i) sulfated zirconia, (ii) Ni-promoted zirconia and (iii) sulfated Ni-ZrO_2. The preliminary studies on Ni-containing materials indicate that the crystal phase and surfaces properties strongly depend on the nickel addition step. For sulfated zirconia (SZ) the nature of surface sulfate species is influenced by impregnation methods and starting precursor. It can be obtained SZ samples that presents sulfates with a covalent character, that could be employed as solid acid catalyst in glucose hydrolysis. On the basis of physicochemical characterizations, the most

crystalline samples, whose surface sulfates exhibiting the stronger covalent character were chosen as catalysts: S2Z_WI, S1Z_5 and S2Z_8.

---

[1] H.H. Kung, E.I. Ko, Preparation of oxide catalysts and catalyst supports a review of recent advances, *Chem. Eng. J.* **1996** (64), 203–214.

[2] X. Bokhimi, A. Morales, O. Novaro, M. Portilla, T. López, F. Tzompantzi, R. Gómez, Tetragonal Nanophase Stabilization in Nondoped Sol–Gel Zirconia Prepared with Different Hydrolysis Catalysts, *J. Solid State Chem.* **1998** (135), 28–35.

[3] B.E. Yoldas, Zirconium oxides formed by hydrolytic condensation of alkoxides and parameters that affect their morphology, *J. Mater. Sci.* **1986** (21), 1080–1086.

[4] A. Ayral, T. Assih, M. Abenoza, J. Phalippou, A. Lecomte, A. Dauger, Zirconia by the gel route, *J. Mater. Sci.* **1990** (25), 1268–1274.

[5] H.J. Kitchen, S.R. Vallance, J.L. Kennedy, N. Tapia-Ruiz, L. Carassiti, A. Harrison, A.G. Whittaker, T.D. Drysdale, S.W. Kingman, D.H. Gregory, Modern Microwave Methods in Solid-State Inorganic Materials Chemistry: From Fundamentals to Manufacturing, *Chem. Rev.* **2014** (114), 1170–1206.

[6] B. Panzarella, G.A Tompsett, K.S. Yngvesson, W.C. Conner, Microwave Synthesis of Zeolites. 2. Effect of Vessel Size, Precursor Volume, and Irradiation Method, *J. Phys. Chem. B* **2007** (111), 12657–12667.

[7] Y.-J. Zhu, F. Chen, Microwave-assisted preparation of inorganic nanostructures in liquid phase, *Chem. Rev.* **2014** (114), 6462−6555.

[8] S.K. Seol, D. Kim, S. Jung, Y. Hwu, Microwave synthesis of gold nanoparticles: Effect of applied microwave power and solution pH, *Mater. Chem. Phys.* **2011** (131), 331−335.

[9] P.K. Shen, S.B. Yin, Z.H. Li, C. Chen, Preparation and performance of nanosized tungsten carbides for electrocatalysis, *Electrochim. Acta* **2010** (55), 7969−7974.

[10] E.K. Plyler, Infrared Spectra of Methanol, Ethanol, and n-Propanol, *J. Res. Nat. Bur. Stand.* **1952** (48, 4), 281–286.

[11] C.M. Phillippi, K.S. Mazdiyasni, Infrared And Raman Spectra Of Zirconia Polymorphs, *J. Am. Ceram. Soc.* **1971** (54), 254−258.

[12] M. Bhattacharya, T. Basak, A review on the susceptor assisted microwave processing of materials, *Energy* **2016** (97), 306−338.

[13] A. Mirzaei, G. Neri, Microwave-assisted synthesis of metal oxide nanostructures for gas sensing application: A review, *Sens. Actuat. B-Chem.* **2016** (237), 749–775.

[14] P. Priecel, J.A. Lopez-Sanchez, Advantages and Limitations of Microwave Reactors: From Chemical Synthesis to the Catalytic Valorization of Biobased Chemicals, *ACS Sustainable Chem. Eng.* **2019** (7), 3−21.

[15] N.N. Greenwood, A. Earnshaw, Chemistry of the Elements, 2nd Edition, Elsevier Ltd, 1997.

[16] K. Nakamoto, Infrared and Raman Spectra of Inorganic and Coordination Compounds, 6th Edition, John Wiley & Sons, Inc., Hoboken, New Jersey, 2009.

[17] Tetragonal-ZrO_2: ICSD 42−1164.

[18] K.S. Rejitha, S. Mathew, Thermal behaviour of nickel(II) sulphate, nitrate and halide complexes containing ammine and ethylenediamine as ligands Kinetics and evolved gas analysis, *J. Therm. Anal. Calorim.* **2011** (106), 267−275.

[19] P.D. Southon, J.R. Bartlett, J.L. Woolfrey, B. Ben-Nissan, Formation and Characterization of an Aqueous Zirconium Hydroxide Colloid, *Chem. Mater.* **2002** (14), 4313−4319.

[20] C. Morterra, G. Cerrato, G. Meligrana, M. Signoretto, F. Pinna, G. Strukul, Catalytic activity and some related spectral features of yttria-stabilised cubic sulfated zirconia, *Catal. Lett.* **2001** (73), 113–119.

[21] Monoclinic-ZrO_2: ICSD 37–1484.

[22] Tetragonal-ZrO_2: PDF 01–088-1007.

[23] H. Toraya, M. Yoshimura, S. Somiya, Calibration Curve for Quantitative Analysis of the Monoclinic-Tetragonal ZrO2 System by X-Ray Diffraction, *J. Am. Ceram. Soc.* **1984** (67,6), C119–C121.

[24] J.A.M. Tabares, M.J. Anglada, Quantitative Analysis of Monoclinic Phase in 3Y-TZP by Raman Spectroscopy, *J. Am. Ceram. Soc*. **2010** (93,6), 1790–1795.

[25] G. Katagiri, H. Ishida, A. Ishitani, T. Masaki, Direct Determination by Raman Microprobe of the Transformation Zone Size in Y_2O_3 containing Tetragonal ZrO_2 Polycrystals; in *In Science and Technology of Zirconia III*, American Ceramic Society, Westerville, OH, **1988**, pp. 537–544.

[26] C.S. Lim, T.R. Finlayson, F. Ninio, J.R. Griffiths, 'In-Situ Measurement of the Stress-Induced Phase Transformation in Magnesia-Partially-Stabilized Zirconia Using Raman Spectroscopy, *J. Am. Ceram. Soc.* **1992** (75, 6), 1570–1573.

[27] Cubic-ZrO_2: ICSD 27–0997.

[28] NiO: ICSD 64–6099.

[29] E.F. Lopez, V.S. Escribano, M. Panizza, M.M. Carnascialic, G. Busca, Vibrational and electronic spectroscopic properties of zirconia powders, *J. Mater. Chem.* **2001** (11), 1891–1897.

[30] D. Kim, H. Jung, Raman Spectroscopy of Tetragonal Zirconia Solid Solutions, *J. Am Ceram. Soc.* **1993** (76, 8), 2106–2108.

[31] N.T. McDevitt, W.L.Baun, Infrared absorption study of metal oxides in the low frequency region (700-240 cm^{-1}), *Spectrochim. Acta* **1964** (20, 5), 799–808.

[32] M. Valigi, D. Gazzoli, R. Dragone, M. Gherardi, G. Minelli, Nickel Oxide-Zirconium Oxide: Ni^{2+} Incorporation and its Influence on the Phase Transition and Sintering of Zirconia, *J. Mater. Chem.* **1995** (5, 1), 183–189.

[33] W.E. Alvarez, H. Liu, E.A. Garcia, E.H. Rueda, A.J. Rouco, D.E. Resasco, n-Butane isomerization on Ni-prornoted sulfated zirconia catalysts, *Stud. Surf. Sci. Catal.* **1996** (101), 553–562.

[34] R.W. Cairns, E. Ott, X-Ray Studies of the System Nickel–Oxygen–Water. I. Nickelous Oxide and Hydroxide, *J. Am. Chem. Soc.* **1933** (55,2), 527–533.

[35] R.D. Shannon, Revised effective ionic radii and systematic studies of interatomic distances in halides and chalcogenides, *Acta Cryst.* **1976** (A32), 751–766.

[36] B. Małecka, A. Łacąz, E. Drożdż, A. Małecki, Thermal decomposition of d-metal nitrates supported on alumina, *J. Therm. Anal. Calorim.* **2015** (119), 1053–1061.

[37] J. Von Hoene, R.G. Charles, W.M. Hickam, Thermal Decomposition of Metal Acetylacetonates: Mass Spectrometer Studies, *J. Phys. Chem.* **1958** (62, 9), 1098–1101.

[38] M. Mihaylov, O. Lagunov, E. Ivanova, K. Hadjiivanov, Determination of Polycarbonyl Species on Nickel-Containing Catalysts by Adsorption of CO Isotopic Mixtures, *Top Catal.* **2011** (54), 308–317.

[39] M. Mihaylov, K. Chakarova, K. Hadjiivanov, Formation of carbonyl and nitrosyl complexes on titania- and zirconia-supported nickel: FTIR spectroscopy study, *J. Catal.* **2004** (228), 273–281.

[40] K. Góra-Marek, A. Glanowska, J. Datka, Quantitative IR studies of the concentration of different nickel sites in NiZSM-5 zeolites,*Micropor. Mesopor. Mat.* **2012** (158), 162–169.

[41] C. Morterra, G. Cerrato, M. Signoretto, On the role of the calcination step in the preparation of active (superacid) sulfated zirconia catalysts, *Catal. Lett.* **1996** (41), 101–109.

[42] V. Bolis, B. Fubini, E. Garpone, C. Morterra, P. Ugliengo, Induced Heterogeneity at the Surface of Group 4 Dioxides as revealed by CO Adsorption at Room Temperature, *J. Chem. Soc. Faraday T.* **1992** (88, 3), 391–398.

[43] C. Morterra, G. Cerrato,V. Bolis,S. Di Ciero**,** M. Signoretto, On the strength of Lewis- and Brønsted-acid sites at the surface of sulfated zirconia catalysts, *J. Chem. Soc., Faraday T.* **1997** (93, 6), 1179–1184.

[44] V. Bolis, G. Cerrato, G. Magnacca, C. Morterra, Surface acidity of metal oxides. Combined microcalorimetric and IR-spectroscopic studies of variously dehydrated systems, *Thermochim. Acta* **1998** (312), 63–77.

[45] Monoclinic ZrO_2: PDF 01–083–0937.

[46] R. Nitsche, M. Winterer, H. Hahn, Structure of nanocrystalline zirconia and yttria, *Nanostruct. Mater.* **1995** (6), 679–682.

[47] R. Nitsche, M. Rodewald, G. Skandan, H. Fuess, H. Hahn, HRTEM study of nanocrystalline zirconia powders, *Nanostruct. Mater.* **1997** (7), 535–546.

[48] G.D. Yadav, J.J. Nair, Sulfated zirconia and its modified version as promising catalyst for industrial processing, *Micropor. Mesopor. Mat.* **1999** (33), 1–48.

[49] R. Kiyoura, K. Urano, Mechanism, Kinetics, and Equilibrium of Thermal Decomposition of Ammonium Sulfate, *Ind. Eng. Chem. Process Des. Develop.* **1970** (9,4)**,** 489–494.

[50] G.X. Yan, A. Wang, I.E. Wachs, J. Baltrusaitis, Critical review on the active site structure of sulfated zirconia catalysts and prospects in fuel production, *Appl. Catal., A* **2019** (572), 210–225.

[51] C. Morterra, G. Cerrato, F. Pinna, M. Signoretto, G. Strukul, On the acid-catalyzed Isomerization of light paraffins over a ZrO_2/SO_4 system: the effect of hydration, *J. Catal.* **1994** (149), 181–188.

[52] E.E. Platero, M.P. Mentruit, IR characterization of sulfated zirconia derived from zirconium sulfate, *Catal. Lett.* **1995** (30), 31–39.

[53] C. Morterra, G. Cerrato, V. Bolis, Lewis and Brønsted acidity at the surface of sulfate doped ZrO_2 catalysts, *Catal. Today* **1993** (17), 505–515.

[54] C. Sarzanini, G. Sacchero, F. Pinna, M. Signoretto; G. Cerrato, C. Morterra, Amount and nature of sulfates at the surface of sulfate-doped zirconia catalysts, *J. Mater. Chem.* **1995** (5, 2), 353–360.

[55] C. Morterra, G. Cerrato, S. Ardizzone, C.L. Bianchi, M. Signoretto, F. Pinna, Surface features and catalytic activity of sulfated zirconia catalysts from hydrothermal precursors, *Phys. Chem. Chem. Phys.* **2002** (4), 3136–3145.

[56] C. Morterra, G. Cerrato, G. Meligrana, Revisiting the Use of 2,6-Dimethylpyridine Adsorption as a Probe for the Acidic Properties of Metal Oxides, *Langmuir* **2001** (17), 7053–7060.

[57] C. Morterra, G. Meligrana, G. Cerrato, V. Solinas, E. Rombi, M. F. Sini, 2,6-Dimethylpyridine Adsorption on Zirconia and Sulfated Zirconia Systems. An FTIR and Microcalorimetric Study, *Langmuir* **2003** (19), 5344–5356.

4. SZ AS CATALYST IN GLUCOSE HYDROLISYS

Sulfated zirconia (SZ) samples were tested as catalysts in glucose hydrolysis for the production of platform chemicals, as either 5-hydroxymethylfurfural (5-HMF) or levulinic acid (LA). It is widely accepted that the reaction pathways for HMF and LA are quite similar and the overall reaction scheme proposed for acid catalyzed hydrolysis of glucose is shown in Scheme 4.1. This reaction is consecutive and involves various steps, catalysed by either Lewis or Brønsted acidic sites present at the surface of the solid catalyst. Glucose conversion has been proposed to start via Lewis acid catalysed isomerization to fructose, followed by several Brønsted acid catalysed dehydration/hydration reactions. Fructose dehydration provides HMF, that can be further converted in LA and formic acid (FA) by acid hydrolysis. Humins are unavoidable by-products in the acid catalyzed hydrolysis step, and can significantly affect yield. Humins can cause catalyst deactivation and adsorb intermediates and substrates.[1]

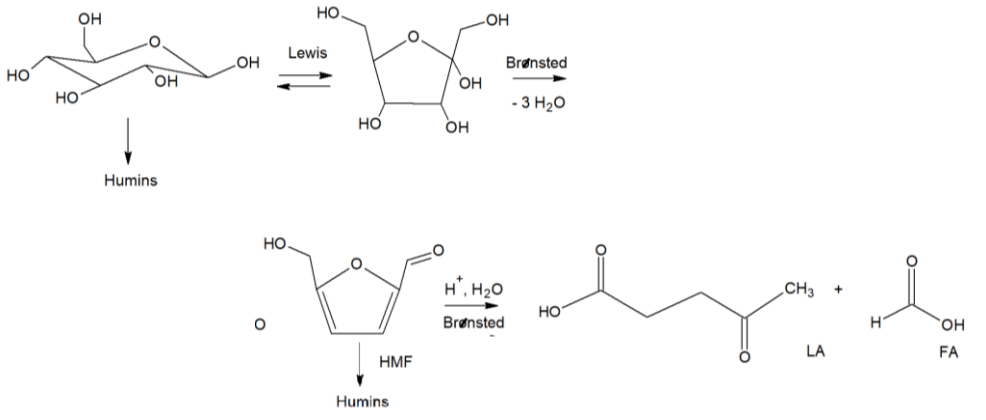

Scheme 4.1. Reaction pathway proposed for glucose acid hydrolysis.

Osatiashtiani et al[2] reported that for SZ an appropriate mix of Lewis and Brønsted sites are required for the tandem isomerization of glucose to

fructose and the latter's subsequent dehydration to 5-HMF. In fact, their studies evidenced that unsulfated monoclinic zirconia, possessing only Lewis sites, is effective for glucose isomerisation to fructose but poorly active towards fructose dehydration to 5-HMF, while using sulfated tetragonal zirconia, possessing a significant Brønsted acidity, the 5-HMF production is enhanced. Another study[3] on acid-catalyzed dehydration of fructose to 5-HMF reported that SZ in water solvent has low catalytic activity in these conditions. On the contrary, in non-aqueous solution SZ promotes a high fructose conversion with high 5-HMF yield.

Lewis and Brønsted acidity are related to both nature and the amount of sulfate ions, that are so fundamental parameters to be tuned in order to improve catalyst activity. The nature of surface sulfates, and nature and the strength of surface acidity as well, is influenced by the preparation method and thus we compared our catalysts to a 'model' SZ system (i.e. obtained by a standard precipitation route)[4,5,6] and named this as SZ_prec. SZ_prec is composed by nanoparticles possessing tetragonal phase, as suggested by structural and vibrational characterizations (see Figure S7). Three SZ samples obtained by MW-assisted sol-gel synthesis, as previously described, were tested and compared to SZ_prec. In these MW-assisted samples sulfation was carried out using the same precursor (i.e., ammonium sulfate), by impregnation in different synthetic steps: (i) S2Z_WI (by WI on t-ZrO_2), (ii) S1Z_5 (by IWI on xerogel) and (iii) S2Z_8 (by IWI on t-ZrO_2). All these samples consist then of sulfated zirconia in tetragonal phase, as discuss previously for S2Z_WI and S1Z_5 and as it has been shown in Figure S8 for S2Z_8.

4.1 Surface properties of the catalysts

We suppose that an important parameter which can influence both reaction pathway and selectivity is the nature of the sulfate groups present on the zirconia surface, that generates Lewis and Brønsted sites of different strength on the surface of the catalysts. Further investigations have been carried out by infrared spectroscopy to investigate and understand the nature of these sites in the catalysts obtained by MW-assisted synthesis and comparing them to the 'model' SZ. The nature of surface sulfates depends on several preparative parameters, as (i) the temperature of the thermal treatment, (ii) the crystal phase of zirconia and (iii) the overall sulfates content.[5,7] It has been proposed that the amount of surface sulfates does not give *per se* all information concerning the properties of a sulfated zirconia catalyst, being the nature of the sulfates more important than just its presence.[7] Sulfate groups formed at the surface of metal oxides are known to possess a highly heterogeneous nature, and they are characterized by complex spectral features.

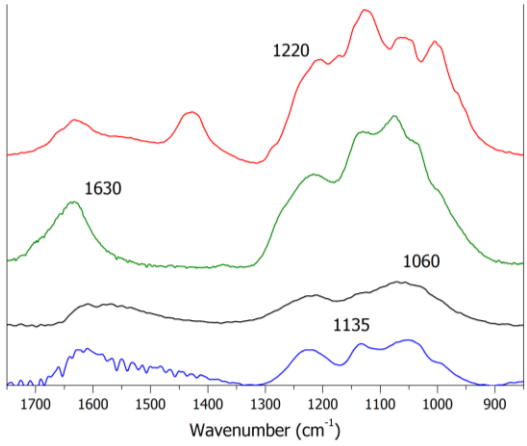

Figure 4.1. ATR spectra of S2Z_WI (in blue), S1Z_5 (in black), SZ_prec (in green) and S2Z_8 (in red) in the 1750-850 cm^{-1} spectral region.

Nature and IR spectral features of surface sulfates are affected by the overall degree of surface hydration. On highly hydrated surface, as those observed in the ATR spectra reported in Figure 4.1, the formation of several broad bands in the 1200-900 cm^{-1} range, and have been related to sulfates mainly in an ionic configuration, resembling that of inorganic (bidentate) sulfato complexes.[8,9] It is possible to recognize signals ascribable to other species adsorbed onto the surface, as the strong broad band located at 1630 cm^{-1} and due to adsorbed/coordinated undissociated water (bending or scissor mode) molecules. The component due to sulfate species is less structured for S1Z_5, suggesting a different nature of surface sulfates in this catalyst. On medium-highly dehydrated surfaces, sulfates tend to acquire a more covalent configuration, that allows to better discriminate their nature: at higher frequencies (ν > 3000 cm^{-1}), as shown in Figure 4.2a, we can observe signals due to the stretching (ν_{OH}) of "free" hydroxyl groups. For SZ_prec there is a weak band centred at 3745 cm^{-1}, ascribable to terminal OH groups, and a strong band at 3645 cm^{-1} that has been ascribed to bridged OH groups, similar to that reported for t-ZO_2/SO_4.[10,11] For samples obtained by MW-assisted synthesis, we can observe signal of terminal OH groups at 3765 cm^{-1} and a broad band at lower wavenumbers related to the stretching modes of both bridged hydroxyls (shoulder/component around 3650 cm^{-1}) and to OH groups involved in weak perturbation of the H-bonding (broad envelope in the lower part of the spectra). The presence of this broad band and of another around 1600 cm^{-1} (related to water scissoring mode) suggests that only a low-medium degree of dehydration is achieved on these samples after treatment at 300 °C.

In the early stage of dehydration, elimination of adsorbed/coordinated undissociated water causes a shift of the related band at lower wavenumbers, as evident in Figure 4.2c, but signals remain quite similar after activation. On the surface of MW-assisted calcined materials seems to

be present also carbonate species that are not removed after activation at this mild temperature. For S2Z_WI a broad band at ~1560 cm^{-1} and signal at 1450 cm^{-1} are quite evident: they may be ascribed, respectively, to bi- and mono- dentate carbonate[12]. In S1Z_5 and S2Z_8 spectra, these signals are less recognizable, but the presence of carbonate species could be responsible of the broadening of the sulfates bands. No similar signals are present in the SZ_prec spectrum, suggesting that carbonate species are formed on the surface of the material during the MW-thermal treatment, that is carried out in static atmosphere and in presence of incandescent graphite.

FTIR spectra of SZ_prec, in Figure 4.2b, are similar to those reported for comparable systems and indicate a highly covalent character of surface sulfate.[7] In the early stages of surface dehydration most of the sulfates have already assumed a covalent configuration (bands at ν>1350 cm^{-1} and at ca 1080 cm^{-1}), but a residual amount of sulfates still exhibits a mainly ionic configuration (bands at 1250 and below 1140 cm^{-1}). Activated sample shows: (i) an intense signal at 1395 cm^{-1} related to the S=O asymmetric stretching mode, (ii) a broad band at ca 1070 cm^{-1} due to the S–O stretching and (iii) a weak peak at 1180 cm^{-1} ascribable to the ν(O=S=O) symmetric mode. The increase of spectral separation between high and low frequency modes is ascribable to a high covalent character of sulfates.[13] S2Z_8 and S2Z_WI exhibit comparable behaviour after activation, as shown in Figure 4.2b-c. The band of the $\nu_{S=O}$ mode at 1360 cm^{-1} is broad and relatively weak, and the broad band of ν_{S-O} mode is centred at ≈ 1030 cm^{-1}: both are attributable to sulfate species with a covalent character. There is also a broad and complex band centred at 1230 cm^{-1}, suggesting that part of surface sulfates still possesses a mainly ionic character, and S2Z_WI seems to present a major fraction of surface sulfates with covalent configuration.

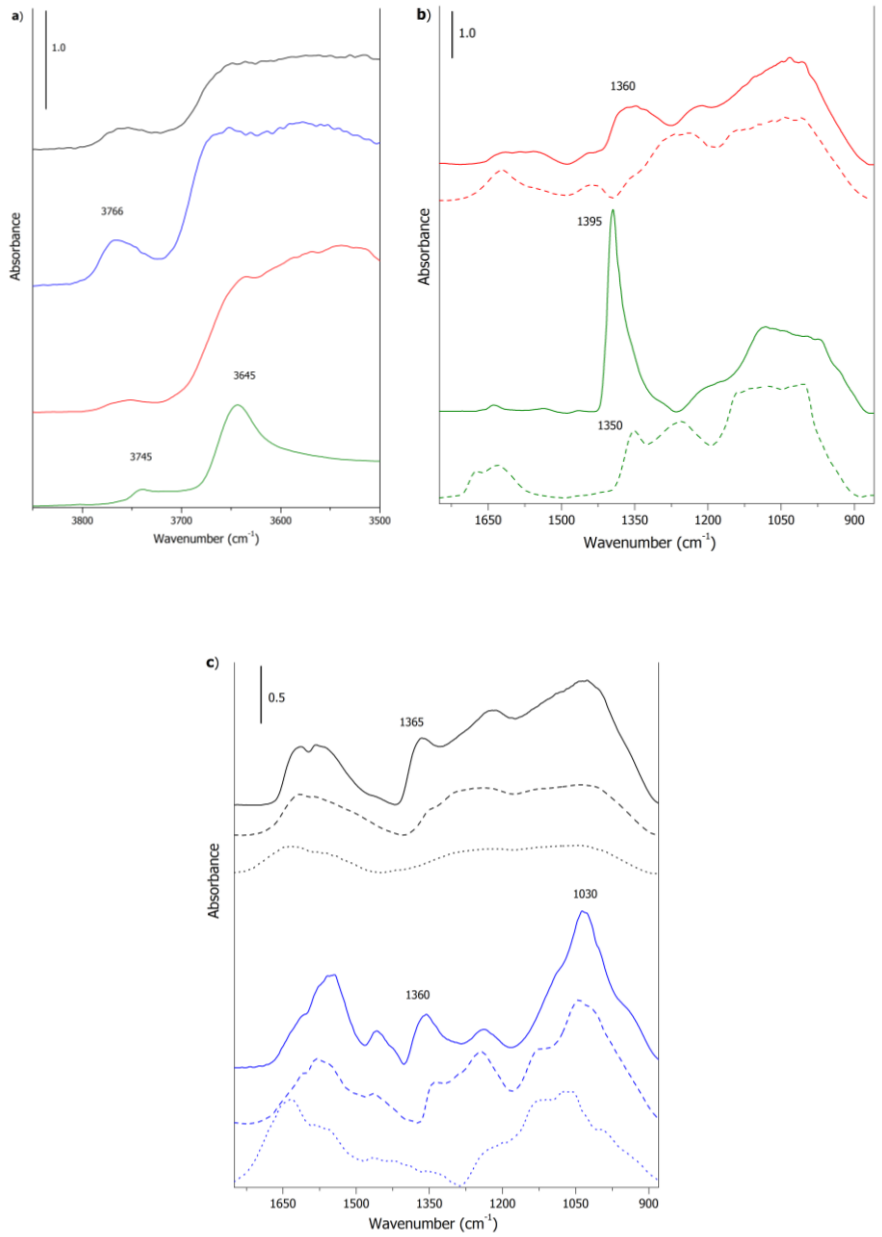

Figure 4.2. FTIR spectra of SZ_prec (in green), S2Z_8 (in red) S2Z_WI (in blue) and S1Z_5 (in black), recorder at ambient condition (dot line) in vacuum (dash line) and after activation at 573 K (solid line); in the νOH spectral region (a), in the 1700-880 cm^{-1} spectral region (b and c).

Spectra of S1Z_5 in different degrees of dehydration (black lines in Figure 4.2b) are very similar, exhibiting a broad band in the 1400-900 cm^{-1} range, which becomes only partially structured after thermal activation (see the black solid-line in Figure 4.2b). The presence of at least a fraction of covalent surface sulfates is supported by the spectral pair at 1365 and 1030 cm^{-1}, but the relatively high intensity of the band at 1220 cm^{-1} could suggest that a large part of sulfates still retains a more ionic configuration.

On the basis of these spectral features, the amount of surface sulfates with covalent configuration is suggested to follow this order: SZ_prec > S2Z_WI > S2Z_8 > S1Z_5. As already suggested by the literature, the nature of surface sulfate is strongly affect by both preparation and calcination methods.[14,15] If compared to SZ calcinated in a conventional way, samples calcined by the MW-assisted procedure present sulfates with a less covalent character. Comparing the impregnation methods each other, the covalent character of surface sulfates is more pronounced in the sample prepared by the wetness impregnation, S2Z_WI, that has a low amount of SO_4^{2-} groups. Samples impregnated with larger amount of sulfating agent by incipient wetness impregnation seems to present a major fraction of sulfates with ionic configuration.

In order to understand how the nature of surface sulfates affects the acid properties of these catalysts, the presence and strength of Lewis and Brønsted acid sites was investigated by means of FTIR spectroscopy of adsorbed probe molecules. The RT adsorption of CO has proven to be a very convenient tool to evaluate the acidic strength of strong Lewis sites at the surface of non-d (d^0) metal oxides. The strength of the acid-base interaction, and thus the Lewis acidity of the surface acid sites, has been found to be correlated to the upwards shift of the CO stretching mode with respect to the frequency of the free gaseous molecule (~2143 cm^{-1}).[16,17,18]

Adsorption of 2,6-dimethylpyridine (2,6-DMP) permits to easily identify both Brønsted and Lewis sites, forming two typical groups of bands.[20,21,22]

For plain and sulfatedt-ZrO_2, the RT adsorption of CO has been shown previously to yield a strong signal in the 2200-2180 cm^{-1} spectral range, related to coordinatively unsaturated surface (cus) Zr^{4+} cations located in crystallographic defective positions.[16,19] Upon sulfation, the CO frequency increases, as it is expected to occur in the presence of electron withdrawing groups, such as surface sulfates, and can be related to an increase of the Lewis-acid of the Zr^{4+}cus cations. In the case of pure tetragonal zirconia obtained by MW-assisted method, CO adsorption gives rise to a strong signal at 2181 cm^{-1}, whose frequency increases as CO coverage decreases (see Figure 3.15a). In addition, at 100 torr, a well recognizable shoulder at 2155 cm^{-1} is present, which decreases rapidly in intensity by evacuation. It has been proposed that the CO signal can be resolved into two peculiar components: $(CO)_a$ at higher wavenumbers, yet saturated at low coverage, and $(CO)_b$ at low wavenumbers, exhibiting a lower intensity.[12] The former component is attributable to CO adsorbed on the most acid Lewis sites, i.e, cationic sites located on crystallographic defective configuration; besides, the latter component has been assigned to CO uptake onto cus cationic sites on extended patches of regular crystal planes. The shoulder at 2155 cm^{-1} could be then assigned to the $(CO)_b$ component. Upon CO adsorption on the 'model' sulfated sample (SZ_prec) a strong and sharp signal is observable at 2199 cm^{-1}, which decreases in intensity with decreasing coverage, as shown in Figure 4.3a, suggesting the presence of strong Lewis sites. In the sulfated sample obtained by MW-assisted method the related signal can be observed at lower wavenumbers, and so Lewis strength is supposed to decrease as follow: SZ_prec > S2Z_8 > S1Z_5 > S2Z_WI. Signal intensity of SZ sample is slightly lower compared to pristine zirconia, suggesting that surface sulfates reduces only partially the amount of Lewis-

acid sites, and increases only to a very limited extent their acid strength. For all MW-synthesized samples it is possible to observe a shoulder at 2155 cm^{-1}, already observed in pure zirconia, and probably related to CO absorption on regular planes. We may suppose that this feature could be related to MW-calcination, being this spectral feature absent only in SZ_prec. MW-assisted calcination seems to generate heterogeneous surface sulfates that occupy both defective and regular sites, while on 'model' systems only the defective sites are set free and may interact with CO molecules.

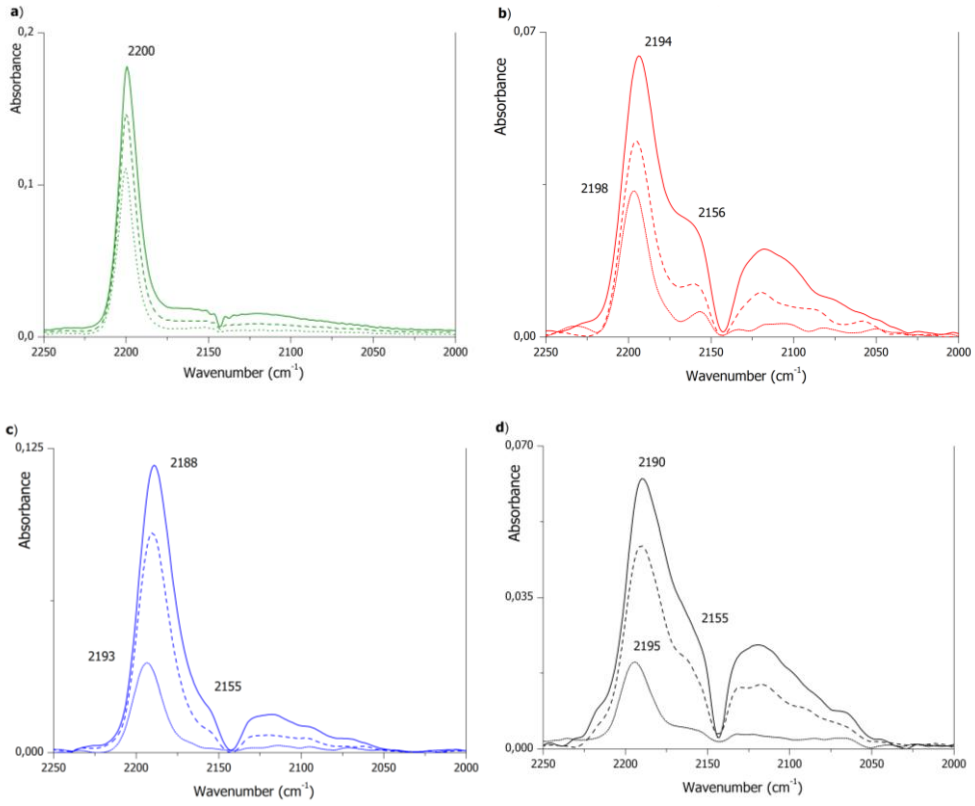

Figure 4.3. Differential FTIR spectra of CO adsorbed on (a) SZ_prec, (b) S2Z_8, (c) S2Z_WI and (d) S1Z_5. Solid line for 100 torr, dash line for 50 torr, dot line for 5 torr.

Many studies have confirmed that 2,6-DMP uptake can reveal the presence of acidic sites that differ either in nature (i.e., Lewis or Brønsted) or in acidic strength.[20,21,22] On plain zirconia only the presence of Lewis acid sites is revealed, but different sites could be distinguished, characterized by different reversibility to evacuation. On SZ systems, surface 2,6-DMPH$^+$ species are easily recognizable by IR and are strongly held to the surface, indicating the presence of medium-strength Brønsted acid sites resulting from sulfation.[23]

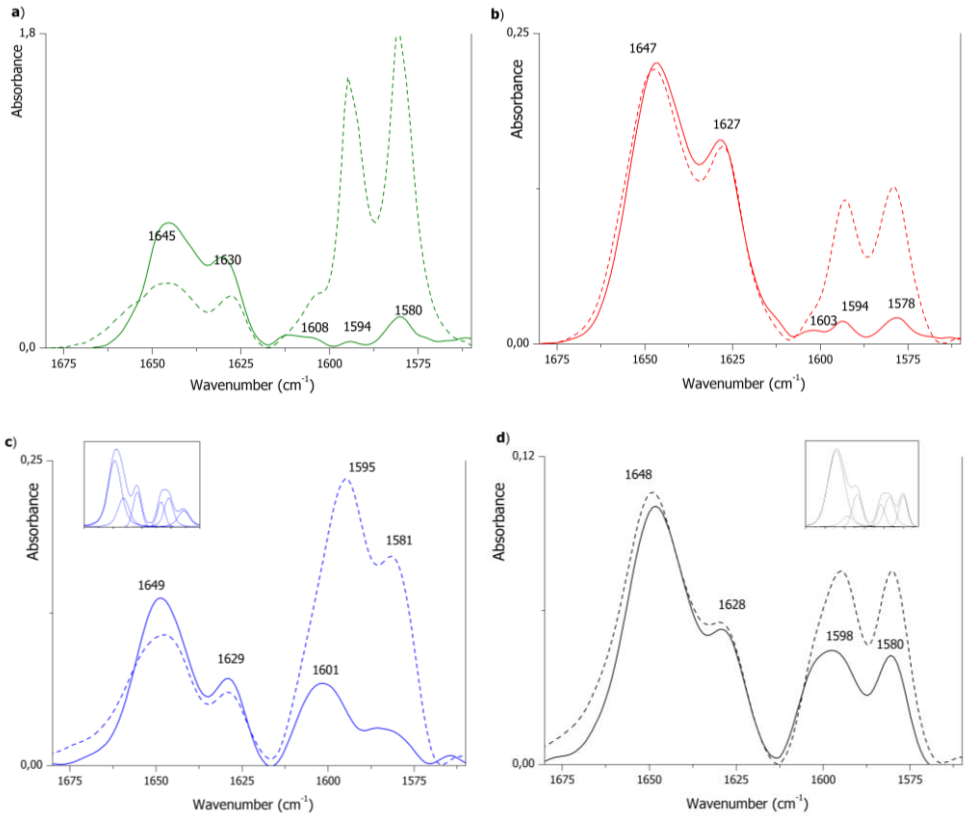

Figure 4.4. Differential FTIR spectra of 2,6-DMP adsorbed on (a) SZ_prec, (b) S2Z_8, (c) S2Z_WI, (d) S1Z_5. Dash line under maximum pressure, solid line after evacuation for 15 min.

2,6-DMP adsorption on SZ_prec (in Figure 4.4a) gives rise to spectra similar to those reported for similar tetragonal sulfated zirconia.[23] At the

maximum pressure (~4 torr) the strongest signals are represented by the two bands at 1594 and 1580 cm^{-1} (ascribable to H-bonded and physisorbed 2,6-DMP molecules), with a shoulder at 1604 cm^{-1}, due to Lewis-coordinated 2,6-DMP, and a broad envelope above 1620 cm^{-1}, due to 2,6-dimethylpyridinium, is present. Upon outgassing, the overall intensity of the envelope at lower wavenumbers decreases drastically, as expected for the elimination of physisorbed/weakly held species, but bands at 1580, 1594, 1608 cm^{-1} are still observable, suggesting the presence of strong Lewis acid centres. The spectral features of Brønsted-bound 2,6-DMP species are strong, with only a partial modification in intensity and profile as well. For S2Z_8 the adsorption of 2,6-DMP reveals the presence of both Lewis and Brønsted acidic sites, as shown in Figure 4.4b. We can notice that at the maximum pressure the strongest band is that related to 2,6-$DMPH^+$ modes, whose spectral profile remains virtually unchanged after outgassing. Signals related to the strongest Lewis acid sites, which retain 2,6-DMP at low pressure, are observable at 1578, 1594 and 1604 cm^{-1}, similar to those observed in the previous sample. On the contrary, both S2Z_WI and S1Z_5 show a different behaviour: these two samples present the two bands related to 2,6-dimethylpyridinium modes at 1648 and 1629 cm^{-1}, ascribable to Brønsted acidity. Below 1620 cm^{-1} a resistant fraction of physisorbed and/or H-bonded 2,6-DMP is evident and gives rise to a multiple band still intense after evacuation. Curve fitting (by means of the facility present in the OMNIC software) of this unresolved band (in the inset of Figure 4.c and Figure 4.d) suggests that it is composed by 3 distinct components, respectively located at ~ 1582, 1596 and 1604 cm^{-1}, analogous to those observed in previous samples. Shape and position of these spectral components are more similar to that reported for t-ZrO_2, than to other analysed SZ materials, suggesting that for S1Z_5 and S2Z_WI sulfation does not particularly affect the strength of the Lewis acidity, even if

Brønsted acid sites are present on the surface. On the basis the spectral features previously described, the proposed scale of the strength of Lewis acidity is analogous to that suggested by CO absorption and the same trend is also suggested for Brønsted acidity (SZ_prec > S2Z_8 > S2Z_WI > S1Z_5).

4.2 Catalytic tests

Acid hydrolysis of glucose was carried out at 180°C in solution with a low concentration (0.027 M) to minimize side reaction of products, as suggested by similar studies[1,2]. In fact the formation of humins is suggested to be strongly affected by the initial substrate concentration, being formed in a second order reaction.[24] In Table 4.1 results relative to tests carried out on samples prepared by MW-assisted procedure (S2Z_WI, S2Z_8, S1Z_5) and on the 'model' system, SZ_prec are reported and compared. FTIR analysis on the employed catalysts, described in the previous section, suggests that these materials possess surface sulfates with different nature, leading to surface acid sites of different strength. Results on adsorption/desorption of probe molecules suggest that SZ_prec and S2Z_8 present stronger Lewis and Brønsted surface sites if compared to S2Z_WI and S1Z_5.

Table 4.1. Results of catalytic tests for SZ.

Catalyst (Reaction time)	Conversion %	C balance %	Product Yield (Selectivity)%					
			% FA		% LA		% HMF	
S2Z_WI (1)	60.0	47.3	1.02	(1.70)	0.17	(0.28)	26.1	(43.4)
S2Z_WI (3)	76.0	47.7	6.74	(8.87)	0.17	(0.22)	28.0	(36.9)
SZ_prec (3)	88.9	28.9	4.09	(4.60)	3.43	(3.86)	17.0	(19.1)
S2Z_8 (3)	59.0	16.6	0.00	(0.00)	0.12	(0.21)	10.1	(17.1)
S2Z_WI (5)	78.0	49.3	1.71	(2.19)	0.18	(0.23)	34.9	(44.8)
S2Z_8 (5)	91.4	24.0	2.67	(2.92)	3.29	(3.60)	14.6	(15.9)
S1Z_5 (5)	91.3	7.71	0.24	(0.26)	0.12	(0.13)	6.45	(7.07)

Different reaction time (from 1 to 5 hours) were tested for S2Z_WI: a good yield of HMF (around 30%) was obtained, with an increase for longer reaction time. For S2Z_8 glucose conversion is significantly improved for longer reaction time, enhancing HMF production (~15%), and promoting the formation of small amounts of LA (~3%). Instead S1Z_5 shows poor selectivity, and only a small amount of HMF (6.5%) was observed even for longer reaction time. Even if glucose conversion is high, the carbon balance is very low suggesting that glucose hydrolysis generates condensation and degradation products, not easy to identify. Besides, the 'model' SZ_prec promotes the formation of HMF (17%) and LA (3.4%) after 3 hours, showing good rate of conversion and carbon balance.

According to the catalysts' surface properties previously described, we can rise some consideration on catalysts' activity and selectivity. SZ_prec possesses surface sulfate groups with a high covalent character, that generates strong Lewis and Brønsted sites. The latter are suggested to promote glucose isomerization, and the former to act on the following hydration/dehydration reactions. Also S2Z_8 presents medium-strong Lewis and Brønsted acid sites, which promote the formation of HMF and LA. Catalyst that is supposed to possess weaker Brønsted acid site, such as S2Z_WI, promotes the formation of HMF, but no further hydrolysis to LA. Fructose yield was found to be maximal when the reaction is stopped after 1 hour, suggesting that the reaction passes through glucose isomerization to produce good HMF yield, but long reaction time are required to improve conversion. On the contrary, S1Z_5 shows poor catalytic activity, even if Lewis and Brønsted sites have been recognized to be present on its surface. The presence of a stable Lewis or Brønsted acidity on SZ is a necessary but not sufficient condition to observe catalytic activity. Morterra et al.[23] have already evidenced this behaviour in SZ catalysts employed in the mild

temperature isomerization of n-butane, a standard reference reaction to test the catalytic activity of SZ-based materials.

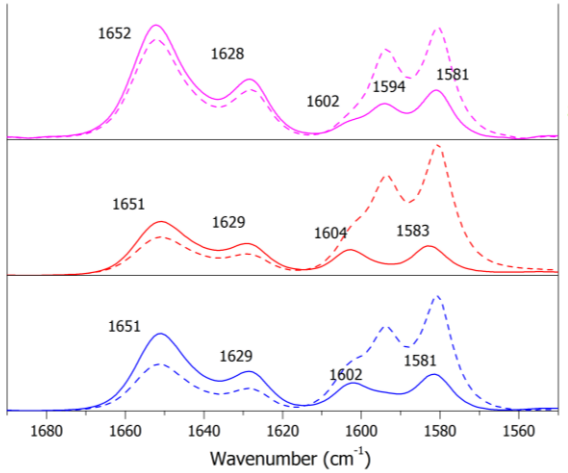

Figure 4.5. Differential FTIR spectra of 2,6-DMP adsorbed on SBA-SO_3H obtained using hexane (in blue), toluene (in red) or saline solution (in pink) as grafting solvent (dash line under maximum pressure, solid line after evacuation for 15 min at RT).

Recently Pizzolitto et al.[25] reported that a good yield of LA (more than 10%) could been obtained using sulfonated SBA-15 (SBA-SO_3H) as catalyst. In this research the role of different grafting solvents (toluene, hexane, and saline solution), used for post-synthesis modification with 3-mercaptopropyltrimethoxysilane, on catalysts' activity was investigated. The most active catalyst is resulted to be that obtained using saline solution. Sulfonated materials have shown to present strong Lewis and Brønsted acid sites, as evidenced by FTIR investigations (2,6-DMP ads/des), whose results are summiresed in Figure 4.5. After adsorption of a large dose of base (dash line), it is possible to observe the typical two signals pattern ascribable to 2,6-dimethylpyridinium ions generated by interaction with Brønsted sites, at 1628 and 1652 cm^{-1}, and a intense band due to phisosorbed/H-bounded 2,6-DMP.[26] After outgassing, above 1620 cm^{-1} the spectral profile remains virtually unchanged, whereas net signals remain at

lower wavenumbers, respectivelyat 1602 and 1583 cm^{-1} and ascribable to 2,6-DMP molecules coordinatedto Lewis acid sites of medium-high strength, more strongly held at the surface.[20] Results suggest that Brønsted acidity seems to be more pronounced in samples obtained employing saline solution, and this catalyst produces the highest yield of LA.

In Figure 4.6 we compared results obtained for glucose conversion catalyzed by SZ obtained by MW-assisted sinthesis and SBA-15 materials, after 5 hours at 180°C. We can observe a major glucose conversion for SZ materials, probably related to the higher thermal stability of zirconia with respect to the siliceous materials. Sulfonated SBA-based catalysts promote HMF and LA formation, while SZ exhibits a good selectivity to HMF.

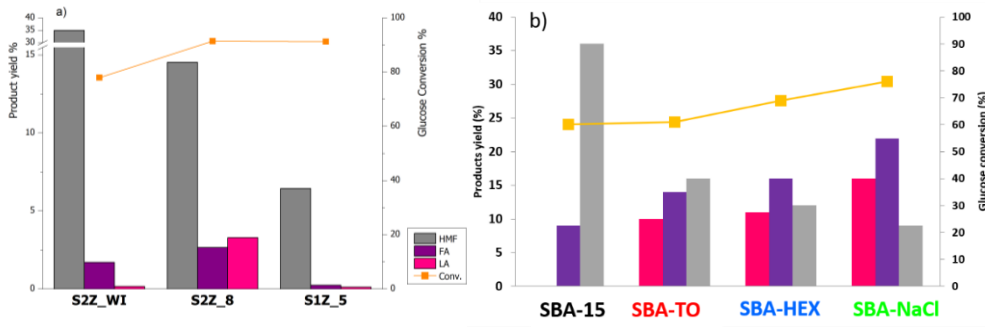

Figure 4.6. Products yields and glucose conversion after 5 hours of reaction at 180°C for: (a) SZ catalysts obtained by MW-assisted synthesis (b) SBA-15 and SBA-SO_3H catalysts (from Ref. 25).

All catalysts (with the exception of S1Z_5) present Lewis and Brønsted acid sites of medium-high strenght that promote glucose hydrolysis according to the pathway proposed in Scheme 4.1. Selectivity in this reaction seems to be influenced by both strength and number of Lewis and Brønsted acid sites, thus the ratio between Lewis and Brønsted acidic sites (L/B) could play a key role. The estimation of L/B ratio requires the

knowledge of molar absorption coefficients (ε) values, specific for each vibrational mode considered and influenced by the surface.

4.3 Quantitative determination of surface acidity (Lewis/Brønsted ratio)

Quantitative measurements and interpretations from infrared spectra require the knowledge of the molar absorption coefficient(s) (ε) of a relevant species. Molar absorption coefficients can be determined assuming that the system (absorbent and substrate) conforms to Beer-Lambert type behaviour. Determination of the absorption coefficient for a particular mode require the measurement of both the integrated band area and the number of moles adsorbed on that particular species. Volumetric gas dosing or gravimetric measurements using a microbalance into an infrared cell allows to measure the number of moles adsorbed simultaneously with recording the spectrum in situ.[27,28] More recently it has been develop a new method that combines IR and gravimetric analysis (AGIR) by using specifically designed cells which allows the simultaneous measurement of both uptake and FTIR spectrum.[29] Several values of integrated molar absorption coefficients for 2,6-DMP can be found in the literature, regarding H-bonded, protonated and coordinated 2,6-DMP for similar systems. In Table 4.2 a series of these values has been reported and a large variation among them is evident.[21,34] For pyridine, another commonly used base probe molecule, molar absorption coefficients of pyridine modes have been reported to vary as a function of acid sites density that in turn is dependent on sulfates concentration.[30,31,32] But a similar behaviour is observed also for phosphated zirconia. The correlation, or lack of, between molar absorption coefficients of phosphated (ε_L=1.02–1.07 cm·μmol^{-1}, ε_B=0.50–0.76 cm·μmol^{-1}) and phosphate free (ε_L=1.78 cm·μmol^{-1}, ε_B=0.53 cm·μmol^{-1}) samples indicated

that the Lewis acid site environment was modified by phosphate addition, whereas the Brønsted sites remained relatively unchanged.[33] It can be supposed that also molar absorption coefficient of Lewis and Brønsted modes of 2,6-DMP vary in function of acid sites density, and so the use of literature values can lead to errors. We have determined the values of integrated molar absorption coefficients for SZ and SBA-SO_3H by volumetric method, using the procedure described in chapter 2.[21,27,28]

Table 4.2. Absorption coefficients for adsorbed 2,6-DMP on acidic sites.

Metal Oxide	Lewis / H-bond modes		Brønsted modes		Ref.
	Wavenumber (cm^{-1})	Coefficient (cm μmol^{-1})	Wavenumber (cm^{-1})	Coefficient (cm μmol^{-1})	
Silica-Alumina	1617	1.01–1.16	1650	3.70–4.06	[34]
SiO_2	1606 1585	1.9 1.9	--	--	21
Phosphated SiO_2			1655 + 1630	7.9	21
H-Y Zeolite			1652 + 1627	6.5	21
Alumina	1617	5.3	--	--	21
SBA-SO_3H	1604 + 1583	3.9	1652 + 1628	5.2	This work
ZrO_2	1609	3.4	--	--	21
WO_x/ZrO_2			1643 + 1628	5.9	21
NbO_x/ZrO_2			1644 + 1628	7.3	21
SO_4-ZrO_2	1579 + 1594 + 1604	1.1	1646 + 1630	5.8	This work

Figure 4.7a reports the infrared spectra in the 1675-1565 cm^{-1} range for increasing doses of 2,6-DMP (from 0.068 to 3.8 μmol) adsorbed on SBA-SO_3H. The spectra exhibit the ν_{8a} and ν_{8b} bands, respectively, at 1652 and 1630 cm^{-1}, characteristic of 2,6-DMP protonated species, and at 1604 and 1583 cm^{-1}, attributed to 2,6-DMP adsorbed on the surface by H-bonding, as already discussed previously. Curve-fitting results (in Figure S9b) suggest the presence of a third component (at 1640 cm^{-1}) in the band associated to protonated species, whose intensity increases similarly to the more evident components. A linear variation of the intensity of Lewis and Brønsted integrated areas is observed as a function of the added 2,6-DMP amount, as

evident is Figure 4.7b. For oxidic systems presenting different types of bonds between 2,6-DMP and their surfaces, integrated molar absorption coefficients were obtained from eq. 1, derived from Beer-Lambert law. Solving the resulting set of equations, molar coefficients of Lewis and Brønsted bands resulted respectively 3.9 cm·μmol^{-1} and 5.2 cm·μmol^{-1}.

$$\frac{S}{n}\left(\frac{A_L}{\varepsilon_L}+\frac{A_B}{\varepsilon_B}\right)=1 \qquad (1)$$

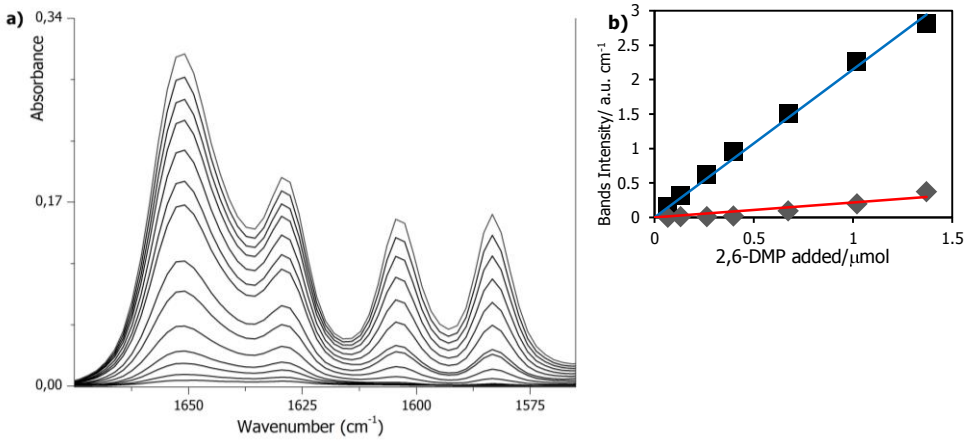

Figure 4.7. SBA-SO_3H: (a) Infrared spectra for increasing amounts of 2,6-DMP (from 0.068 to 1.4μmol); (b) evolution of the bands area of Lewis bands (red line) and of Brønsted bands (blue line) with the amount of added 2,6-DMP.

The obtained values are slightly different if compared to those reported in the literature, for which a large variation is generally reported (Table 4.2). The calculated ε_B is slight smaller than that reported for phosphated silica (7,9 cm·μmol^{-1}), but comparable to zeolite or silica-alumina values; on the contrary, ε_L is bigger than those reported for pristine silica (1.9 cm·μmol^{-1}). These results suggest that integral molar absorption coefficients can considerably vary when more than one types of bonds between 2,6-DMP and the surface can occur. All the reported systems possess strong sites of a unique nature, but SBA-SO_3H presents both Lewis and Brønsted

sites with medium strength. This affects both location and bonding type of adsorbed molecules and consequently the values of their molar absorption coefficients.

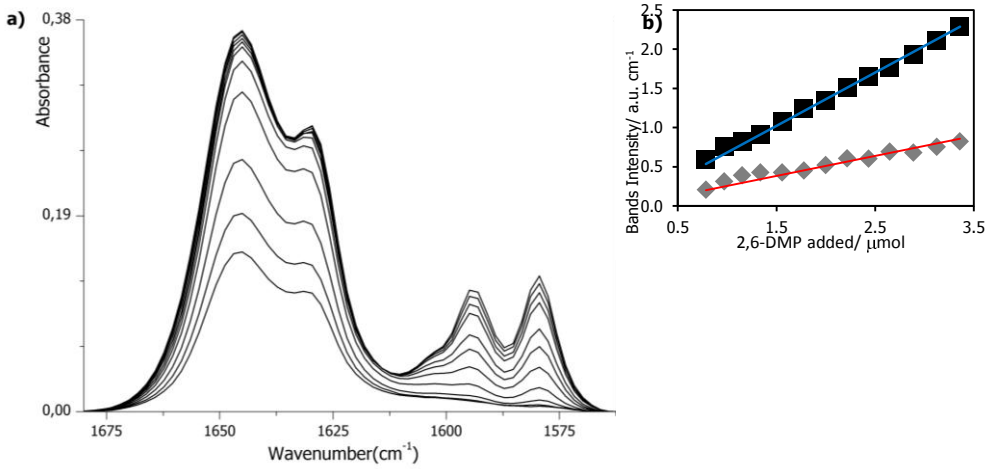

Figure 4.8. SZ: (a) Infrared spectra for increasing amounts of 2,6-DMP (from 0.78 to 3.4 μmol); (b) evolution of the bands area of Lewis bands (red line) and of Brønsted bands (in blue) with the amount of added 2,6-DMP.

Figure 4.8a shows the infrared spectra between 1630 and 1550 cm^{-1} for increasing doses of 2,6-DMP adsorbed on SZ. The spectra exhibit bands characteristic of protonated species, at 1646 and 1629 cm^{-1}, and bands ascribable to 2,6-DMP adsorbed on the surface by Lewis/H-bond interactions at 1604, 1594 and 1583 cm^{-1}. Also in this case, curve-fitting results (in Figure S9a) suggest the presence of a third component (at 1637 cm^{-1}) in the envelope associated to the protonated species, whose intensity increase slower than the more evident components. The system containing different types of bonds between 2,6-DMP and the surface and eq. 1 were used and, by solving the resulting set of equations, molar coefficients of Lewis and Brønsted bands have been obtained, being respectively 1.1 $cm \cdot \mu mol^{-1}$ and 5.8 $cm \cdot \mu mol^{-1}$. It has been reported that, for adsorption experiments on SZ systems carried out by adding small increasing doses,

2,6-DMP uptake starts first at protonic acidic sites and is over 50% complete before the onset of uptake at Lewis sites.[23] A similar behaviour was observed for our system, and so values are obtained from higher amount of added base molecules. Obtained values are slightly different if compared to those reported in the literature (Table 4.2), being ε_L bigger that those reported for pristine zirconia (3.4 $cm \cdot \mu mol^{-1}$) and ε_B smaller than that reported for zirconia supported W/Nb oxide (respectively 5.9 $cm \cdot \mu mol^{-1}$ and 7.3 $cm \cdot \mu mol^{-1}$). As previously suggested, the presence of both Lewis and Brønsted sites could affect the location and bonding type of absorbed molecules and, consequently, the values of molar absorption coefficients.

To verify if the experimental calculated ε_L and ε_B values give a good estimation, a cross-check was done calculating the total number of adsorbed 2,6-DMP molecules, comparing then the results with experimental values. For SBA-SO_3H and SZ percent errors are very low (<1%) at high amount of adsorbed molecules, but become more relevant for smaller doses, especially in the case of SZ, for which the interaction of 2,6-DMP with Brønsted and Lewis sites is suggested to occur not simultaneously. A different approach to calculate integral molar coefficient consists in subtracting the contribution due to H-bond or Lewis sites components, using the values determined with other solids in order to calculate the amount of 2,6-$DMPH^+$, and then ε_B was calculated directly using the slope of the linear part of the curves ($A_B = (\varepsilon_B \cdot n_B)\ S$). For SBA-$SO_3$H, using ε_L=1.9 $cm \cdot \mu mol^{-1}$ of pristine silica, the value of ε_B resulted to be 5.5 $cm \cdot \mu mol^{-1}$, but the corresponding calculated numbers of adsorbed 2,6-DMP molecules resulted overestimated at high doses of 2,6-DMP (average error 23%). Similarly, calculation was done for SZ, using ε_L=3.4 $cm \cdot \mu mol^{-1}$ obtained for pure zirconia, but we obtained a $\varepsilon_B < \varepsilon_L$, that has to be considered meaningless. These results support the previous hypothesis that integral molar coefficients of sulfated oxides presenting both Lewis and

Brønsted acid sites could be very different from those obtained for the corresponding pure metal oxides.

The concentration of Lewis and Brønsted acid sites on the catalyst described in the previous section was quantified using the calculated molar extinction coefficients (Table 4.3). As evident, the concentration of Lewis and Brønsted sites is very different among the various SZ systems. Equal nominal % wt amount of sulfates were impregnated on SZ_prec and S2Z_8, but the amount of Brønsted sites is lower. MW-synthesized SZ, S1Z_5 and S2Z_WI, impregnated with smaller sulfates amount exhibit a very low Brønsted concentration. Results suggest that MW-assisted calcination seems not to be the best option to obtain surface sulfates sites able to enhance Brønsted acidity and then the catalytic activity thereby.

Table 4.3. Acid sites concentration and L/B ratio.

Catalyst	N Lewis (mmol g^{-1})	N Brønsted (mmol g^{-1})	A_L/A_B
SZ_prec	0.21	0.32	0.7
S2Z_8	0.052	0.12	0.4
S2Z_WI	0.21	0.081	2.7
S1Z_5	0.16	0.068	2.4
SBA	0.60	--	--
SBA-SO_3H (NaCl)	0.43	0.66	0.7
SBA-SO_3H (Hex)	0.31	0.48	0.7
SBA-SO_3H (Tol)	0.22	0.34	0.6

However, some correlations between catalytic activity and L/B ratio can be done. All catalysts that promote LA formation possess L/B values lower than 1, confirming that Brønsted acidity is a necessary condition. On the contrary, to obtain 5-HMF Lewis acidity seems to be sufficient. Similar yields (around 35%) were obtained using SBA, a system presenting only Lewis acidity, and S2Z_WI, a system having a pronounced Lewis character. S1Z_5, even showing some acidity, has poor catalytic activity. This confirms that the presence of surface acid sites is a necessary but not a sufficient parameter to evaluate the catalytic activity. These results suggest that

contrary to what reported, the formation of HMF is observed even when Brønsted acidity is absent. It has been proposed that glucose can directly transform into HMF, without passing thought fructose isomerization.[35,36] In addition, glucose and/or fructose can be converted to multiple other products, with more than one reaction pathway taking place simultaneously.[37] For example humins can be formed from degradation and condensation of glucose and many other intermediates. But also retro-aldol reactions, that lead to the formation of short carboxylic acids, as shown in Scheme 4.2, can occur.

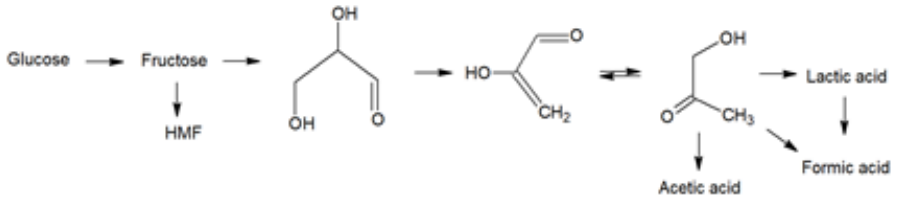

Scheme 4.2. Possible pathway of fructose degradation.

4.4 Thermal studies by ATR

Understanding the mechanism of catalytic reactions is of particular importance in order to design functional catalysts. We made a preliminary study to understand if it is possible to investigate the possible mechanisms by ATR spectroscopy. We monitored heating of pure glucose and of glucose+catalyst mixtures (from ambient T to 180°C) recording time-resolved spectra by ATR. Raman and IR have been successfully applied to identify and quantify glucose in blood and food. Specific signals (1123 and 1033 cm^{-1} in Raman and IR spectra, respectively) are commonly used as marker bands for glucose. Another series of band allow the identification of α and β anomers, because the OH moiety directed either below or above

the ring plane, respectively, exhibits different features in the relevant vibrational spectra.[38]

ATR spectrum of hydrated glucose is extremely rich in bands, see Figure 4.9. The most intense signals are located in the 1150-950 cm^{-1} spectral range, and are ascribable to C–C and C–O stretching and bending modes. At higher wavenumbers signals related to stretching mode of CH groups are well structured and recognizable singled out at 2944, 2912, 2891 and 2880 cm^{-1}, while hydroxyl groups give rise to a broad band. ATR spectra at increasing temperature are shown in Figure 4.9 and as consecutive spectra in Figure S10–S12. No relevant spectral changes are observed increasing T up to 150°C: the spectral components generally shift to lower wavenumbers and broaden, in particular in the ν_{OH} region.

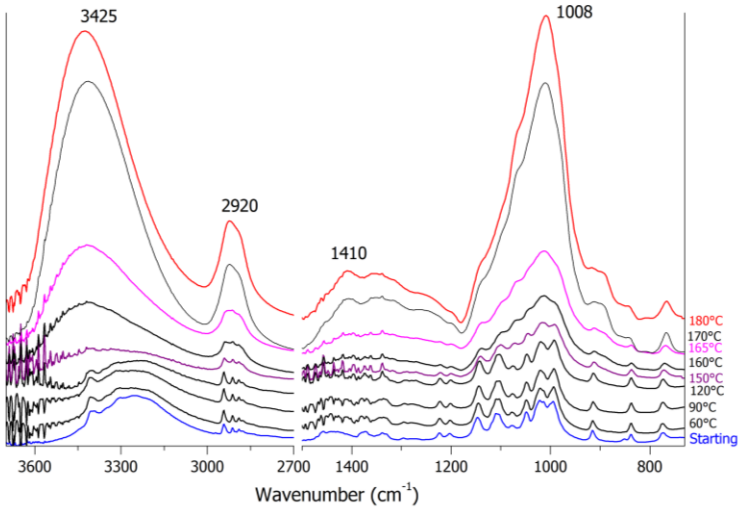

Figure 4.9. ATR spectra of glucose at increasing temperature (from 27°C to 180°C).

Glucose melts at ~148°C (depending on its isomeric form) and, starting from this temperature on, signals start to increase in intensity and to broaden, being this behaviour more pronounced between 160°C and 170°C. At the final T (180°C) signals attributable to C–C and C–O give an intense

and broad band with a maximum at 1008 cm^{-1}, and individual signals of CH stretching modes generate a broad and intense band. New broad signals appear in the 1200-1500 cm^{-1} spectral range and above 3000 cm^{-1}. It is well known that the thermal decomposition of sugars leads to the formation of both brown-coloured compounds (that gives caramel colour) and volatile products, with the typical caramel aroma. Caramelization consists in a complex series of reactions due to decomposition under relatively dry conditions: in the case of glucose the process takes place at 160°C.[39] The reaction pathway starts with an enolization, in which glucose gives rise to 1,2-enediol, an important intermediate in the formation of a large number of furan and pyran compounds.[40] The formation of these types of compounds perfectly matches with the new signals observed and previously ascribed to C–C, C–O and O–H stretching and bending modes, but due to the similarity among the several products, it is not possible to individually single out them.

We prepared a semi-solid mixture composed by the catalyst and the glucose solution (glu+SZ mixture), which has been then heated from ambient temperature to 180°C. Glu+SZ mixture exhibits a spectrum dominated by signals related to glucose and, subtracting the net SZ contribution, gives a spectrum similar to those recorded for the plain glucose solution, as evident in Figure 4.10b. ATR spectra recorded at increasing temperatures are shown in Figure 4. 10a and as consecutive spectra in Figure S13-S14. Differently to those observed for pure glucose, the spectral profile starts to change around 70°C for the glu+SZ mixture, when water removal allows to recognize CH stretching signal at 2915 cm^{-1}. The band in the 1150-950 cm^{-1} starts to broaden with a parallel blue-shift of 16 cm^{-1}, whereas the band originally ascribable to CH bending modes (1201 and 1225 cm^{-1}) has a similar shift towards higher wavenumbers. Band ascribable to hydroxyl stretching mode continues to decrease until the

maximum temperature is reached. With increasing temperature, it is possible to observe the formation of a signal located at 1425 cm^{-1}, that gradually decreases at T ≥ 100°C until it vanishes. We can suppose that this signal is related to a peculiar intermediate, that is forming and consuming during heating. Infrared spectrum of fructose[38] exhibits a weak signal around 1425 cm^{-1}, but the absence of other related strong signals in our spectra is inconsistent for its identification. HMF presents strong infrared signals around 1400 and at 1022 cm^{-1}.[41] Both are detectable in our spectra, exhibiting similar pattern in intensity as well, suggesting that HMF is formed and degraded during heating.

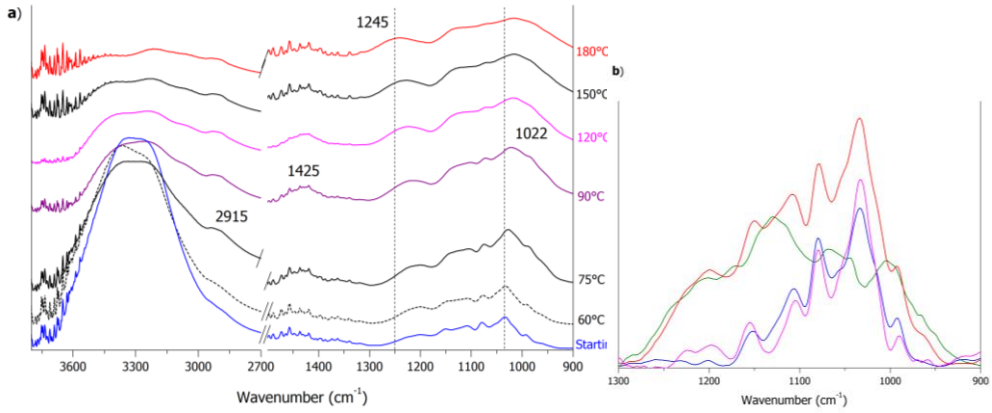

Figure 4.10. (a) ATR spectra of mixture glu+SZ at increasing temperature (from 27°C to 180°C); (b) ATR spectra of glucose solution (in blue), SZ (in green) and mixture glu+SZ (in red), in pink differential spectra (mixture - SZ).

We prepared a semi-solid mixture composed by SBA-SO_3H and glucose solution (glu+SBA mixture) which has been heated up to 180°C. The ATR spectrum of the glu+SBA mixture is mainly attributable to the characteristic catalyst peak around 1050 cm^{-1}, and only subtracting the SBA contribution, glucose characteristic signals are identifiable, as shown in Figure 4.11b. ATR spectra obtained at increasing temperature are shown in Figure 4.11a and as consecutive spectra in Figure S15-S16. In the glu+SBA mixture the spectral profile starts to change around T = 60°C, when the weak signals

related to glucose start to decrease and vanish at ~70°C. Then spectra remain virtually unchanged, in particular the typical peak of SBA located at 1058 cm^{-1}. Only a weak and broad signal can still be observed at ca 800 cm^{-1}.

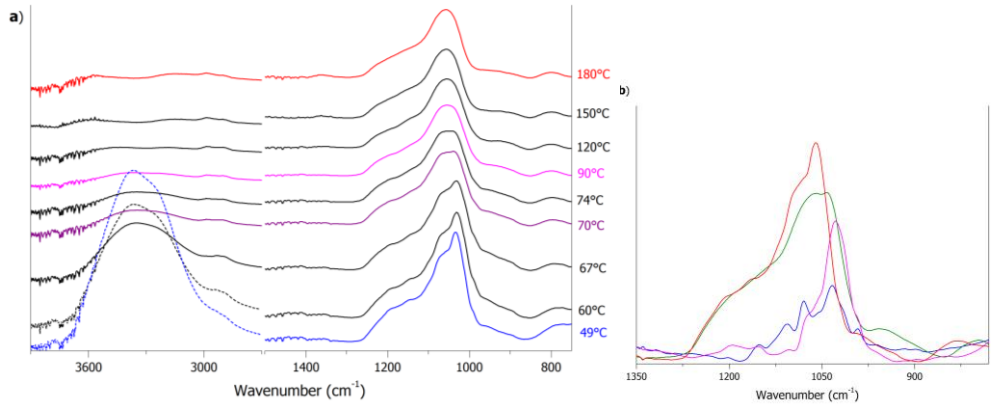

Figure 4.11. (a) ATR spectra of mixture SBA-SO_3H and glucose solution at increasing temperature (from 49°C to 180°C); (b) ATR spectra of glucose solution (in blue), of SBA-SO_3H (in green) and of their mixture (in red), in pink differential spectra (Mixture - SBA-SO_3H).

This ATR preliminary study suggests that, even in the presence of small amount of water, materials act as catalyst by inhibiting the caramelization process observed for pure glucose, and thus promoting glucose conversion at lower T. Mechanism seems to follow different pathways using two different solid acid catalysts, even if both catalyst possess similar Lewis-Brønsted acid sites. A better investigation on the role of surface sites was attempted by using FTIR spectroscopy. A pellet composed by a mixture of glucose and catalyst (1:4 in wt) has been heated at 180°C adding small doses of water in a controlled atmosphere. Unfortunately, this approach resulted not properly informative. In particular, (i) there is problem in the recognition of glucose signals: in the case of SZ it is possible to single out only 3 signals (namely, at 915, 852 and 837 cm^{-1}), which on the contrary are completely covered in SBA materials. (ii) Even if heating is performed

adding water, pellets rapidly became brown giving rise to noisy spectra. (iii) The identification of gaseous products is complicated by water signals that completely cover the most relevant bands.

---

[1] S. Kang, J. Fu, G. Zhang, From lignocellulosic biomass to levulinic acid: A review on acid-catalyzed hydrolysis, *Renew. Sust. Energ. Rev.* **2018** (94), 340–362.

[2] A. Osatiashtiani, A.F. Lee, D.R. Brown, J.A. Melero, G. Moralese, K. Wilson, Bifunctional SO_4/ZrO_2 catalysts for 5-hydroxymethylfufural (5-HMF) production from glucose, *Catal. Sci. Technol.* **2014** (4), 333–342.

[3] X. Qi, M. Watanabe, T.M. Aida, R.L. Smith, Sulfated zirconia as a solid acid catalyst for the dehydration of fructose to 5-hydroxymethylfurfural, *Catal. Commun.* **2009** (10), 1771–1775.

[4] M. Hino, K. Arata, Synthesis of Solid Superacid Catalyst with Acid Strength of $H_0 \leq 16.04$, *J.C.S. Chem. Comm.* **1980**, 851–852.

[5] G.D. Yadav, J.J. Nair, Sulfated zirconia and its modified versions as promising catalysts for industrial processes, *Micropor. Mesopor. Mat.* **1999** (33) 1–48.

[6] X. Song, A. Sayari, Sulfated Zirconia-Based Strong Solid-Acid Catalysts: Recent Progress, *Catal. Rev.* **1996** (38, 3), 329–412.

[7] C. Sarzanini, G. Sacchero, F. Pinna, M. Signoretto, G. Cerrato, C. Morterra, Amount and Nature of Sulfates at the Surface of Sulfate-doped Zirconia Catalysts, *J. Mater. Chem.* **1995** (5, 2), 353–360.

[8] C. Morterra, G. Cerrato, F. Pinna, M. Signoretto, G. Strukul, On the Acid-Catalyzed Isomerization of Light Paraffins over a ZrO_2/SO_4 System: The Effect of Hydration, *J. Catal.* **1994** (149), 181–188.

[9] K. Nakamoto, *Infrared and Raman Spectra of Inorganic and Coordination Compounds*, 6th Edition, John Wiley & Sons, Inc., Hoboken, New Jersey, 2009.

[10] A.A. Tsyganenko, V.N. Filimonov, Infrared spectra of surface hydroxyl groups and crystalline structure of oxides, *J. Mol. Struct.* **1973** (19), 579–589.

[11] C. Morterra, G. Cerrato, G. Meligrana, M. Signoretto, F. Pinna, G. Strukul, Catalytic activity and some related spectral features of yttria-stabilised cubic sulfated zirconia, *Catal. Lett.* **2001** (73), 113–119.

[12] C. Morterra, G. Cerrato, L. Ferroni, Surface Characterization of Yttria-stabilized Tetragonal ZrO_2 Part 3-CO_2 Adsorption and the CO_2-CO Interaction, *J. Chem. Soc. Faraday Trans.* **1995** (91, 1), 125–132.

[13] S. Detoni, D. Hadzi, Infrared spectra of some organic sulphur-oxygen compounds, *Spectrochim. Acta* **1957** (11), 601–608.

[14] C. Morterra, G. Cerrato, M. Signoretto, On the role of the calcination step in the preparation of active (superacid) sulfated zirconia catalysts, *Catal. Lett.* **1996** (41), 101–109.

[15] G.X. Yan, A. Wang, I.E. Wachs, J. Baltrusaitis, Critical review on the active site structure of sulfated zirconia catalysts and prospects in fuel production, *Appl. Catal. A* **2019** (572), 210–225.

[16] C. Morterra, G. Cerrato, V. Bolis, C. Lamberti, L. Ferroni, L. Montanaro, Surface Characterization of Yttria-stabilized Tetragonal ZrO_2 Part 2-Adsorption of CO, *J. Chem. Soc., Faraday Trans.* **1995** (91, 1), 113–123.

[17] V. Bolis, B. Fubini, E. Garrone, C. Morterra, Thermodynamic and Vibrational Characterization of CO Adsorption on variously Pretreated Anatase, *J. Chem. Soc., Faraday Trans.*, **1989** (85), 1383–1395.

[18] C. Morterra, G. Cerrato, L. Ferroni, A. Negro, L. Montanaro, Surface characterization of tetragonal ZrO_2, *Appl. Surf. Sci.* **1993** (65/66), 257–264.

[19] C. Morterra, G. Cerrato, V. Bolis, S. Di Ciero, M. Signoretto, On the strength of Lewis- and Brønsted-acid sites at the surface of sulfated zirconia catalysts, *J. Chem. Soc., Faraday Trans.* **1997** (93, 6), 1179–1184.

[20] C. Morterra, G. Cerrato, G. Meligrana, Revisiting the Use of 2,6-Dimethylpyridine Adsorption as a Probe for the Acidic Properties of Metal Oxides, *Langmuir* **2001** (17), 7053–7060.

[21] T. Onfroy, G. Clet, M. Houalla, Quantitative IR characterization of the acidity of various oxide catalysts, *Micropor. Mesopor. Mat*. **2005** (82), 99–104.

[22] A.J. McCue, G.A. Mutch, A.I. McNab, S. Campbell, J.A. Anderson, Quantitative determination of surface species and adsorption sites using Infrared spectroscopy, *Catal. Today* **2015** (259), 19–26.

[23] C. Morterra, G. Meligrana, G. Cerrato, V. Solinas, E. Rombi, M. F. Sini, 2,6-Dimethylpyridine Adsorption on Zirconia and Sulfated Zirconia Systems. An FTIR and Microcalorimetric Study, *Langmuir* **2003** (19), 5344–5356.

[24] B. Girisuta, L.P.B.M. Janssen, H.J. Heeres, GREEN CHEMICALSA Kinetic Study on the Conversion of Glucose to Levulinic Acid, *Chem. Eng. Res. Des.* **2006** (84, A5), 339–349.

[25] C. Pizzolitto, E. Ghedini, F. Menegazzo, M. Signoretto, A. Giordana, G. Cerrato, G. Cruciani, Effect of grafting solvent in the optimisation of SBA-15 acidity for levulinic acid production, *Catal. Today* **2020** (345), 183–189.

[26] H.A. Benesi, Determination of Proton Acidity of Solid Catalysts by Chromatographic Adsorption of Sterically Hindered Amines, *J. Catal.* **1973** (28), 176–178.

[27] C.A. Emeis, Determination of Integrated Molar Extinction Coefficients for Infrared Absorption Bands of Pyridine Adsorbed on Solid Acid Catalysts, *J. Catal.* **1993** (141, 2), 347–354.

[28] S. Khabtou, T. Chevreau, J.C. Lavalley, Quantitative infrared study of the distinct acidic hydroxyl groups contained in modified Y zeolites, *Microporous Mater*. **1994** (3), 133–148.

[29] F. Thibault-Starzyk, B. Gil, S. Aiello, T. Chevreau, J. Gilson, In situ thermogravimetry in an infrared spectrometer: an answer to quantitative spectroscopy of adsorbed species on heterogeneous catalysts, *Micropor. Mesopor. Mat.* **2004** (67), 107–112.

[30] J. Rosenberg, B. Bachiller-Baeza, T.J. Dines, J.A. Anderson, Nature of Surface Sulfate Species and the Generation of Active Sites on Silica-Zirconia Mixed-Oxide Catalysts, *J. Phys. Chem. B* **2003** (107), 6526–6534.

[31] C. Morterra, G. Cerrato, Titrating surface acidity of sulfated zirconia catalysts: is the adsorption of pyridine a suitable probe?, *Phys. Chem. Chem. Phys.* **1999** (1), 2825–2831.

[32] C. Morterra, G. Cerrato, F. Pinna, G. Meligrana, Limits in the use of pyridine adsorption, as an analytical tool to test the surface acidity of oxidic systems. The case of sulfated zirconia catalysts, *Top. Catal.* **2001** (15), 53–61.

[33] D.J. Rosenberg, J.A. Anderson, On the Environment of the Active Sites in Phosphate Modified Silica–Zirconia Acid Catalysts, *Catal. Lett.* **2004** (94), 109–113.

[34] I.S. Pieta, M. Ishaq, R.P.K. Wells, J.A. Anderson, Quantitative determination of acid sites on silica–alumina, *Appl. Catal. A-Gen.* **2010** (390), 127–134.

[35] A.T. Pedersen, R. Ringborg, T. Grotkjær, S. Pedersen, J.M. Woodley, Synthesis of 5-hydroxymethylfurfural (HMF) by acid catalyzed dehydration of glucose–fructose mixtures, *Chem. Eng. J.* **2015** (273),455–464.

[36] F. Robyt, *Essentials of catbohydrates chemistry*, Springer, New York, 1998.

[37] A.A. Marianou, C.M. Michailof, A. Pineda, E.F. Iliopoulou, K.S. Triantafyllidis, A.A. Lappas, Effect of Lewis and Brønsted acidity on glucose conversion to 5-HMF and lactic acid in aqueous and organic media, *Appl. Catal. A-Gen.* **2018** (555), 75–87.

[38] E. Wiercigroch, E. Szafraniec, K. Czamara, M.Z. Pacia, K. Majzner, K. Kochan, A. Kaczor, M. Baranska, K. Malek, Raman and infrared spectroscopy of carbohydrates: A review, *Spectrochim. Acta A* **2017** (185), 317–335.

[39] J.M. deMan, *Principles of Food Chemistry*, 3rd Edition, Aspen Publishers, Inc., Gaithersburg, Maryland, 1999.

[40] H.D. Belitz, W. Grosch, P. Schieberle, *Food Chemistry*, 4th Edition, Springer-Verlag, Berlin Heidelberg, 2009.

[41] J. Zakzeski, R.J.H. Grisel, A.T. Smit, B.M. Weckhuysen, Solid Acid-Catalyzed Cellulose Hydrolysis Monitored by In Situ ATR-IR Spectroscopy, *ChemSusChem* **2012** (5), 430–437.

5. CONCLUSION AND OUTLOOK

The prospecting of a sustainable industrial and societal development requires the transition of our linear economy to a circular model. In chemical manufacturing and fuels production this means to design with a cradle-to-cradle perspective. Lignocellulosic biomass represents an alternative sustainable feedstock, especially for the production of value-added chemicals. Glucose represents one of the more abundant intermediates in the lignocellulosic degradation and can be further converted into many platform chemicals. The use of heterogeneous catalysts allows to reduce both environmental impact and industrial cost. Glucose hydrolysis requires bifunctional solid acid catalysts, with high selectivity and activity in water. Sulfated zirconia (SZ), a well-known catalyst already employed in several industrial processes, could be a valuable alternative, and has shown to be able to promote the production of 5-hydroxymethylfurfural (5-HMF) from glucose. Activity and selectivity of SZ systems can be improved tuning both amount and strength of Lewis and Brønsted acid sites. It is well known that surface properties of SZ systems are strongly affected by both preparation method and calcination temperature. The most common methods employed for the synthesis of SZ are long multi-step procedures, that usually require a final calcination. Employment of MW heating can help to reduce energy consumption and reaction time, rendering more sustainable the synthetic process.

We proposed a MW-assisted sol gel procedure that involves two steps of few minutes, both assisted by MW heating. In the first step the gel is dried (MW-assisted drying) and in the second step the obtained xerogel is calcined using a susceptor to rapidly reach high temperature(s) (MW-assisted calcination). At first this procedure was applied to the synthesis of

plain zirconia, and homogeneous small nanoparticles exhibiting pure tetragonal phase have been obtained, as indicated by both vibrational and structural characterizations. Only few similar studies have been reported in literature so far and suggest that MW heating promotes the formation of tetragonal phase if applied during either gel formation or in gel drying. If compared to the materials obtained in these studies, our samples appear to be more crystalline.

To optimize the procedure and understand the effect of MW heating, we investigated the effect of some synthetic parameters as (i) hydrolysis catalyst, (ii) nature of the solvent and (iii) gel aging. Three different acids (HNO_3, H_2SO_4 and CH_3COOH) were used to promote the hydrolysis of the zirconium propoxide precursor. The only appropriate acid hydrolysis catalyst appears to be nitric acid, while using sulfuric and acetic acids, amorphous products were obtained. This effect seems to be related to the different mechanism of crystallization and degradation of the relevant anions during MW-assisted calcination, as the temperature reached in the MW oven (T maximum ~ 750°C) seems to be sufficient to promote zirconia crystallization only in presence of nitrate ions, that easily degrade during calcination. Pure tetragonal zirconia has been obtained from both the employed solvents, ethanol and 2-propanol. HR-TEM images indicates that using ethanol the obtained nanoparticles are more homogeneous in both shape and dimension, exhibiting a more ordered external habit. It can be noted that ethanol has a higher loss tangent than 2-propanol, and MW-assisted drying seems to be more efficient for gels obtained from ethanol. This may affect the nature of the obtained xerogel and of the relevant calcinated product. With respect to gel aging time, the two solvents have shown a very different behaviour. Using 2-propanol, pure t-ZrO_2 has been obtained after 24 hours of gel aging, whereas samples obtained after shorter times are mainly amorphous. On the contrary, using ethanol as solvent, a tetragonal

product is formed, no matter of the aging time, and an increase of the monoclinic fraction is observed with the increase of aging time.

The step that seems to be more influenced by MW heating is suggested to be calcination. Pure tetragonal zirconia has been obtained by MW-assisted calcination of zirconium hydroxide (from $ZrOCl_2$), while xerogel (from MW-assisted drying) calcined by conventional method gives particles showing both monoclinic and tetragonal phase. MW hybrid heating method, which employed a susceptor to transfer heat to the sample, have been applied previously in materials production, ceramic sintering and solid state syntheses of mixed oxides, but to the best of our knowledge never to carry out calcination on amorphous materials. MW-assisted method allows to extremely reduce calcination time and energy consumption, if compared to traditional thermal treatments. Moreover, the experimental results suggest that the rapid heating provided by MW irradiation promotes the formation of the tetragonal phase, the most valuable in catalytic applications.

The proposed MW-assisted procedure has been then applied in the synthesis of both SZ and Ni-promoted ZrO_2. After impregnation with either nickel or sulfate precursors, the dried powders have been always thermally treated by MW-assisted calcination.

In the case of nickel promotion, the addition step has shown to strongly influence the chemical nature of the final product, as detailed in the following:

(i) When Ni precursor is impregnated on crystalline zirconia, NiO is formed on the particles surface that retain the tetragonal phase, as evidenced by PXRD, vibrational and TEM analyses. FTIR data, obtained by using CO as probe molecule, confirmed the presence of surface Ni^{2+} sites.

(ii) The formation of the cubic phase is observed when Ni impregnation is carried out on the still amorphous xerogel, as suggested by diffraction data and confirmed by Raman spectroscopy. It is supposed that part of the Ni species is incorporated into the zirconia lattice stabilizing a fluorite-like structure, the same of nickel oxide. If we refer again to FTIR spectroscopy, CO adsorption indicates that part of the Ni species is exposed at the surface as Ni^{2+}, but the presence of metallic Ni is suggested as well. TEM images confirmed the presence of small nanoparticles of metallic Ni, but also that the material is poorly crystalline and very heterogeneous in both shape and dimension of nanoparticles and in chemical composition.

(iii) By adding Ni precursor in the starting solution, tetragonal zirconia nanoparticles are formed. Ni ions are incorporated into the zirconia structure (at least in the outer spheres of the crystallites), and the lattice disorder causes a broadening in the Raman signals. Small roundish nanoparticles, quite homogenous in shape and dimension are observed in the TEM images. CO absorption indicates that nickel is present on the surface as Ni^{2+}, Ni^{+} and Ni^{0} species.

The impregnation step is the most relevant parameter also in the preparation of SZ. Impregnation on t-ZrO_2 seems to promote the formation of a small fraction of monoclinic phase, and samples possess surface sulfate species having a covalent character. When impregnation is carried out on the xerogel, the powder obtained is less crystalline and sulfate species seems to have a more ionic nature. Also the c-ZrO_2 samples obtained by Ni impregnation on xerogel are poorly crystalline, suggesting that MW-assisted calcination is less effective if carried out on the impregnated amorphous intermediate. The nature and strength of surface acidity have been investigated using CO and 2,6-dymethylpyridine (2,6-DMP) as probe

molecules. Results indicate that both Lewis (L) and Brønsted (B) acid sites are present, but their relative strength is influenced by both the impregnation method and impregnation step.

The mechanism of acid catalyzed glucose hydrolysis is supposed to start via isomerization to fructose, and continue through dehydration in 5-hydroxymethylpyridine (5-HMF), that could be possibly hydrolyzed into levulinic acid (LA). The first step is supposed to be Lewis acid catalyzed, while dehydration/hydration reactions are catalyzed by Brønsted acid sites. Three SZ samples have been tested as possible catalysts in glucose hydrolysis: (i) S2Z_WI (by WI on t-ZrO_2) having surface sulfates with a covalent character and presenting weak L and B sites; (ii) S2Z_8 (by WI on t-ZrO_2) that has surface sulfate species with a more covalent character and present L and B acid sites of medium strength; (iii) S1Z_5 (by IWI xerogel) partially amorphous, showing surface sulfates with a less pronounced covalent character, and presenting weak L and B acid sites. The first two catalysts have shown to promote 5-HMF production at discrete yield, while S1Z_5 is resulted to be poorly active. Catalytic results were compared to those obtained from other systems presenting L and B acid sites of medium strength on their surfaces: a 'model' SZ (obtained from standard precipitation route) and SBA-SO_3H. In glucose conversion these model systems promote the formation of both 5-HMF and LA. To better understand the relation between L and B acid sites and catalyst selectivity it is necessary to quantify the amount of surface acid sites.

The quantitative assessment of acid sites can be carried out by means of FTIR spectroscopy. In particular, the adsorption/desorption of 2,6-DMP gives rise to two distinct and characteristic complex bands associated to the interaction with both B and L acid sites, but the real quantitative assessment requires the knowledge of molar extinction coefficients (ε) of

the relevant 2,6-DMP modes. Values of molar extinction coefficients for Lewis and Brønsted modes for SBA-SO_3H and SZ were determined by volumetric methods. The calculated ε_L and ε_B values were found to be 1.1 and 5.8 cm μmol^{-1}, respectively, for SZ, and 3.9 and 5.2 cm μmol^{-1}, respectively, for SBA-SO_3H. These values are very different from those reported in the literature for similar systems. We suppose that this difference can be related to the different surface acid properties of the materials. The values reported in the literature were obtained for materials presenting either only strong Lewis acidity (as silica or plain zirconia) or strong Brønsted sites (phosphated silica or W/Nb oxides supported on zirconia). On the contrary, our materials present at the same time both Lewis and Brønsted acid sites of medium strength. We suppose that the simultaneous presence of both Lewis and Brønsted sites could affect the location and bonding type of adsorbed molecules and, consequently, the values of molar absorption coefficients thereon. However, further studies on other metallic oxide are necessary to confirm this assumption.

The calculated ε_L and ε_B values have been used to determine L/B ratio. All catalysts that promote LA formation possess L/B values lower than 1, confirming that Brønsted acidity is a necessary condition to promote 5-HMF hydrolysis. On the contrary, Lewis acidity seems to be sufficient to obtain 5-HMF: discrete yields (around 35%) of 5-HMF were obtained using pristine SBA, presenting only Lewis acidity, and S2Z_WI, having a pronounced Lewis character. The mechanism of acid catalyzed glucose hydrolysis can follow different pathway. Isomerization to fructose, that is supposed to be the rate-determinant step, can proceed via acyclic and cyclic route. Alternatively, glucose can be directly dehydrated to 5-HMF without fructose formation. Moreover, glucose and/or fructose can be converted to multiple other products, with more than one reaction pathways taking place

simultaneously. One example is a retro-aldol reaction, that brings to the formation of short-chain carboxylic acids (namely, acetic, lactic and formic acid). We supposed that the nature and amount of L and B acid sites can influence the reaction mechanism and lead to a different selectivity.

To verify this hypothesis, it will be appropriate to apply the *operando* spectroscopy methodology. This approach permits to investigate relationship between catalyst structure (bulk/surface) and catalyst performance (activity and selectivity), by simultaneously collecting catalyst characterization and online product(s) analysis data. To understand if this approach could be valid to study glucose hydrolysis, we carried out some preliminary studies by infrared spectroscopy. At first, we analysed the heating of pure glucose and of mixtures glucose+catalyst (from ambient T to 180°C) recording time-resolved spectra by ATR. Results indicate that, even in the presence of small amounts of water, both systems (SZ and SBA-SO_3H) seem to act as catalyst. In fact, caramelization, observed for pure glucose, is inhibited in the presence of catalyst. These results suggest that an appropriate experiment design could be applied to the study of acid-catalyzed glucose hydrolysis.

Supplementary Material

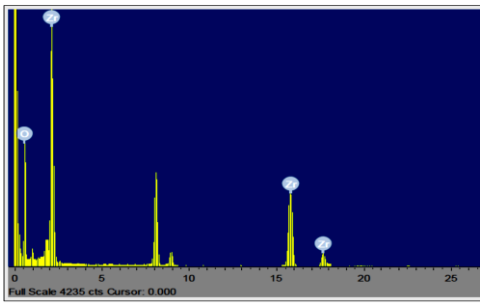

Element	Weight %	Atomic %
Zr	74.03	33.33
O	25.97	66.67
Total	100.00	100.00

Figure S5. EDS pattern of ZE_0.

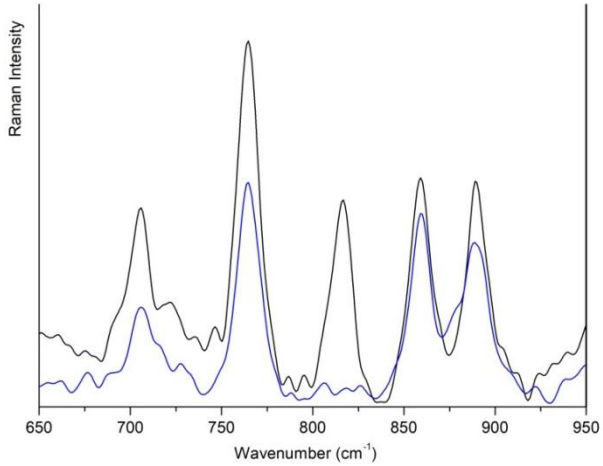

Figure S6. Raman spectra of xerogel from 2-propanol (in black) and ethanol (in blue).

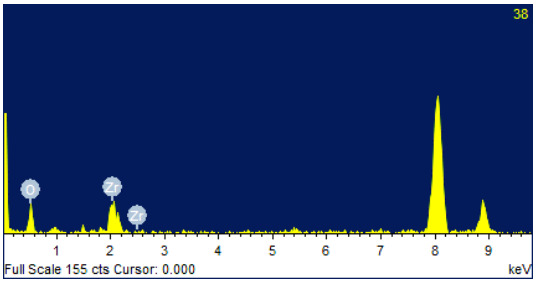

Element	Weight %	Atomic %
Zr L	74.03	33.33
O	27.97	66.66
Total	100.00	100.00

Figure S7. EDS analysis on Ni0Z_2.

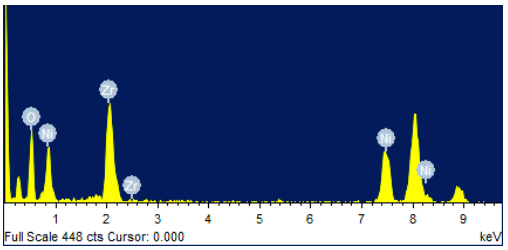

Element	Weight %	Atomic %
Ni K	5.26	3.66
Zr L	69.08	30.90
O	25.66	65.45
Total	100.00	100.00

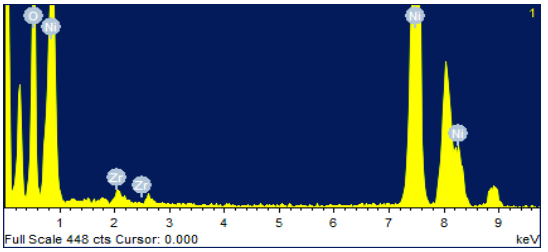

Element	Weight %	Atomic %
Ni K	50.01	32.90
Zr L	26.92	11.40
O	27.03	55.70
Total	100.00	100.00

Figure S8. EDS analysis of Ni1Z_10 on different portions of the grid.

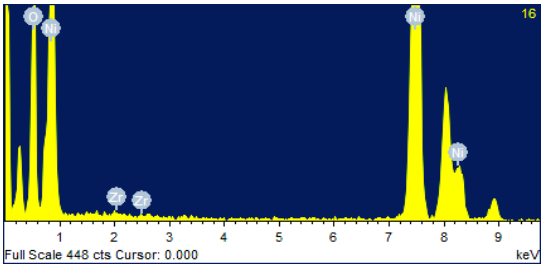

Element	Weight %	Atomic %
Ni K	68.78	44.26
Zr L	9.23	3.82
O	21.98	51.91
Total	100.00	100.00

Figure S9. EDS analysis on Ni2Z_10.

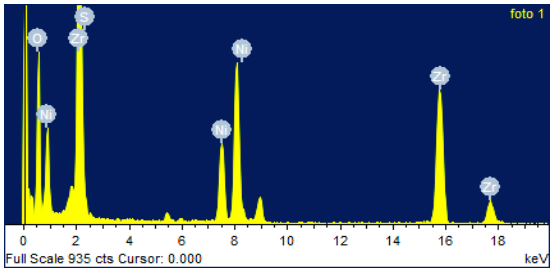

Element	Weight %	Atomic %
Ni K	0.48	0.18
Zr L	31.23	7.46
S K	0.97	0.66
O K	67.32	91.7
Total	100.00	100.00

Figure S10. EDS analysis on Ni3S2Z.

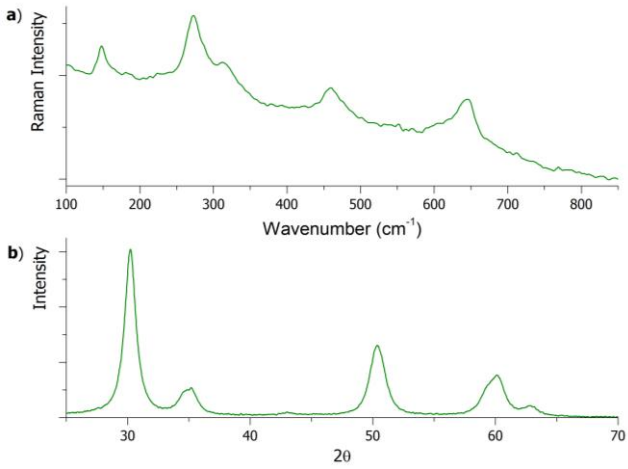

Figure S11. Raman spectrum (a) and XRD diffractogram (b) of SZ_prec catalyst.

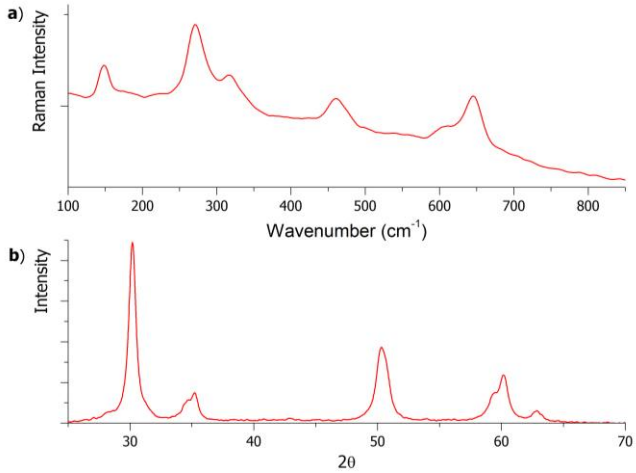

Figure S12. Raman spectrum (a) and diffractogram (b) of S2Z_8 catalyst.

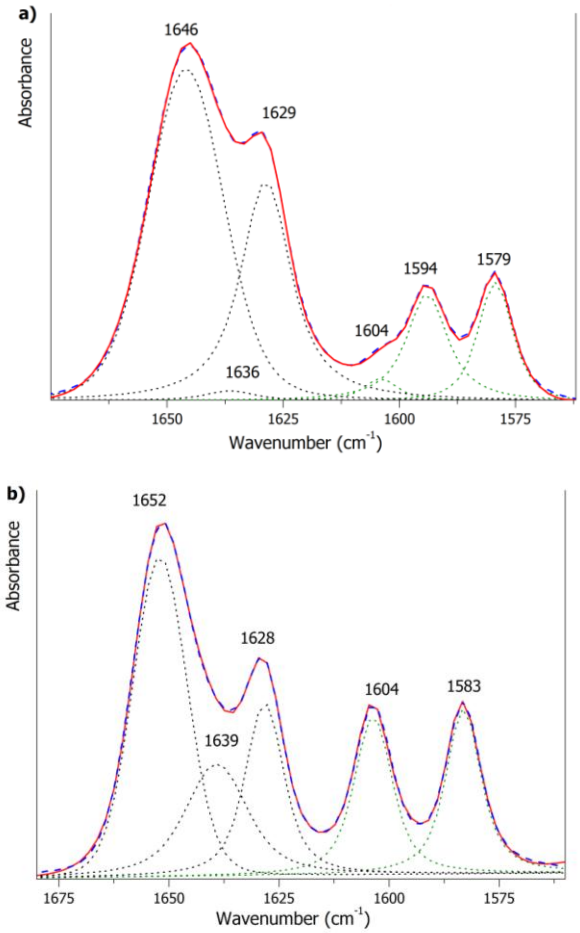

Figure S13. Examples of curve-fitting at the maximum 2,6-DMP amount for: (a) SZ and (b) SBA-SO_3H.

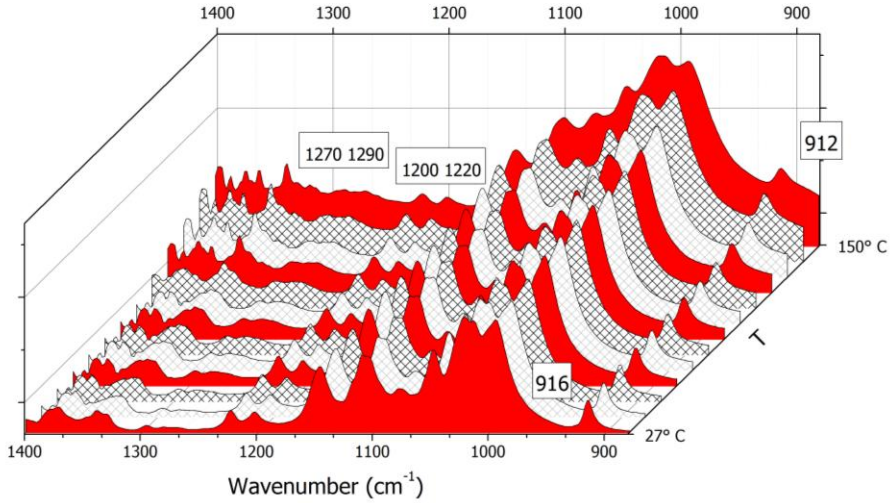

Figure S14. Temperature-resolved ATR spectra of glucose (from 27°C to 150 °C); red colour indicates T multiples of 30°C.

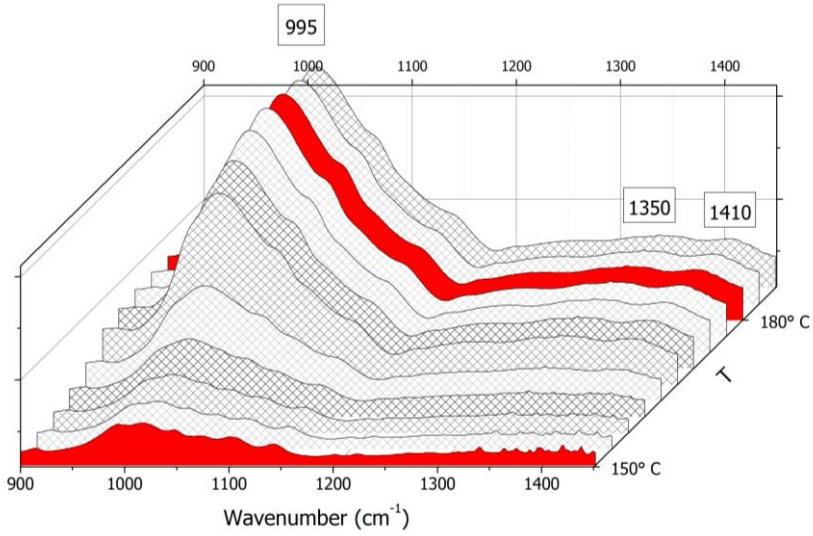

Figure S15. Temperature-resolved ATR spectra of glucose (from 150°C to 180°C).

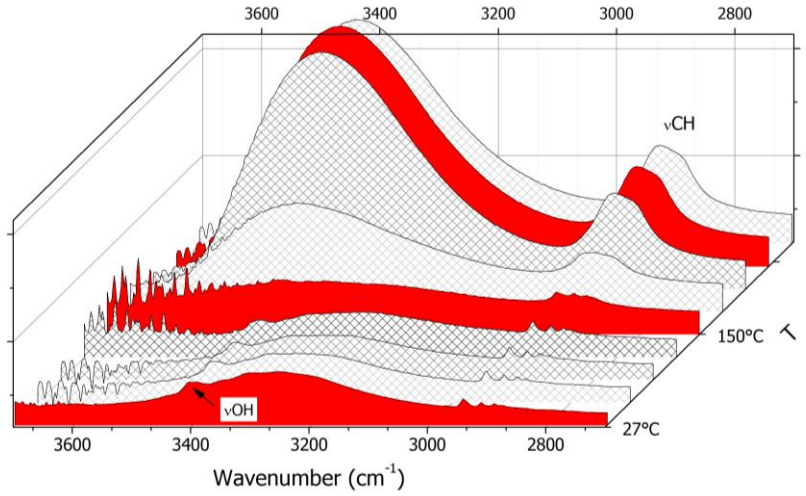

Figure S16. Temperature-resolved ATR spectra of glucose in the high frequencies spectral range (from 27°C to 180°C).

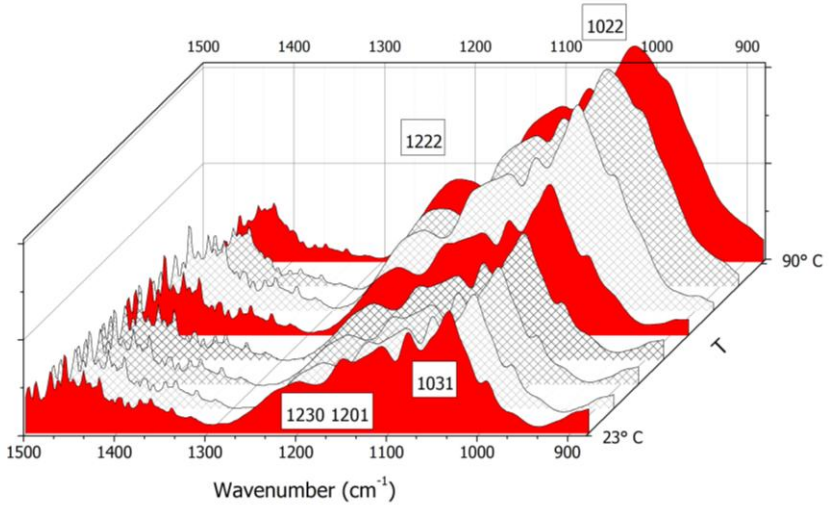

Figure S17. Temperature-resolved ATR spectra of glucose+SZ mixture (from 23°C to 90°C); red colour indicates T multiples of 30°C.

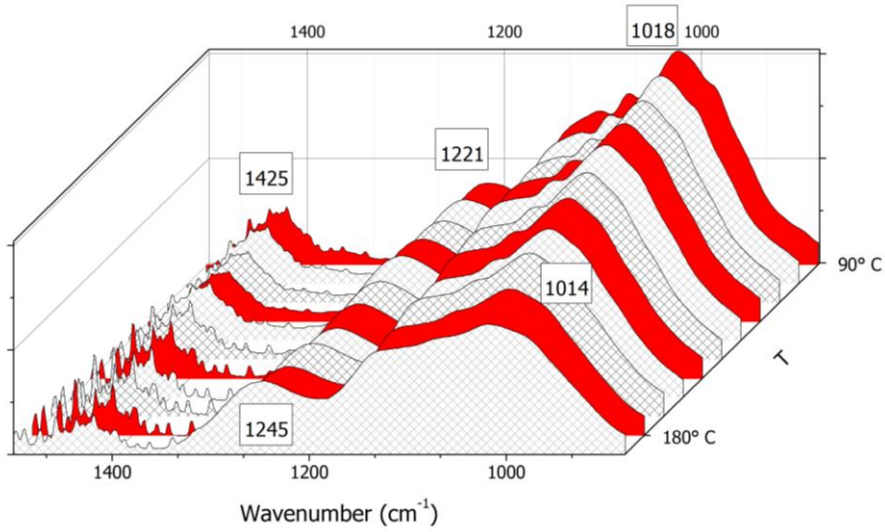

Figure S18. Temperature-resolved ATR spectra of glucose+SZ mixture (from 90°C to 180°C); red colour indicates T multiples of 30°C.

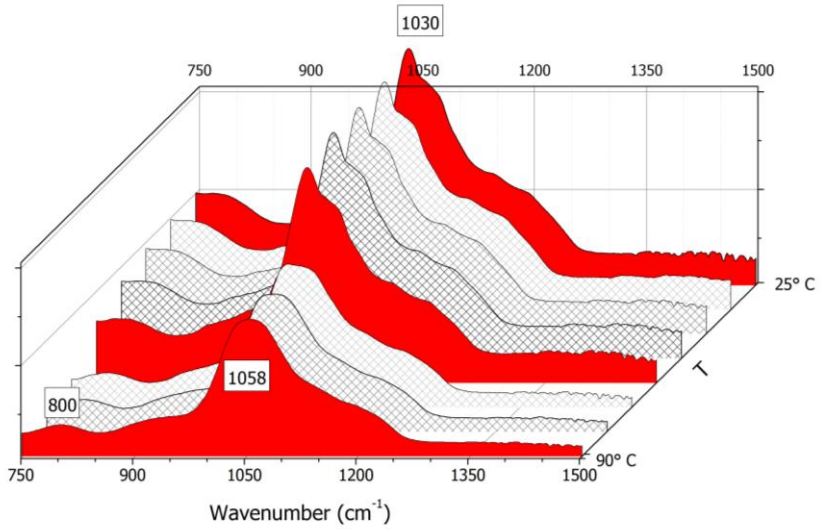

Figure S19. Temperature-resolved ATR spectra of glucose+SBA-SO_3H mixture (from 25°C to 90°C); red colour indicates T multiples of 30°C.

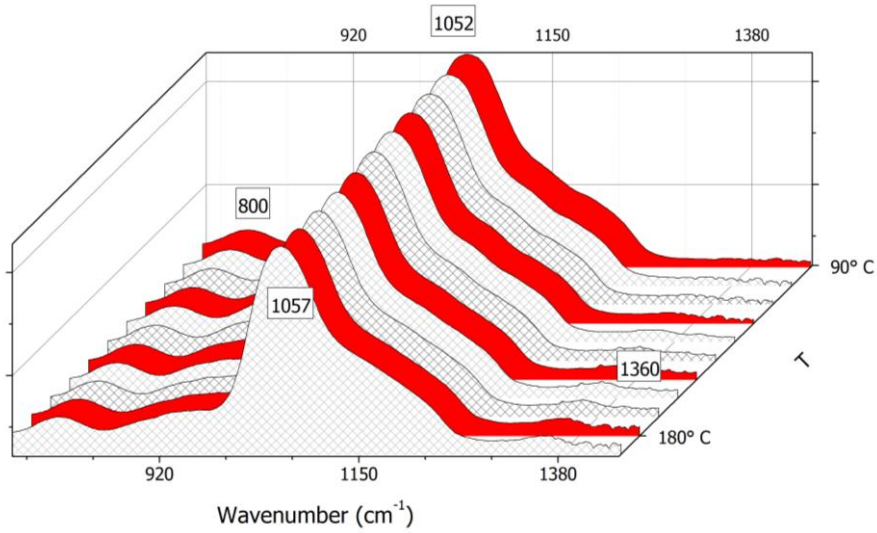

Figure S20. Temperature-resolved ATR spectra of glucose+SBA-SO_3H mixture (from 90°C to 180°C); red colour indicates T multiples of 30°C

Ringraziamenti

Questi anni di dottorato sono stati un periodo intenso, ricco di esperienze e di emozioni. Il lavoro di ricerca sperimentale è stato costituito da alti e bassi, momenti di entusiasmo e scoraggiamento che ho condiviso con amici e colleghi. È stato soprattutto grazie al loro sostegno e aiuto che sono riuscita a superare i momenti di maggiore sconforto e vorrei quindi ringraziarli.

Il mio primo ringraziamento va alla mia tutor, la Prof.ssa Pinuccia Cerrato, per la fiducia che ha avuto in me e per la pazienza che ha mostrato nel seguirmi in questo percorso. La sua passione per la chimica e la didattica, la sua professionalità, la sua grande conoscenza scientifica e non solo mi hanno fatto crescere come scienziata e come donna.

Vorrei ringraziare il Prof. Eliano Diana, che nel corso di questi e dei precedenti anni è sempre stato disponibile, fornendomi spesso l'indicazione giusta al momento giusto. Le lunghe chiacchierate con lui, che partendo dalla chimica passano all'arte o all'attualità, sono state fonte di ispirazione.

Voglio ringraziare i miei compagni di ufficio e laboratorio, che hanno reso le mie giornate meno pesanti e più allegre e sono diventati nel tempo molto più che solo colleghi: il Dott. Emanuele Priola, che riesce a sempre a farmi sorridere, contagiandomi con il suo entusiasmo per la ricerca, il Dott. Luca Andreo per i suoi canti e la sua infinita disponibilità e la Dott.ssa Maria Labate, sempre pronta ad ascoltarmi e sostenermi. Senza di loro questo viaggio non sarebbe stato lo stesso. Vorrei anche ringraziare tutti i tesisti che sono passati dal quarto piano: hanno contribuito a rendere l'ambiente stimolante e vivace.

Vorrei ringraziare la Dott.ssa Elisabetta Bonometti, la mia sorella maggiore al quarto piano, che mi ha fornito assistenza tecnica e scientifica

nelle procedure con le microonde. Un grande ringraziamento va anche alla Dott.ssa Francesca Turco, che mi ha dato coinvolto nei progetti di divulgazione scientifica e di storia della chimica.

Vorrei ringraziare il Prof. Roberto Rabezzana e il Prof. Gianmario Martra, che mi hanno coinvolto nei loro progetti permettendomi di esplorare nuovi e interessanti campi di ricerca. E voglio ringraziare tutto il gruppo di colleghi del quarto e quinto piano, anche per i bei momenti conviviali.

Un doveroso ringraziamento va ai professori che mi hanno ospitato nei loro laboratori. Il prof. Misha Bogdanov mi ha accolto a Houston e mi ha dato la possibilità di studiare l'applicazione dei nanomateriali in campo biomedico. La Prof.ssa Michela Signoretto di Ca' Foscari per gli ottimi suggerimenti e tutto il gruppo CatMat, che ha arricchito scientificamente e umanamente la mia esperienza veneziana. E il Prof. Marco Daturi per la sua accoglienza, disponibilità e le stimolanti discussioni durante il mio soggiorno a Caen.

Infine, ma non per importanza, vorrei ringraziare il mio compagno Angelo. Ha sopportato i miei ritmi di lavoro impossibili, sempre pronto a consolarmi con qualche manicaretto e festeggiare i miei piccoli e grandi successi con un brindisi. Senza di lui non ce l'avrei fatta!

In ultimo, un pensiero va a mio padre, a cui dedico questo traguardo.

Acknowledgements

These years have been an intense period, full of experiences and emotions. The experimental work consists of ups and downs, that I shared with friends and colleagues. Thanks to their support, I was able to overcome moments of discouragement and therefore I would like to thank all of them.

At first, I thank my supervisor, Prof. Pinuccia Cerrato, for always trusting in me and for her patience during these years. Her passion for chemistry and teaching, her professionalism, her great knowledge in science and not only made me grow up as both a scientist and a woman.

I would like to thank Prof. Eliano Diana, for the availability to listen to me, giving me the right indication at the right time. Long conversations with him, starting from chemistry and passing to art or current events, have been a great source of inspiration.

I want to thank my office and laboratory mates, who made my days less heavy and happier and became more than simple colleagues: Dr. Emanuele Priola, for his infecting enthusiasm for science and research, Dr. Luca Andreo for his singings and his infinite availability and Dr. Maria Labate, always ready to listen and support me. Without them this journey would not have been the same. I would also like to thank all the graduate students who have passed from the 4th floor: they contributed to render the environment stimulating and lively.

I would like to thank Dr. Elisabetta Bonometti, my older sister on the 4th floor, who provided me technical and scientific assistance in microwave procedures. A big thank also to Dr. Francesca Turco, who involved me in the scientific dissemination.

I would like to thank Prof. Roberto Rabezzana and Prof. Gianmario Martra, who involved me in their projects allowing me to explore interesting research fields. And all the colleagues of the 4th and 5th floors for the beautiful convivial moments.

A due thank goes to professors who hosted me. Prof. Misha Bogdanov welcomed me in Houston and gave me the opportunity to study the application of nanomaterials in the biomedical field. Prof. Michela Signoretto from Ca' Foscari for her excellent suggestions and all members of CatMat group, who enriched my Venetian experience, scientifically and humanly as well. Prof. Marco Daturi for his warm welcome, helpfulness and stimulating discussions during my stay in Caen.

Last but not least, I would like to thank Angelo, my partner. He always understood my impossible work rhythms, and was always ready to console me with good food and to celebrate my little and big successes with a toast. Without him I would not have made it!

Finally, a thought goes to my father, to whom I dedicate this goal.

LEARNING ACTIVITIES

Papers

- C. Pizzolitto, E. Ghedini, F. Menegazzo, M. Signoretto, A. Giordana, G. Cerrato, G. Cruciani, Effect of grafting solvent in the optimisation of SBA-15 acidity for levulinic acid production, *Catal. Today* **2020** (345), 183–189.
- L. Rimoldi, A. Giordana, G. Cerrato, E. Falletta, D. Meroni, Insights on the photocatalytic degradation processes supported by TiO_2/WO_3 systems. The case of ethanol and tetracycline*, Catal. Today* **2019** (328), 210–215.
- A. Giordana, E. Priola, E. Bonometti, P. Benzi, L. Operti, E. Diana, Structural and spectroscopic study of the asymmetric 2-(2'-pyridyl)-1,8-naphthyridine ligand with closed-shell metals, *Polyhedron* **2017** (138), 239–248.

Presentations

1. Oral presentation: "Microwave-assisted synthesis of zirconia: catalyst for biomass valorization" – A. Giordana, E. Diana, L. Operti, G. Cerrato – Summer School To.Sca.Lake 3.0 – Como (Italy), May 27th-31st, 2019.
2. Oral presentation: "Microwave-assisted synthesis of zirconia: solid acid catalyst for biomass valorization" – A. Giordana, E. Bonometti, E. Diana, L. Operti, G. Cerrato – Merck&Elsevier Young Chemists Symposium – Rimini (Italy), November 19th-21st, 2018.

1. Poster presentation: "Microwave assisted synthesis of zirconia: catalyst for biomass valorisation" – A. Giordana, E. Diana, L. Operti, G. Cerrato, C. Pizzolitto, E. Ghedini, M. Signoretto – EuropaCat 2019 – Aachen (Germany), August 18th-23th, 2019.
2. Poster presentation: "Microwave assisted synthesis of zirconia: solid catalyst for biomass valorisation" – A. Giordana, E. Bonometti, E. Diana, L. Operti, G. Cerrato – Winter School Innovative Catalysis and Sustainability – Bardonecchia (Italy), January7th-11th, 2019.
3. Poster presentation: "Zirconia: solid acid catalyst for biomass valorisation" – A. Giordana, E. Bonometti, E. Diana, L. Operti, G. Cerrato – EFCATS Summer School on Catalysis – Liblice Castle (Czech Republic), June 25th-29th, 2018.
4. Poster presentation: "Hetergeneous catalysts for biomass valorisation: the case of t-ZrO_2" – A. Giordana, E. Bonometti, E. Diana, L. Operti, G.

Cerrato – Giornate Italo-Francesi di Chimica – Genova, April 16th-18th, 2018.

5. Poster presentation: "Nano-tetragonal zirconia for catalytical purpose" – A. Giordana, E. Bonometti, E. Diana, L. Operti, G. Cerrato – Chess 2017, Scuola di analisi delle superfici – Firenze, November 27th-30th 2017.
6. Poster presentation: "Microwave-assisted synthesis of tetragonal zirconia" – A. Giordana, E. Bonometti, E. Diana, L. Operti, G. Cerrato – Merck Young Chemists Symposium – Milano Marittima (Italy), November 13th-15th, 2017.
7. Poster presentation: "Total microwave synthesis of ZrO_2" – A. Giordana, E. Bonometti, E. Diana, L. Operti, G. Cerrato – International Workshop "Advanced inorganic material: green and unconventional synthesis approaches and functional assessment" – Department of Chemical Science, Padova, September 8th, 2017.

Periods Abroad

- Period: August 24th - September 27th, 2019. Laboratorie Catalyse&Spectrochimie (ENSI) – Caen (France). Supervisor: Prof. M. Daturi
- Period: May 4th, 2017- July 9th, 2017. UTHealth, University of Texas – Houston (USA). Supervisor: Prof. M. Bogdanov

PhD Schools Attended

- Summer School "To.Sca.Lake 3.0-Total scattering for nanotechnology", Como (Italy), May 27th-31st, 2019.
- Winter School "Innovative Catalysis and Sustainability: scientific and socio-economic aspects", Bardonecchia (Italy), January 7th-11th, 2019.
- EFCATS Summer School on Catalysis, Liblice Castle (Czech Republic), June 25th-29th, 2018.
- Chess 2017 "Conventional And High-Energy Spectroscopies For Inorganic, Organic And Biomolecular Surfaces And Interfaces", Firenze, November 27th-30 th 2017.
- NOVACAM Winter School "Green Catalysis by Design", Padova, February 22th, 2017.
- Winter school "Raman Spectroscopy Applied to Earth, Environmental and Chemical Sciences", Torino and Milano, January 25th-27th, 2017.

Seminars, Conferences Attended

- EuropaCat 2019 (14th European Congress on Catalysis) – Aachen (Germany), August 18th-23th, 2019.
- ISPC 2019 (23rd Conference of the International Society for the Philosophy of Chemistry) – Torino, July 15th-17th, 2019.
- Merck&Elsevier Young Chemists Symposium 2018 – Rimini (Italy), November 19th-21st, 2018.
- Prima Giornata Di Studio "Sostenibilità e Processi Chimici Microonde Mediati" – Genova, October 19th, 2018.
- Giornate Crisdi "The Role of Crystallography in Drug Science and Biology" – Torino, March 5th, 2018.
- Workshop "Analisi quantitative di fasi cristalline: metodi tradizionali e chemiometria a confronto" – Bologna, February 6th, 2018.
- Merck Young Chemists Symposium – Milano Marittima (Italy), November 13th-15th, 2017.
- International Workshop "Advanced inorganic material: green and unconventional synthesis approaches and functional assessment" – Padova, September 8th, 2017.
- International Conference "Green Catalysis by Design" – Padova, February 23th, 2017.
- Giornata dedicata alla valorizzazione delle competenze dei dottori di ricerca e al posto – Torino, October 4th,2016.
- Workshop "Introduzione al Foundrising" – Torino, October 4th,2016.

Teaching support activities

- Tutoring for "Chimica Generale e Inorganica", degree course of "Scienze Naturali". (3 activities of 40 hours each).

PhD Courses Attended

Course title	Instructor	University / Department	Hours
English for Scientific	J. Robinson	Torino / Scuole di	30

Course title	Instructor	University / Department	Hours
Academic Purposes for PhD students	(IUSE)	Dottorato in Scienze della Natura	
Artificial photosynthesis: mimicking nature to produce the energy of the future	E. Giamello	Torino / Chimica	8
Raman microspectroscopy: practical course	P. Rossetti, S. Ferrando	Torino / Scienze della Terra	4
Theoretical and practical learning course for TEM-EDS utilization	E. Belluso	Torino / Scienze della Terra	22
An insight into epistemological and didactic issues related with science teaching	E. Ghibaudi, G. Cerrato, F. Vindinghi	Torino / Chimica	12
Citing, being cited, preserving your identity and your work, archiving electronically your bibliography: a know-how guide for a changing world	B. Martin	Torino / Chimica	8

Course title	Instructor	University / Department	Hours
BC1: Introduction to Crystallography	P. Benna	Torino / Crisdi (Crystallography School 2018)	6
BC2: Instrumentation for X-Ray Diffraction	A. Agostino	Torino / Crisdi (Crystallography School 2018)	4
BC3: Electron Diffraction	R. Cossio	Torino / Crisdi (Crystallography School 2018)	4
BC4: X-Ray Diffraction	A. Pavese	Torino / Crisdi (Crystallography School 2018)	4
BC5: X-Ray Diffraction Methods: Polycrystalline	M. Milanesio (Uniupo)	Torino / Crisdi (Crystallography School 2018)	10
SC3: Solid State Properties: Modelization	A. Ferrari	Torino / Crisdi (Crystallography School 2018)	8
SC6: The Debye Scattering Equation: a Total Scattering approach for characterizing Nanomaterials	F. Bertolotti (Uninsubria)	Torino / Crisdi (Crystallography School 2018)	4
SC13: Pair Distribution function analysis of complex, disorder and amorphous Materials from Total Scattering Data.	M. Dapiaggi (Unimi)	Torino / Crisdi (Crystallography School 2019)	4